UNIVERSITÉ DU QUÉBEC À MONTRÉAL

DIFFUSION IN BATTERY MATERIALS

DISSERTATION

PRESENTED

AS PARTIAL FULFILLMENT

OF THE DOCTORATE IN CHEMISTRY

BY

CHRISTIAN KUSS

AUGUST 2014

UNIVERSITÉ DU QUÉBEC À MONTRÉAL

LA DIFFUSION DANS LES MATERIAUX DES BATTERIES

THÈSE

PRÉSENTÉE

COMME EXIGENCE PARTIELLE

DU DOCTORAT EN CHIMIE

PAR

CHRISTIAN KUSS

AOUT 2014

ACKNOWLEDGEMENTS

While writing a dissertation is an elaborate, if not cumbersome and sometimes frustrating task, it was nevertheless a very pleasant experience for me, from which I learned a lot about chemistry and materials, but also about the overall natural sciences, writing, organization, professional relationships and life in general. This experience is largely determined by the environment, and for this I would like to thank,

My supervisor Professor Steen Brian Schougaard, for accepting me as a graduate student, for pushing me to improve, for supporting my professional development outside of research, be it on conferences or in the ECS Student Chapter, and for his patience and support for my personal life;

Our research group, particularly Dr. David Lepage, who helped me a lot to get started in the group, and also Ngoc Duc Trinh, Mathieu Saulnier, Dr. Renaud Cornut, Dr. Aurore Castets, Dr. Reza B. Moghaddam, Dr. Michael Snowdon, Stefan Andjelic, Fatima Sobh, Danny Chhin, Jason Vachon and Simon Gervais for the many helpful discussions, and their friendship;

Once more Ngoc Duc Trinh and Stefan Andjelic, for assisting us at the Advanced Photon Source, to make the best use of our precious beam time;

Our undergraduate and collegial researchers Murielle Carmant-Dérival and Yanis Bouktit, for their assistance;

Professor Benoit Marsan and Professor Mohamed Siaj, for accompanying my research and providing helpful comments, and Prof. Huu van Tra for his dedicated support as program director;

Gwenaël Chamoulaud, for maintaining much of the equipment and the technical assistance;

Dr. Eric Dufresne, Dr. Donald Walko, Harold Gibson and the Advanced Photon Source, for enabling high impact research;

Thierry Maris, Jean-Philippe Masse, Sylvain Essiembre, Dr. Pascale Chevallier, Dr. Andrey Moiseev, and everyone else, who provided technical assistance with my experiments;

Professor Mark Sutton and Professor Dominic Ryan, who assisted us with *in situ* X-ray diffraction and Mössbauer spectroscopy (even if this data did not make it into this work);

UQAM, for its understanding for the special circumstances, which arise when students change the educational system during their studies;

The Fondation UQAM, for much appreciated financial support, and the entailed encouragement;

My parents, for supporting me to study chemistry and providing me with a foundation that made it possible;

And last but certainly not least, my wife Sabine, for her patience when reading and listening to this and other works, for the very helpful comments and for helping me to obtain a broad perspective on science. I also thank her and my children Theo and Klara for pulling me back into reality, when equations, atoms and molecules became too much my friends.

DEDICATION

To my wife Sabine, and my children Theo and Klara.

TABLE OF CONTENTS

LIST OF FIGURES

LIST OF TABLES

LIST OF ABBREVIATIONS

AES	Atomic emission spectroscopy
ANL	Argonne National Laboratory
APS	Advanced Photon Source
ATR	Attenuated total reflectance
CLUMEQ	Consortium Laval, UQAM, McGill, and Eastern Quebec
FTIR	Fourier-transform infrared (spectroscopic techniques)
GULP	General Utility Lattice Program
HRTEM	High Resolution Transmission Electron Microscopy
JMAEK	Johnson-Mehl-Avrami-Erofe'ev-Kolmogorov model
NHE	Normal hydrogen electrode
NSERC	National Science and Engineering Research Council
PVDF	Polyvinylidene difluoride
SE	Secondary electron
SEI	Solid electrolyte interface
SEM	Scanning electron microscopy
TEM	Transmission electron microscopy
UV	Ultraviolet light (electromagnetic radiation from 10 nm to 400 nm wavelength)
XRD	X-ray diffraction
XPS	X-ray photoelectron spectroscopy

LIST OF SYMBOLS AND UNITS

a	Activity
A	Surface area if used as symbol, Ampere if used as unit
Å	Angstrom
A_B	Buckingham potential parameter
c	Concentration
C	Coulomb or Cycling rate (equivalent to (dis-)charge/hour)
C_B	Buckingham potential parameter
C_P	Heat capacity
°C	Degrees Celsius
d	Lattice spacing
D	Diffusion coefficient
D_{Li}	Diffusion coefficient of Li^+ ions
e	Euler's number e = 2.718 …, or electron charge e = 1.602 … 10^{-19} C
eV	Electronvolt
E	Electrode potential, or Youngs modulus (Appendix D)
E°	Electrode potential under standard conditions
f	Atomic scattering factor
f_A	Absorption factor
f_L	Lorentz factor
f_P	Polarization factor
f_T	Temperature factor
F	Faraday's constant F = 9.649 … 10^4 C mol^{-1}
$F_{h,k,l}$	Structure factor of diffraction reflex at Miller's indices h, k and l
g	Gramm
G	Gibb's free energy, or shear modulus (Appendix D)
$G^‡$	Gibb's free energy at transition state
GoF	Goodness of fit
h	Hour
H	Enthalpy

i	Electric current
i_0	exchange current
I	Diffraction intensity
I_G	Intensity of Gaussian peak
$I_{h,k,l}$	Diffraction intensity at Miller's indices h, k and l
I_L	Intensity of Lorentzian peak
J	Joule
k	Rate constant
k_s	Spring constant
K	Bulk modulus, if used as symbol, Kelvin if used as unit
L	Crystallite size
m	Meter if used as unit, multiplicity of diffraction reflex in calculating diffraction intensity
mol	Mole
M	Molar (= mol dm^{-3})
n	Amount of substance
n_a	Avrami exponent
N	Number of points
pH	Negative decadic logarithm of activity of H^+ ions in solution
Pa	Pascale
P	Number of variable parameters
Q	Electric charge
r	Distance or radius
R	Ideal gas constant R = 8.315 … J K^{-1} mol^{-1}
R^2	Coefficient of determination
R_{wp}	Weighted profile factor
R_{exp}	Expected weighted profile factor
s	Second
S	Strain
T	Absolute temperature
U	Potential energy

V	Volt
W	Peak full width at half maximum
x	Space coordinate
z	Number of elementary charges or transferred electrons
α	Transfer coefficient (Butler-Volmer kinetics) or fraction of transformed product (solid state kinetics)
γ	Geometry factor
Γ	Jump rate
Δ	Indicates difference
ε_0	Electric permittivity
η	overpotential
η_L	Lorentz fraction
θ	Diffraction angle
θ_0	Maximum of diffraction intensity
λ	Wavelength
μ	Chemical potential
π	Ratio of a circle's circumference to its diameter $\pi = 3.1415 \ldots$
ρ	Density
σ	Conductivity
φ	Diffraction angle in the imaging plane
ω	Frequency

RÉSUMÉ

Avec les progrès de la microélectronique et le développement subséquent des technologies mobiles à faible coût, les batteries au lithium sont largement utilisées dans la vie quotidienne. Comme elles alimentent en électricité une panoplie d'appareils portables, elles semblent promises à un bel avenir pour répondre aux besoins en énergie de type intermédiaire. Ce secteur regroupe les voitures électriques, les dispositifs tampons écologiques de stockage d'énergie du réseau électrique et autres.

Ces nouvelles technologies nécessitent l'amélioration de la performance des batteries au lithium. Pour que celles-ci soient compétitives avec les méthodes actuelles de stockage d'énergie, p. ex. le stockage chimique de l'électricité produite par combustion et le stockage physique par pompage de l'hydroélectricité, il faut améliorer les technologies des batteries, notamment les vitesses de charge et de décharge, la puissance et la densité énergétique.

La recherche sur les matériaux d'électrodes se situe au cœur du développement des batteries au lithium haute performance. Il y a plus d'une décennie, des chercheurs ont proposé l'utilisation d'une matière céramique à base de phosphate de lithium et de fer ($LiFePO_4$) pour la cathode des batteries au lithium. Ces travaux ont reçu beaucoup d'attention parce que ce composé n'est pas coûteux, sécuritaire et peu nocif pour l'environnement.

Même si la production du $LiFePO_4$ à l'échelle industrielle augmente constamment, ce n'est que récemment qu'on s'est intéressé à ses caractéristiques de charge et de décharge, dont la performance est remarquable. Toutefois, les mécanismes expliquant la rapidité de la charge et de la décharge demeurent évasif. La présente thèse porte sur la cinétique de l'oxydation et de la réduction du $LiFePO_4$, en mettant l'accent sur les limites de transport intrinsèques du lithium.

Les deux premiers chapitres de la présente étude portent sur la détermination des vitesses maximales de charge et de décharge du $LiFePO_4$. On suit les réactions d'oxydation et de réduction chimique par des méthodes *in situ* de photométrie et de diffraction des rayons X. Alors que la photométrie rend possible l'analyse à haute résolution temporelle et l'étude de la forme de la courbe, la diffraction des rayons X permet de sonder directement les propriétés des matériaux et les caractéristiques

dynamiques des changements de phase. Les données indiquent que le $LiFePO_4$ peut être déchargé complètement en quelques minutes et chargé en moins d'une minute. De plus, on constate que la progression de la réaction de décharge n'est pas la même que celle de la charge, ce qui semble indiquer l'existence d'un mécanisme de limitation différent pour ces deux réactions. Les deux premiers chapitres montrent donc que le $LiFePO_4$ ne peut pas être le facteur limitant la vitesse dans les batteries au lithium actuelles.

Le troisième chapitre examine l'application de la diffraction des rayons en synchrotron à la réaction de charge chimique du $LiFePO_4$ induite par un oxydant gazeux, qui met en évidence un changement de phase très rapide. Grâce aux rayons X à forte intensité de l'Advanced Photon Source, des diffractogrammes de grande qualité ont pu être enregistrés *in situ* à une fréquence d'acquisition de 10 Hz. Une analyse détaillée des données obtenues a fourni des informations sur la vitesse de transition de phase, sur la cristallinité de l'échantillon et sur la formation anisotropique d'interfaces. Ces résultats indiquent la formation d'une grande interface entre la phase $LiFePO_4$ riche en lithium et la phase $FePO_4$ pauvre en lithium, qui se dispose préférentiellement de façon perpendiculaire à l'axe cristallographique *a*. Ils montrent aussi la formation de microdéformations significatives quand le $LiFePO_4$ est délithié à très grande vitesse.

Le dernier chapitre de cette étude examine les effets à l'échelle atomique des défauts les plus fréquemment observés dans le $LiFePO_4$. En construisant un ensemble de potentiels pour la modélisation atomistique empirique du système $LiFePO_4/FePO_4$, on a pu analyser la mobilité des défauts antisites du fer dans le $LiFePO_4$ et dans le $FePO_4$. Alors que des études antérieures semblaient indiquer que ces défauts étaient immobiles et que, pour cette raison, ils entravaient la diffusion du lithium, notre étude montre que, même si les défauts antisites du fer sont immobiles dans le $LiFePO_4$, ils manifestent une mobilité significative dans le $FePO_4$. Ainsi, il se peut que dans le système $LiFePO_4$, ils n'entravent la mobilité du lithium que pendant les premiers cycles et qu'ils soient éliminés de la structure au cours des cycles subséquents.

L'objectif principal de cette étude est de lever le voile sur la performance inexpliquée de forte vitesse du $LiFePO_4$. À terme, ces travaux devraient permettre de dresser une feuille de route pour la mise au point de matériaux de batteries performants. Tôt ou tard, ces matériaux connaîtront une forte demande pour les futures applications des batteries au lithium.

Mots-clés : batteries au lithium, $LiFePO_4$, diffusion en phase solide, réactions cinétiques en phase solide, modélisation atomistique.

ABSTRACT

With the advance of microelectronics and the subsequent development of cheap mobile technology, lithium batteries have become ubiquitous in daily live. As they provide portable electric power for so many small devices, they are also considered promising for future intermediary electric power needs. These are electric cars, green electric grid buffer energy storage and others.

These new technologies demand better performance from lithium batteries. Particularly with respect to fast charging and discharging rates, and power and energy density, current battery technology needs to improve in order to compete with traditional power storage, *e.g.* chemical storage in combustion fuel and physical storage in pumped-storage hydroelectricity.

At the center of the development of better performing lithium batteries is battery materials research. More than a decade ago, such research proposed the ceramic material lithium iron phosphate ($LiFePO_4$) as positive electrode material for lithium batteries. It has since received much attention, because it is relatively cheap, environmentally benign, and safe and performs competitively.

Even though it is industrially produced at an increasing scale, its remarkable high rate performance has only recently been discovered. The mechanisms that allow fast charging and discharging of $LiFePO_4$ are still poorly understood. The present thesis investigates the $LiFePO_4$ oxidation and reduction kinetics, with a focus on its intrinsic lithium transport limitations.

The first two chapters are concerned with quantifying the maximum charging and discharging rate of $LiFePO_4$. Chemical oxidation and reduction reactions are tracked using *in situ* photometry and X-ray diffraction. Whereas photometry allows for high time resolution and curve shape analysis, X-ray diffraction probes the material properties and the dynamics of the phase change directly. The data shows that $LiFePO_4$ can be discharged completely within few minutes and charged in less than one minute. Furthermore, the discharge follows a different reaction progress, than the charge, which suggests a different limiting mechanism for the two reactions. These two chapters prove that $LiFePO_4$ cannot be rate limiting in current lithium batteries.

The third chapter applies synchrotron X-ray diffraction to the chemical charging reaction of $LiFePO_4$ induced by a gaseous oxidant, which exhibits a very fast phase change. With the high intensity X-rays of the Advanced Photon Source, high quality diffractograms could be recorded *in situ* with an acquisition frequency of 10 Hz. The resulting data was analyzed in detail, providing information on the rate of the phase transition, the crystallinity of the sample and the anisotropic formation of interfaces. The results show the formation of a wide interface between the lithium rich $LiFePO_4$ phase and the lithium poor $FePO_4$ phase that arranges preferentially perpendicular to the crystallographic *a*-axis. It also reveals significant micro-strains when $LiFePO_4$ is delithiated at ultrafast rate.

The last research chapter concerns the atomic scale effects of the most frequently observed defects in $LiFePO_4$. By synthesizing a set of potentials for empirical atomistic modeling of the $LiFePO_4/FePO_4$ system, it was possible to analyze the mobility of iron antisite defects in $LiFePO_4$ and in $FePO_4$. Such defects have previously been considered immobile and thus hindering lithium diffusion. Our study shows that iron antisite defects are in fact immobile in $LiFePO_4$ but show significant mobility in $FePO_4$. As such, they might hinder lithium mobility in the $LiFePO_4$ system only during the first cycles, but are removed from the structure during subsequent cycling.

The overall goal of this research is to shine light onto the mysterious high rate performance, in order to start sketching a blueprint for fast performing battery materials. Ultimately, such materials will be in high demand for the mentioned future applications of lithium batteries.

Keywords: lithium battery, $LiFePO_4$, solid state diffusion, solid state reaction kinetics, atomistic modeling.

INTRODUCTION

It is a principle of nature, that, whenever you need your mobile device most urgently, it is discharged. Take for example the concert evening, for which you had to leave five minutes ago, but you have to wait until your cell phone is charged to the critical five percent necessary for the babysitter to reach you. For this reason, and some less trivial others, researchers are working to improve battery performance and allow short charging times, down to a few minutes. The present thesis contributes to this effort, by understanding some of the limitations imposed on charging and discharging time by current battery technology.

From cell phones, over electric cars to electric grid energy storage, current state-of-the-art technology relies on lithium ion batteries.(Tarascon & Armand, 2001) These batteries store energy in chemical form in compounds that are hosts to lithium ions. The energy is released by liberating lithium ions from one host and inserting them into the other. During this process the host compounds are oxidized and reduced, exchanging electrons to power external devices. As the battery is charged, the process is reversed and lithium ions return to their initial host. The speed, at which a battery can be charged, is generally limited by the movement of lithium ions and electrons. As such, the chapters following the introduction focus on the movement of ions in one battery material of particular industrial importance to Québec, lithium iron phosphate.

The following introduction will discuss the charging and discharging processes in lithium batteries in more detail, putting an emphasis on diffusion of ions inside the

battery, before going on to describe theoretical and experimental methods employed in this work.

0.1 Lithium batteries

The types of batteries, for which lithium iron phosphate is being developed, can be separated into lithium batteries and lithium ion batteries. In contrast to lithium ion batteries, lithium batteries use metallic lithium as negative electrode, avoiding the use of a host material, as used in lithium ion batteries (Figure 0.1). Both will be discussed together in this section as lithium batteries.

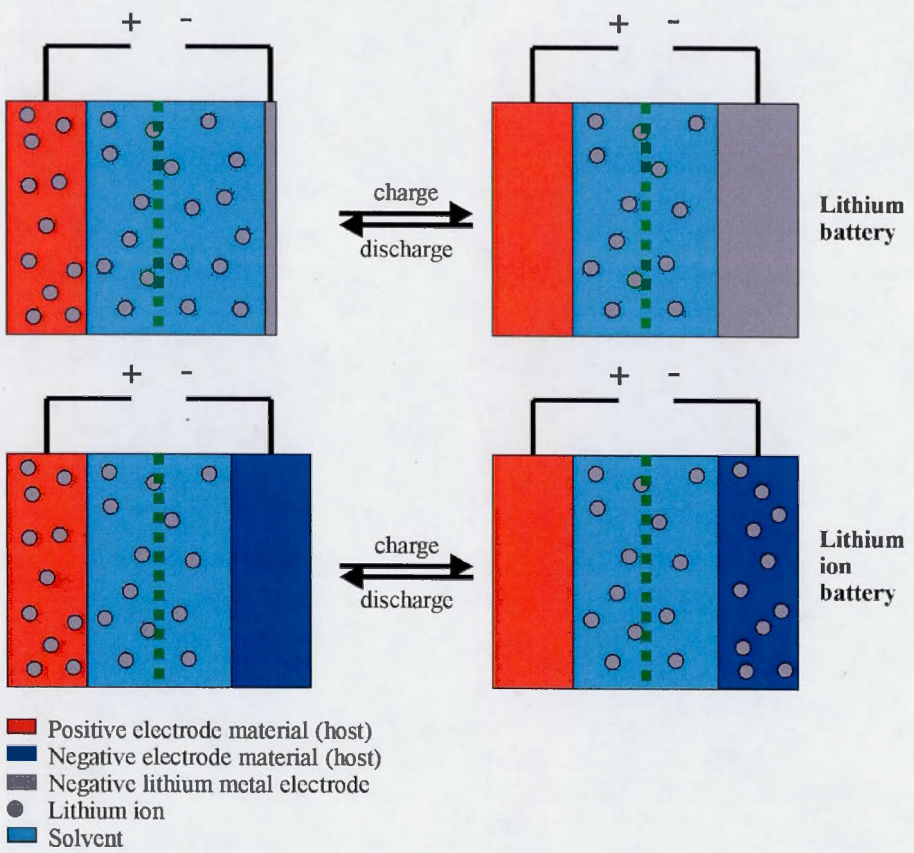

Figure 0.1 Scheme of the general composition of lithium secondary and lithium ion batteries.

In general, lithium batteries consist of a positive and a negative electrode, an electrolyte to achieve ionic connection, and in many cases a separator to avoid electronic short circuit connection between the two electrodes. The positive electrode of a lithium battery is a host material that allows storage of lithium ions. This can be for example an inorganic framework, like lithium cobalt oxide $LiCoO_2$, or the focus of this thesis, lithium iron phosphate $LiFePO_4$, or an organic electronically conductive polymer, as used in the first lithium ion battery.(Yoshino, 2012) The negative electrode consists of lithium metal, in lithium batteries, or of another host material, such as graphite or lithium titanate $Li_4Ti_5O_{12}$ or a lithium alloy, *e.g.* with aluminum in lithium ion batteries. In the discharged state, lithium ions are stored inside the host material at the positive electrode. During charge, a positive potential is applied to the positive electrode, leading to the oxidation of the host material. As electrons are released from the positive electrode material, so are lithium ions to ensure charge compensation. Ions are transported through the electrolyte, electrons through the external circuit towards the negative electrode. There, a negative potential leads to a reduction of lithium ions to lithium metal, or of the host material that intercalates lithium ions. Discharge of the battery reverses these processes. Figure 0.1 summarizes these two technologies.

Both, electron and ion transport, can be rate limiting in a lithium battery. Electrons need to be transported to the reduction or oxidation site in the electrode, while ions need to be transported to the electrode, and into the material. Depending on the material, it may be either ionic or electronic transport, that limits the transport properties of that battery component.(Park, Zhang, Chung, Less, & Sastry, 2010)

Because diffusion plays such a critical role in the charging and discharging dynamics in lithium batteries, some basics of diffusion in general, and solid state diffusion in particular, are presented in the next section, before focusing on the electrode constituents.

0.1.1 Diffusion

The main transport mechanism of ions in battery materials is diffusion. Diffusion is caused by the random movement of mobile species, also known as random walk or Brownian motion. This movement serves to increase disorder, or entropy, in a system, by equilibrating properties like temperature, concentration or chemical potential.

This is best understood considering two adjacent volumes that contain the same particles, but in different concentrations (.2). All particles move randomly in all directions. Since the concentration is larger on the left side, it is more likely that particles cross from the left volume to the right volume, than in the opposite direction. When the concentration is the same over the whole volume, random walk will have no macroscopic effect on the concentration.

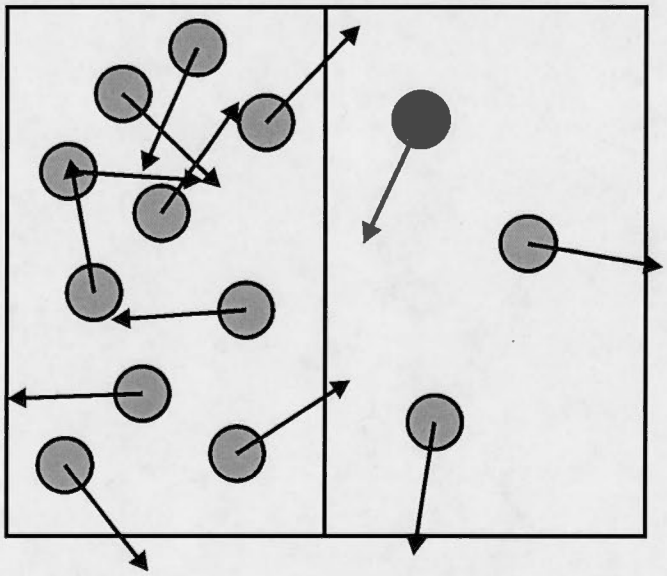

Figure 0.2 Random walk and diffusion

This has first been phenomenologically described by Adolf Fick in 1855.(Fick, 1855) He found the following two relationships, known as Fick's first (0.1) and second (0.2) law:

$$\frac{1}{A}\frac{\partial n}{\partial t} = -D\frac{\partial c}{\partial x} \qquad (0.1)$$

$$\frac{\partial c}{\partial t} = D\frac{\partial^2 c}{\partial x^2} \qquad (0.2)$$

Where A is the area, n is the amount of substance, c is the concentration, t is the time, D is the diffusion coefficient and x is the space coordinate.

This can be further extended to the three-dimensional case, and is more generally also valid for gradients of the chemical potential μ. As the chemical potential is dependent on temperature, concentration, pressure and other environmental variables, gradients of these variables lead to diffusion processes. As can be seen in equation 0.1, a small diffusion coefficient requires a large driving force to obtain the same flux. *I.e.* in a battery, a higher overpotential is necessary to charge at the same rate.

0.1.1.1 Solid state diffusion

Atom diffusion in the solid state is particular, as not all species are mobile. In fact, due to the rigid lattice structure of solids, only structural defects allow atoms to move. As such, the speed of diffusion processes in solids is highly dependent on the availability, or concentration, of these defects.

Above absolute zero temperature, each solid lattice has a finite probability to form lattice defects to increase entropy. A subgroup of such defects are point defects, which are defects that only involve single atomic sites. They include:

i. Vacancies: empty lattice sites,
ii. Interstitials: atoms in between lattice sites, and

iii. Antisites: lattice sites that are filled by atoms of a different kind.

For a stoichiometric solid, only intrinsic defects are possible. Such intrinsic defects are Frenkel defects (pairs of vacancies and interstitials) and Schottky defects (pairs of vacancies).(Wiberg, 1995) In reality, even experimentally stoichiometric materials deviate slightly from ideal stoichiometry, allowing for low concentrations of single vacancy, interstitial and antisite defects.

For diffusion to occur in a solid, such defects have to be mobile. In general, there are two main solid state diffusion mechanisms: interstitial diffusion, *i.e.* an interstitial atom moves from one interstitial site to the next, and vacancy diffusion, *i.e.* a vacancy site moves, by being replaced by neighboring atoms (Figure 0.3).(Borg & Dienes, 1992) In both cases, the environment is very rigid. As such, potential energy wells exist, in which those moving atoms reside, and from which they can jump to the next energy well. The probability of such a jump depends on the vibrational frequency of phonon modes that facilitate the jump, and the energy barrier to overcome:

$$\Gamma = \omega e^{-\frac{\Delta G^{\ddagger}}{kT}}, \qquad (0.3)$$

Whereas Γ is the jump frequency, ω is the vibrational frequency, $\Delta G^{\ddagger}$ is the activation energy or jump barrier, k is Boltzman's constant, and T is the absolute temperature. It can further be shown that the jump frequency Γ of an atom is connected to its diffusion coefficient by

$$\Gamma = \frac{\gamma D}{r^2}, \qquad (0.4)$$

With a geometry factor γ, which is 2 for diffusion in one dimension, 4 in two dimensions and 6 in three dimensions and the jump distance r.

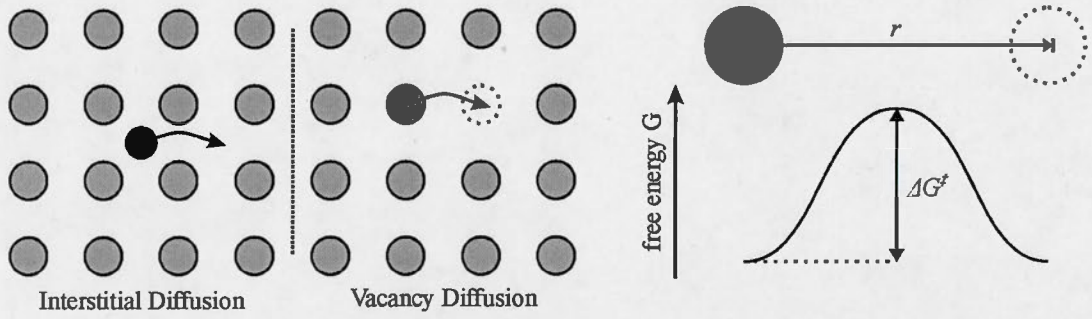

Figure 0.3 Solid state diffusion mechanisms and dimensions

In order to apply the macroscopic Fick's laws to solid state diffusion, one has to consider the defect as the mobile species. As such, the diffusion rate depends on the concentration difference of such defects. Furthermore, in many cases, the activation barrier and vibrational frequencies depend on the direction of the movement. As such, depending on the structure of the solid, diffusion coefficients may be anisotropic.

In summary, an atom that is bound to its lattice site can move only by forming an interstitial defect or by occupying a vacancy. An atom, which has small probability to occupy an interstitial site and does not have neighboring vacancy defects, is restricted to vibrations around its average position and cannot move beyond its lattice unit. As such, defects are essential to solid state diffusion and by extension to charging and discharging rates in batteries.

0.1.2 Positive electrode

Having introduced some of the most essential aspects of diffusion to lithium batteries, this section now returns to the battery components. As the research work in the next chapters is conducted on the positive electrode material $LiFePO_4$, its main goal is to provide the context within which this material is used.

In conventional positive lithium battery electrodes ionic as well as electronic transport takes on a complex three-dimensional shape, known as tortuous path

(illustrated in .4). This is because these electrodes are essentially porous composite materials, consisting of the active host material, an electronically conductive additive, a polymeric binder, that keeps them together, and a current collector, on which this mixture is bound. The composite is additionally penetrated by electrolyte. As such, ionic transport has to follow the electrolyte filled pores inside the composite, while electronic transport follows the electronically conducting additive and active material. While an electrode may be only micrometers thick, the real transport path for ions and electrons may be many times larger. A significant body of research has already been published, addressing the tortuous transport in composite electrodes.(Bae, Erdonmez, Halloran, & Chiang, 2013; Kehrwald, Shearing, Brandon, Sinha, & Harris, 2011; Ren, Armstrong, Jiao, & Bruce, 2010; Vijayaraghavan, Ely, Chiang, García-García, & García, 2012)

Once ions and electrons arrive at the active particle, they are transported inside the active material to the storage site of the lithium ion. Electrolyte and electronically conducting additives are optimized to facilitate ion and electron transport respectively. The active material, however, is optimized to facilitate the storage of ions. As such, this final transport step into or out of the active material is often slow. A shorter transport path in the active material, by reducing particle size thus helps overall (de-)lithiation rate.(Hsu, Tsay, & Hwang, 2004; Okubo et al., 2007)

Two chapters of this thesis use methods to quantify the lithium transport rate in the active material $LiFePO_4$. At this time, it is one of the most studied lithium battery electrode materials.

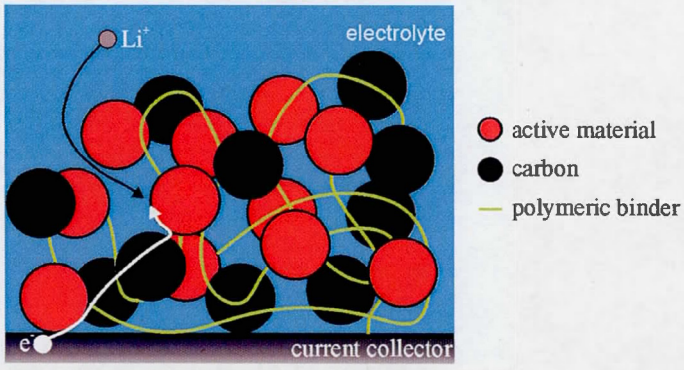

Figure 0.4 Composition of a conventional positive electrode and tortuous path effect of lithium and electron movement.

0.1.2.1 Lithium iron phosphate

$LiFePO_4$ is also known to mineralogists as *triphylite*. It occurs naturally in mixtures with the manganese end member of a iron-manganese solid solution $LiMnPO_4$ *lithiophylite*.(Duda, Rejl, & Slivka, 1998)

The first time $LiFePO_4$ was publicly proposed as a battery material was in 1996, by the research group of Goodenough.(Padhi, Nanjundaswamy, & Goodenough, 1997) Due to the large bandgap, it performed initially only at a fraction of the theoretical capacity, until it was coated with conductive carbon.(Ravet et al., 1999) The resulting patents are owned by Hydro-Québec, and the world wide most important producer of commercial $LiFePO_4$ is still the Quebec spin-off company Phostech Lithium (now known as part of Clariant (Canada), Inc.). As such, further development of this competence remains of great interest to Quebec's economy.

In a lithium battery, $LiFePO_4$ functions as the lithium host material in the positive electrode. As illustrated in Figure 0.1, it releases lithium ions during charge, while iron is oxidized to form $FePO_4$. Particular to this material is that intermediate compositions Li_xFePO_4 ($0 \leq x \leq 1$) are not stable, but separate to two solid phases

with compositions near $LiFePO_4$ and $FePO_4$.(Yamada, Koizumi, Sonoyama, & Kanno, 2005)

This phase separation has detrimental effects on diffusion in $LiFePO_4$. In $LiFePO_4$ only little lithium vacancies exist, while in $FePO_4$ only little interstitial lithium is available. Since these are the mobile species transporting lithium in $LiFePO_4$, the diffusion rate is drastically decreased from a hypothetical complete solid solution system, where all intermediate compositions between $LiFePO_4$ and $FePO_4$ are possible.

In spite of this thermodynamic limitation, some research has shown very good rate characteristics of lithium iron phosphate(Huang et al., 2012; Kang & Ceder, 2009). Many of the theoretical investigations of $LiFePO_4$(P. Bai, Cogswell, & Bazant, 2011; Boovaragavan & Srinivasan, 2011; Cogswell & Bazant, 2012; F. Liu, Siddique, & Mukherjee, 2011; Malik, Zhou, & Ceder, 2011; Meethong, Huang, Speakman, Carter, & Chiang, 2007) and some experimental studies(Delmas, Maccario, Croguennec, Le Cras, & Weill, 2008; Kao et al., 2010; Orikasa, Maeda, et al., 2013b; Sharma et al., 2012; Srinivasan & Newman, 2004; X. Yu et al., 2012) have focused on this discrepancy, producing different models.

One of the first models, describing the charge/discharge process in a single $LiFePO_4$ particle is the shrinking core model (Figure 0.5, top).(Srinivasan & Newman, 2004) It was developed in the Newman group in 2004 to simulate the electrochemical behavior of $LiFePO_4$ electrodes. In this model, the growing phase is expected to propagate from the particle surface towards its center. It was later rejected, because others predicted and found highly anisotropic lithium diffusion.(Islam, Driscoll, Fisher, & Slater, 2005; Nishimura et al., 2008; Shi et al., 2009) Their results indicated that lithium mobility is orders of magnitude higher in the crystallographic *b* axis. The domino cascade model,(Delmas, et al., 2008) published in 2008, accounts for this anisotropy and henceforth attracted much

attention (Figure 0.5, center). It describes a linearly growing phase, where lithium mobility is facilitated by a strained interface between $LiFePO_4$ and $FePO_4$ which allows for interstitial diffusion. Finally, the latest theoretical papers question this model that was based on *ex situ* observations. Different modeling techniques suggest a kinetic pathway, that suppresses phase separation and allows for a phase transition between $LiFePO_4$ and $FePO_4$ in a solid solution of the two, (Figure 0.5, bottom) (P. Bai, et al., 2011; Cogswell & Bazant, 2012; F. Liu, et al., 2011; Malik, et al., 2011) while other studies suggest the formation of different interfaces, during spinodal decomposition combined with a domino cascade type mechanism.(Dargaville & Farrell, 2013; Ichitsubo et al., 2013)

Experimental *in situ* studies show different types of behavior. With *in operando* TEM a sharp phase boundary between $LiFePO_4$ and $FePO_4$ can be observed upon slow discharge / lithium insertion into $FePO_4$.(Y. Zhu et al., 2013) However, to overcome the limitations of a TEM environment, this study had to work with a solid electrolyte which had only a small contact area with the studied particle. As such, it might not be representative for the behavior in a battery. Synchrotron X-ray diffraction and X-ray absorption data, recorded during battery cycling at different rates and with different particle sizes, was recently reported in several publications by Orikasa and co-workers.(Orikasa, Maeda, Koyama, Minato, et al., 2013; Orikasa, Maeda, et al., 2013a, 2013b) These results show the formation of a metastable phase during the first insertion of lithium into $FePO_4$ that becomes more pronounced at fast cycling and appears to be Li_xFePO_4 with $0.6 \leq x \leq 0.75$. This phase slowly disappears upon relaxation. Furthermore, the solid solution limits of Li in $FePO_4$ and vacancies in $LiFePO_4$ are extended compared to the thermodynamic values, particularly for small 60 nm particles.

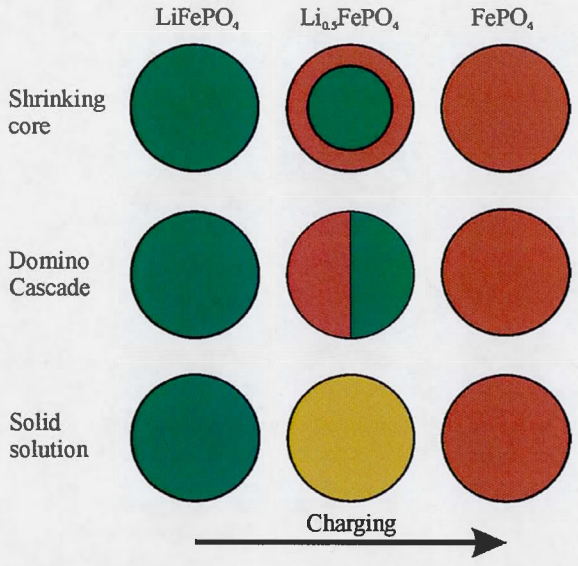

Figure 0.5 Kinetic single particle models of lithium iron phosphate.

To date, experimental evidence for the domino cascade and the solid solution model as well as more complicated mechanisms have been presented. No one model can yet be conclusively confirmed true, and research on this issue continues.

0.1.3 Other battery components

While this thesis focuses on $LiFePO_4$, this material functions as energy store only in the context of a complete battery, in which other components need to allow fast ion transport as well. In the electrolyte, ions move inside the pores of the positive composite electrode, through the separator, and through the pores of the negative electrode. At the negative electrode, ions need to be intercalated / deintercalated, or lithium metal needs to deposit / dissolve. Each one of these steps can limit the cycling rate of the battery.

As seen in section 0.1.1, ion transport rate can be increased by increasing the driving force, *e.g.* the overpotential. For charging, this means in theory, by increasing the charging voltage, the battery can be charged quicker. However, the electrolyte has

only a limited electrochemical potential stability range, known as the electrochemical window of the electrolyte. For the most common liquid lithium containing battery electrolytes, which are salts in mixtures of organic carbonates, this window extends to about 4.5 V *vs* Li/Li^+ on the oxidizing side, and to about 1.2 V *vs* Li/Li^+ on the reducing side.(Xu, 2004) Charging or discharging beyond these potential limits leads to significant side reactions at the positive electrode, that consume electrolyte and may form products that are harmful to the battery.

Since the cathodic stability of many such carbonate electrolytes does not extend below 1 V *vs.* Li/Li^+ these solvents decompose partly at the negative electrode, which commonly exhibits a potential below 1 V *vs.* Li/Li^+. The decomposition products form a solid electrolyte interface (SEI) at the negative electrode. Under the right conditions, it can passivate the electrode to avoid further electrolyte decomposition. This process has been studied extensively.(S. S. Zhang, 2006)

In addition to liquid organic electrolytes, aqueous electrolytes have been investigated.(Winter, Besenhard, Spahr, & Novák, 1998) Since water has a small electrochemical window, such electrolytes are only stable to a maximum 1.5 V cell voltage, and would not be able to be used with negative electrode materials, that have a low potential *vs.* Li/Li^+. As such, even though aqueous electrolytes exhibit much better ionic conduction, they are of little interest for applications that require large specific energy.

Instead, research has been directed to improve electrochemical stability. Much more stable are for example most solid electrolytes. These may be salts, ceramics, or polymers. The more rigid solid structure, however, decreases ionic conduction even further.(Fergus, 2010) The gain in potential window is thus often overcompensated by the reduction in diffusion coefficient. Such batteries are often heated in order to improve conductivity to make them practical.

While the separator is not an active component of the battery, its properties may nevertheless impact battery performance significantly. Its purpose is to avoid electronic contact between the two electrodes, while allowing unhindered ion mobility. As such, it is redundant when using solid electrolytes. To perform well, it must be micro-porous and thin, but mechanically strong, to allow for good ionic conductivity.(S. S. Zhang, 2007) Furthermore, it should not degrade in the battery, remain effective during thermal failure, and be cheap.

This is to show, that finally all battery components contribute to ion transport. As such, slow charging and discharging rates may be limited by any of the battery components. Consequently, *all* elements need to be considered when optimizing overall battery performance.

0.2 Predictive and analytical theoretical methods

With this short introduction into lithium batteries, it becomes clear that the combination of ionic and electronic transport processes can be quite complex. In order to understand, quantify and predict experimental results arising from such processes, a number of theoretical techniques are available. Some of these models also found application in the following research chapters. The next two sections will provide the basics of these approaches.

0.2.1 Empirical atomistic modeling

Chemical theoretical models can be classified by system size. They range from electronic structure calculations, that may be used to model electronic and atomic scale effects, to macroscopic continuous models, that are suited to simulate the effect of bulk structures on whole batteries.(Yip, 2005)

Increasing model scale from electronic structure calculations, one passes next to the atomic level, as applied in empirical atomistic modeling. The smallest modelled element of an empirical atomistic model is an atom, or in certain cases an atomic core

and its electronic shell. At this scale, all interactions are based on Newtonian mechanics, neglecting relativistic and quantum effects.

The interactions between atoms are modeled by different empirical potential energy functions, or potentials, most notably the Coulomb potential, Morse potential, Buckingham potential and Lennard Jones potential.(Gale & Rohl, 2003) All of these potentials are pair potentials, *i.e.* the interaction of two atoms is only defined by the nature of these atoms and their distance. Additionally, other potentials exist, that describe the interactions of three or more atoms. They are sometimes necessary to correctly model angles and coordination dependent interactions.

0.2.1.1 Potential energy functions

In this work, only the Coulomb potential, the Buckingham potential, and a harmonic oscillator potential were required to observe sufficient correlation between the model and physical data. The Coulomb potential takes on the mathematical form

$$U = \frac{1}{4\pi\varepsilon_0} \cdot \frac{Q_1 Q_2}{r}, \qquad (0.5)$$

Where U is the potential energy, ε_0 is the electric permittivity, Q_1 and Q_2 are the charges of the first and the second ion, respectively, and r is the distance between the two.

The Coulomb potential is always attractive for charges of opposing sign, and goes towards negative infinity as the distance goes to zero. This runs counter the knowledge, that the atomic electron clouds repulse each other at small distance. The Buckingham potential,(Buckingham, 1938) on the other hand, has an attractive and a repulsive part. As such, the Buckingham potential can be added to a Coulomb system, to add a short range repulsive force, or stand alone, *e.g.* in a non-ionic model. The Buckingham potential takes on the form

$$U = A_B e^{-r/\rho_B} - \frac{C_B}{r^6}, \quad (0.6)$$

Where A_B, ρ_B, and C_B are constants, specific to the modeled interaction.

In some cases it is not sufficient to model the interactions between atoms and ions, but the polarizability of atoms and ions has to be taken into account as well. In this case, ions or atoms can be split into a solid core, which contains the mass, and a massless electron shell. This is called a shell model.(Dick & Overhauser, 1958) Coulomb forces are acting on both core and shell, while the short range repulsive interactions are acting on the shell only. To bind shell and core together, a harmonic spring potential is applied between the two:

$$U = \frac{1}{2} k_s r^2, \quad (0.7)$$

Where k_s is the spring constant, and r is the distance between core and shell.

By adding the pairwise potentials of all involved atoms, it is possible to get the potential energy of the system. For geometry optimization, its derivatives with respect to the atomic coordinates (*i.e.* the forces acting on each atom) are then calculated. By minimizing the forces per atom, the zero temperature equilibrium structure of the system can be obtained.

In solids, these interactions can be efficiently determined for an infinite periodic structure, by making use of symmetry operations. To this end, crystalline solids can be classified by the applicable symmetry operations into space groups. Common to all space groups is the simple translation of the repetition unit, or unit cell, in all directions. A change in periodic structure comes with a change in the systems energy. From this energy change and other structural information, properties like elastic constants and dielectric constants can be obtained.

0.2.1.2 Modeling point defects

To investigate diffusion of atoms inside solids, the periodic structure needs to be broken. Two approaches are used to perform this type of calculations.

An increase in the system size to multiple unit cells is called a supercell approach (.6, left). The supercell is chosen at a size, where it is too large for a defect to interact with its image in the next periodic cell. This approach is particularly useful, if a system contains a large concentration of defects. To this end, several defects can be placed in one supercell. As such, defects within one unit cell can be placed close to each other, where they interact.

A complete removal of periodicity to model defects is called a cluster approach. One such method, that is used frequently to model point defects in periodic solids, is the Mott-Littleton approach (.6, right).(Mott & Littleton, 1938) The periodic crystalline solid is modeled first. Then the defect is placed in the center of a spherical extract of the periodic solid. Up to a radius r_1, called region 1, this extract is relaxed explicitly, as would be done in a geometry optimization. Between r_1 and r_2, region 2a, atoms are relaxed within a harmonic approximation of the given potential function to reduce computational cost. Beyond r_2, region 2b, atoms are fixed to their position in the crystalline solid. Structural effects are thus assumed to be limited to region 1 and region 2a.

For both methods, by comparing the energies obtained from the crystalline solid, and the solid containing the defect, a defect energy can be obtained. This energy represents the work, necessary to form this defect from a crystalline solid.

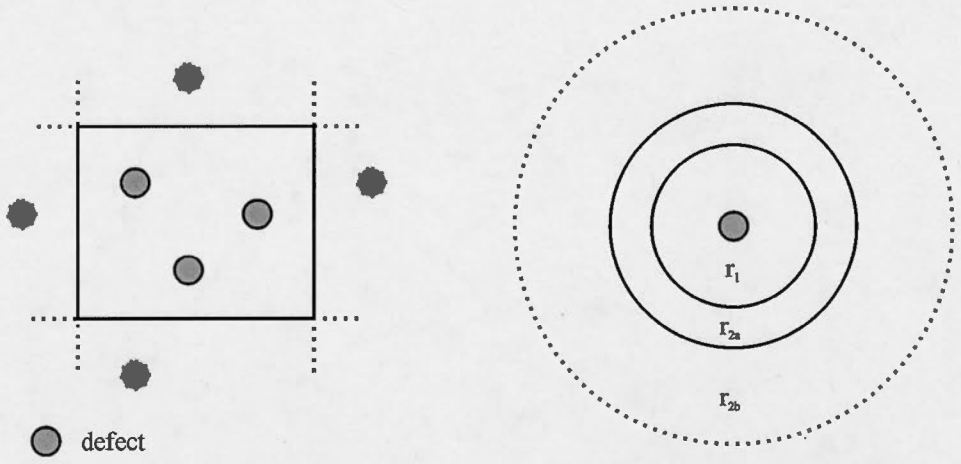

Figure 0.6 Two methods of point defect calculations in molecular modeling: the supercell method, and the cluster approach after Mott and Littleton. Point defects are displayed as grey circles.

In order to obtain diffusion trajectories and activation barriers, the moving defect atom can be fixed in one axis, so that it can relax only in two dimensions. This axis is commonly chosen to be the shortest path between the two equilibrium sites. As such, discrete defect geometries and energies along the trajectory are probed. Increasing the number of such calculated geometries, it becomes less likely that a local energy minimum along the trajectory is missed. Plotting the energy versus the displacement from the original position, the energy barrier for one diffusion step is obtained.

0.2.2 Solid state kinetic models

Different from atomistic models, that provide insight on the atomic scale, are solid state kinetic models. Here, the modeled size is drastically increased to describe events on the particle or bulk scale. Solid state kinetic models are used to describe experimentally obtained reaction progress. As such, they commonly take different limiting processes into consideration, such as nucleation of a new solid phase, reaction kinetics, and diffusion of species in the solid.(Khawam & Flanagan, 2006)

Two such models have been applied frequently to study the phase transition and lithium transport in $LiFePO_4$: the Avrami model,(Orikasa, Maeda, Koyama, Minato, et al., 2013; Oyama, Yamada, Natsui, Nishimura, & Yamada, 2012) based on nucleation-growth considerations, and phase-field models,(P. Bai, et al., 2011; Ichitsubo, et al., 2013) which model spinodal decomposition, emphasizing the influence of diffusion and interfacial strain.

0.2.2.1 The Avrami equation

A nucleation-growth-ingestion law for the progress of solid state reaction was made popular around 1940 by Melvin Avrami in a series of publications in The Journal of Chemical Physics.(Avrami, 1939, 1940, 1941) It considers:

i. an original density of possible nucleation sites,
ii. an activation barrier for the formation of growth nuclei from these nucleation sites,
iii. an activation energy for the growth of the nucleus, and
iv. the ingestion of growth nuclei and nucleation sites, by other growth nuclei.

The reaction is tracked by the volume fraction of transformed product α, whereas the time dependence of α becomes

$$\ln(1-\alpha) = (k \cdot t)^{n_a} . \quad (0.8)$$

Here, t is the time, k is a rate constant and n_a is the Avrami exponent.(Khawam & Flanagan, 2006) This exponent can take on values between 0.5 and 4 and varies with the rate limiting mechanism of the reaction.

Commonly the Avrami exponent is unknown, so that it becomes practical to plot $\ln[-\ln(1-\alpha)]$ *vs.* $\ln(t)$. A linear fit then provides the Avrami exponent n_a as the slope and $n_a \ln(k)$ as the intercept with the ordinate.

The Avrami model does not unambiguously ascribe one limiting mechanism to one Avrami exponent. As such, no one single mechanism can be deduced solely from the Avrami exponent. However, the model can be used to exclude certain limiting mechanisms, and in concert with other techniques may assist in identifying the limiting step of a solid state reaction.

Another application of the Avrami model to solid state reaction data is the analysis of rate constants. As such, different rate constants of the same reaction can be compared, even if the limiting mechanism is unclear, as long as the Avrami exponent remains unchanged. Such investigations include the determination of the activation energy for the rate limiting process.

One significant limitation of the Avrami model is that it assumes a two phase reaction with a sharp phase boundary. For many solid state reactions, this is adequate, as the phase boundary often is not significant in comparison to the grain size. For typical lithium battery materials, this may be different. Particularly, most lithium battery materials are host structures that only slightly expand and compress upon lithium insertion and deinsertion, but do not completely reorganize the structure. In fact, small mismatches between the lithiated and delithiated phases are often seen as requirement to avoid particle fractures upon cycling, which lead to capacity fading. As such, extended solid solutions between the products of the solid state reactions in lithium battery materials are likely, which reduces applicability of the Avrami model.

This complexity has resulted in the application of new more complex phase field models to battery research, and the investigation of the phase transformations and kinetics of battery materials. These respect the kinetic possibility of extended solid solution, and concurrent reaction progress and phase separation in a diffuse interface. They commonly include consideration for interfacial strain as well. The Avrami models are then just a subset of phase-field models, assuming fast localized spinodal

decomposition, that produce growing nuclei. Sections 5.1 – 5.3 discuss the thermodynamics of these processes in more detail.

Both, Avrami and phase field models, were applied successfully to the reaction progress in $LiFePO_4$.(P. Bai, et al., 2011; Ichitsubo, et al., 2013; Orikasa, Maeda, Koyama, Minato, et al., 2013; Oyama, et al., 2012) Since the simplistic Avrami model already reproduces the experimental data well, it is not surprising that the more complex models are equal or surpass those fits. As such, it is unwise to deduce a limiting mechanism from such models. Thus, it seems, only direct *in situ* observations are able to solve this mystery.

0.3 Experimental techniques

The following research chapters report one approach to make such observations, using several experimental techniques. Direct *in situ* observation of the phase change was possible through X-ray diffraction. Other techniques were used to characterize the involved reactions and materials.

0.3.1 Electrochemical techniques

It goes without saying, that electrochemical methods are fundamental to study lithium batteries. The essential charge storing processes in the battery are electrochemical. Thus, electrochemistry can be used to study them, and their kinetic limitations.

0.3.1.1 Electrochemical fundamentals

Electrochemical thermodynamics is controlled by the ubiquitous Nernst equation (Bard & Faulkner, 2001):

$$E = E^{\circ} + \frac{RT}{zF} \ln\left(\frac{a_{ox}}{a_{red}}\right), \quad (0.9)$$

Whereas E is the electrochemical potential, the ° denotes standard conditions, R is the ideal gas constant, T is the temperature in Kelvin, z is the number of exchanged electrons in the reaction, F is Faraday's constant, and a_{ox} and a_{red} are the activities of the oxidized and reduced species of the reaction respectively.

Nernst's equation describes the thermodynamic drive of an electron exchange reaction. For a redox reaction to take place spontaneously, the electrochemical potential of the oxidation must be smaller than the potential of the reduction reaction. As other thermodynamic potentials, the electrode potential depends on concentrations or activities of involved species and the temperature.

Given that electrode potentials cannot be measured directly, they cannot be provided as absolute values. Instead they are given with respect difference to a reference electrode, such as the normal hydrogen electrode (NHE). This is the hydrogen reduction reaction from acidic solution, defined at pH = 0 and a hydrogen gas fugacity of 1. In lithium batteries, instead, the Li/Li^+ redox couple is often used as reference.

In this context, the oxidation reaction of $LiFePO_4$ is:

$$LiFePO_4 \rightarrow Li^+ + FePO_4 + e^- \qquad [0.1]$$

In a lithium battery with lithium metal negative electrode, the corresponding reduction reaction is:

$$Li^+ + e^- \rightarrow Li \qquad [0.2]$$

Given an electrode potential of about -3 V *vs.* NHE for the lithium reduction, and about + 0.4 V *vs.* NHE for the $LiFePO_4$ oxidation, this reaction is not spontaneous, but requires external work. As such, the reactions [0.1] and [0.2] describe the charging process of the lithium battery. In discharge, the spontaneous reaction,

lithium metal is oxidized and $FePO_4$ is reduced, while the resulting electron flux, or current, is used to power external devices.

An electrochemical reaction can also be characterized by its reaction rate. For electrochemical reactions at an electrode, the Butler-Volmer equation is commonly applied, which results from activation considerations, similar to transition state theory in chemical kinetics. As such, activation energy is necessary to transfer an electron from the electrode to the substance in solution. Up to a certain thermodynamic driving force, or applied overpotential, the reaction rate is thus determined by the activation barrier. The Butler-Volmer treatment of this consideration results in

$$i = i_0 \left(e^{\frac{\alpha \eta F}{RT}} - e^{\frac{(1-\alpha)\eta F}{RT}} \right), \quad (0.10)$$

Where i is the current, i_0 is the exchange current, α is the transfer coefficient, which ranges between 0 and 1, η is the overpotential, *i.e.* the potential difference from the equilibrium potential of the process, F is the Faraday constant, R is the ideal gas constant and T is the absolute temperature in Kelvin.

Increasing the overpotential, *i.e.* the thermodynamic driving force, further, the reaction rate becomes diffusion determined. As diffusion rate is independent of the potential at the electrode (assuming the electric field rapidly decays in the electrolyte, so that migration can be neglected), increasing the overpotential when reaching the diffusion limit has no influence on the reaction rate. The current behavior, when reaching diffusion limit, is solely determined by Fick's laws, and analytical solutions to Fick's law can provide the current for specific situations, *e.g.* Cottrell law for a potential step at a planar electrode.

Considering this impact of diffusion on the current at high overpotentials, it becomes clear that the diffusion rate is a determining factor for the high rate performance of battery materials.

0.3.1.2 Research batteries

The most often used method to test battery materials electrochemically is the production of research batteries. These exist in different forms, like pouch cells or coin cells, but essentially are built very similarly. For $LiFePO_4$/Li cells with liquid electrolyte, the positive electrode material is mixed with an electronic conductor, and a polymeric binder to form a paint-like paste.(Marks, Trussler, Smith, Xiong, & Dahn, 2011) This paste is applied to form a thin layer of specified thickness on a current collector, commonly aluminum foil. The electrode is then dried, and may be calendared to reduce the electrode thickness and improve electronic connectivity. At that stage it can be introduced into an inert atmosphere, commonly argon gas, to avoid lithium and electrolyte corrosion, and is assembled with a polymeric separator and lithium metal negative electrode. Before closing and sealing the battery housing, *e.g.* the aluminum casing of a coin cell, the electrolyte is added.

The assembled battery can then be subjected to electrochemical tests. Most commonly, the battery is discharged and charged repeatedly at a constant current, which is called galvanostatic electrochemical cycling. By changing the current, the rate performance of the battery can be evaluated. Given the known composition of the electrode paint, the size of the electrode, and its weight, the battery capacity can be normalized by the weight of active material in the positive electrode. If the battery composition is chosen, so that the positive electrode material limits its capacity, this normalized battery capacity is a measure of the achieved capacity of the positive electrode material.

The thermodynamic capacity limit of a battery is easily designed to be the positive electrode active material. At very low rates, the thermodynamic capacity of one material can thus be extracted. The kinetic limit, however, is much more difficult to understand. Judging the kinetic performance of a single material from the

performance of its battery is difficult, and requires careful evaluation of all current and electron conducting materials in the complete battery.

Other electrochemical techniques are more suitable to probe different kinetic events in a battery, and are as well applied. In the literature, different research groups used impedance spectroscopy,(Schmidt et al., 2011) galvanostatic intermittent titration,(Y. Zhu & Wang, 2010) and other techniques(P. Yu, Popov, Ritter, & White, 1999) to evaluate rate performances and lithium conduction mechanisms of batteries.

0.3.1.3 Chemical redox reactions

As just explored, electrochemical techniques are problematic in determining the kinetics of an active electrode material, since the measured kinetics are a convolution of all kinetic contributions in the electrochemical cell. In a chain, these include electronic conduction at the anode, diffusion in the anode material (if it is an intercalation compound), faradaic process at the anode, diffusion in the electrolyte, faradaic process at the cathode, diffusion in the cathode material (if it is an intercalation compound) and electronic conduction at the cathode. Every single step in this chain may limit the overall kinetics.

Chemical redox reactions exhibit a much simpler kinetic chain, including only redox agent and lithium diffusion in the matrix, surface reaction kinetics and diffusion in the active material. They can mimic the electrochemical response of the active material to an electric potential and by designing the experiment appropriately, the reaction rate can be determined by the lithium dynamics in the active material. In order to do so, the chemical redox agent needs to (de)lithiate the active material, without modifying it in a different way. *E.g.* Chapter II will show that the oxidant ozone cannot significantly delithiate $LiFePO_4$, but instead the material is slightly modified at the surface, whereas the oxidant NO_2 delithiates $LiFePO_4$ completely, without any significant change to the $FePO_4$ framework.

If the only observable reaction of the active material to the redox agent is lithium (de)intercalation, then the reaction is suited to mimic the electrochemical (dis)charging. Since neither the applied electric potential nor the redox agent penetrate significantly into the active material, lithium dynamics inside the bulk material are only determined by the lithium concentration in the active material's surface layer. In order to investigate the bulk lithium transport kinetics, contributions from diffusion in the matrix and surface reaction kinetics to the overall measured reaction rate need to be excluded. Both these contributions commonly are proportional to the redox agent concentration, whereas the lithium surface concentration shows little dependence on it. As such, in the absence of a reaction rate dependence on the redox agent concentration, the measured kinetics are those of the bulk active material.

0.3.2 Infrared Spectroscopy

In addition to performance characterization, battery materials need to be characterized chemically. Infrared spectroscopy is among the most efficient techniques for this purpose, due to simple sample preparation and low cost equipment.

As other spectroscopic techniques, infrared spectroscopy excites discrete energetic states of the material using electromagnetic radiation, in this case in the infrared spectrum. The excitation energy can be extracted from the energy dependent absorption of the infrared excitation light. The energetic transitions occur between vibrational and rotational states of the atomic structure. Excitation with infrared light, thus leads to the stimulation of vibrational motions of atoms in the material. In a solid state material, the energetic state of a vibration is called a phonon.

The energy, of these transitions is often highly dependent on the chemical state of the material. Depending on the local environment of functional groups in a material, *e.g.* the phosphate group in $LiFePO_4$, the vibrational energies change. As

such, infrared spectroscopy is a sensitive tool to probe local changes in the chemistry of battery materials.

Technically, infrared spectroscopy can be realized with different technologies and geometries. Therefore, it is classified by how the absorption at different wavelengths is obtained. Classically, a polychromatic infrared light is filtered by wavelength in a monochromator, which then scans through the different available light energies. During this process, much of the infrared excitation light intensity is removed. Fourier transform infrared (FTIR) spectroscopy employs an alternative method, to reduce this intensity loss and thus improve signal to noise ratio. In this technique, a Michelson interferometer is used to introduce wavelength specific destructive interference between two identical, but time-shifted, polychromatic infrared beams. Scanning the time difference between the two beams, one obtains an interferogram in the time domain that can be converted to a spectrum in the frequency domain by Fourier Transformation.

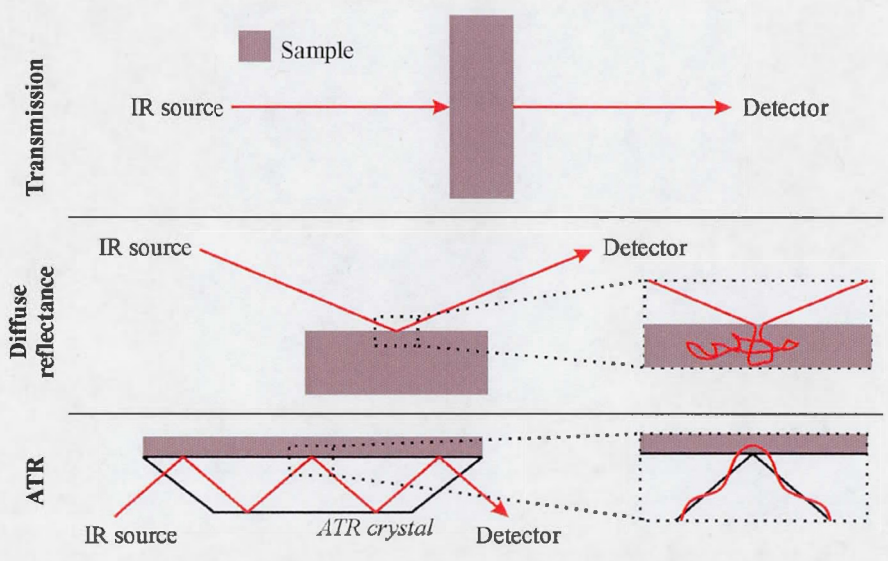

Figure 0.7 Infrared spectroscopy absorption geometries. The red line illustrates the infrared light and grey shading the sample.

Infrared spectroscopies are also classified by the geometry of the absorption step (Figure 0.7). Three common techniques are transmission, diffuse reflectance and attenuated total reflectance (ATR) infrared spectroscopy. In transmission, infrared source, sample and detector are in one line. As such, infrared light has to pass through the complete sample to reach the detector. For powdered solid state samples, it is common to disperse the sample in a salt with little infrared absorption, *e.g.* KBr. Infrared spectra from powdered samples can as well be obtained in diffuse reflectance, where infrared light is reflected from the powder before it is detected. Finally, the infrared beam can be reflected internally from a crystal. At high incidence angle, above a critical angle determined by the refractive indices of the crystal and its environment, the infrared light is totally reflected. Similar to quantum tunneling of electrons, the wave function of photons that are totally reflected on an interface extends into the second medium with an exponential decay. If a third medium, *i.e.* the sample, is close enough, energy can be absorbed by it. This technique is called ATR infrared spectroscopy. Thus, depending on the geometry of the absorption step, the bulk material (transmission) or the sample surface (ATR) can be probed.

Early on, the effect of lithium deintercalation from $LiFePO_4$ on its infrared spectra was studied,(Ait-Salah et al., 2006; Burba & Frech, 2004) and the technique is now frequently employed to test for lithium deintercalation, and other chemical changes to $LiFePO_4$.(Hamelet et al., 2009)

0.3.3 Electron Microscopy

Electron microscopy is complementary to infrared spectroscopy. Whereas infrared spectroscopy probes the chemical environment, common electron microscopy probes its physical state (aside from some specialized detectors). For this purpose, a focused electron beam may be scanned across the surface (scanning electron microscopy, or SEM) or, electrons may be transmitted through the sample

and an image is produced through their absorption by the sample (transmission electron microscopy, or TEM).

Compared to standard optical microscopy (bright field microscopy), electron microscopy can naturally achieve higher resolution. The resolution limit of bright field microscopy is determined by light diffraction, which interferes most strongly when the imaged features become smaller than the light wavelength. Consequently, X-ray microscopy is the highest resolution microscopy technique, using electromagnetic waves. However, X-rays interact only little with samples, and interaction decreases with increasing X-ray energy. On the other hand, low energy X-rays are difficult to obtain at high intensity. As such, most applied X-ray microscopy is now conducted at synchrotron light sources.(Sakdinawat & Attwood, 2010) This requires high intensity X-rays and highly sensitive X-ray detectors. Electrons can achieve the same wavelengths, but interact much stronger with samples, and are easier to obtain at controlled energies and intensities than X-rays. As such, electron microscopy is much more commonplace in materials characterization today.

The most general elements of an electron microscope include an electron source, which expels and accelerates electrons in an electric field. Electromagnetic lenses then focus and guide the electron beam. After it interacts with the sample, a signal is detected by a detector. In SEM, this is a point detector, and the image is produced by moving the beam across the sample. In TEM, the detector is an area detector, which directly records the image.(Goldstein et al., 2003; Williams & Carter, 2009)

Depending on the geometry, SEM or TEM, and the detector, image contrast has different origins. In imaging mode of TEM, contrast can be due to sample thickness, atomic weight of sample elements and electron diffraction by a crystalline lattice.(Williams & Carter, 2009) In SEM, different detectors exist to detect electrons from different origins. Secondary electrons are expelled from atoms in the sample upon impact of the primary electron beam similar to photoelectrons in the XPS

technique. The respective secondary electron (SE) detector produces topographical images of the sample surfaces: holes and edges are more easily seen in SE images. Backscattered electrons, on the other hand, are elastically scattered from the sample, *i.e.* they do not transfer energy to the sample. A backscattered electron detector commonly produces images, whose contrast depends on the elemental composition of the sample. High atomic number elements lead to darker contrast, while lighter elements also show lighter contrast.(Goldstein, et al., 2003)

Additionally, TEM can be employed to obtain electron diffraction patterns. The diffraction principles are the same as in X-ray diffraction but can be applied to a microscopic sample. As such, the crystalline structure of a sample can be probed in detail.

Taken together, electron microscopic techniques are powerful tools to investigate the microscopic structure of battery materials. A recent study even employed TEM to investigate the single particle discharge mechanism of $LiFePO_4$ at low rate.(Y. Zhu, et al., 2013) Electron microscopy also played a significant role in the derivation of the Domino Cascade model.(Brunetti et al., 2011; Delmas, et al., 2008) When interpreting electron microscopic data, the effect of the vacuum environment and the small sample size should be taken into consideration.

0.3.4 X-ray photoelectron spectroscopy

In $LiFePO_4$ and other lithium battery electrode materials lithium ion transport passes two distinct steps: the material bulk and the surface or interface. As such, surface characterization techniques can be of immense interest to the study of lithium transport in battery materials. X-ray photoelectron spectroscopy (XPS) is one such surface sensitive technique.

In XPS, a sample is irradiated with X-rays. Those X-rays penetrate the sample and interact with electrons in the sample. X-rays are able to eject electrons in near

core electron shells, *i.e.* the K and the L shell. These electrons can be detected, and their kinetic energy depends on the originating shell, the specific element, and the chemical environment.(Ratner & Castner, 2009)

As such, the elemental composition and chemical bonding that is present at the surface of a sample can be determined. Since the ejected electrons are easily absorbed by the sample following the exponential Beer-Lamberts law, only surface near photoelectrons are detected. XPS has been applied to study the electronic structure of $LiFePO_4$,(Castro et al., 2010) which likely has significant impact on the mobility of lithium in the material.(Ong, Chevrier, & Ceder, 2011)

0.3.5 X-ray diffraction

The go-to technique for structure determination of solid state materials is X-ray diffraction. Just as electrons in electron microscopy, wavelengths of X-rays are similar in value to nearest neighbor atomic distances. Since X-rays propagate as waves, they are bent by obstacles such as the electronic shells of atoms. In periodic structures, this leads to constructive and destructive interference between the periodically bent X-rays, which, in turn, leads to diffraction patterns.(Waseda, Matsubara, & Kozo, 2011)

0.3.5.1 Theory of X-ray diffraction

The angular dependence of constructive interference maxima on lattice distances in periodic solids underlies Bragg's law.

$$n \cdot \lambda = 2d \sin\theta \ , \quad (0.11)$$

Where n is the order of the maximum, which is one for the nearest neighbor plane spacing, λ is the X-ray wavelength, d is the spacing between atomic planes and θ is the diffraction angle. (Figure 0.8)

Using Bragg's law, one can determine the distance between atomic planes, or lattice distance, from the angular deflection of a diffraction maximum from the original X-ray beam. As these planes consist of periodically spaced atoms, there are a large number of planes to consider for each periodic solid. Depending on selection rules, each plane may lead to diffraction reflexes and add to the number and intensity of diffraction spots. The diffractogram of a single crystal will form a large number of diffraction spots. Picturing an imaging plane behind the sample (Figure 0.9) the location of a diffraction spot can be determined with two angles: the diffraction angle (2θ) of a spot is determined by the corresponding lattice distance, and its angle in the imaging plane (here called φ) is determined by the orientation of the lattice (and thus the crystal) in space. In a diffractogram of a powder, crystals are oriented in all directions; as such 2θ remains the same for each particle, but φ changes. Instead of diffraction spots, diffraction rings at constant 2θ are the result. As such, in powder diffractograms with unpolarized X-rays, the diffraction intensity is only dependent on the diffraction angle 2θ, commonly displayed in intensity-2θ diffractogram plots.

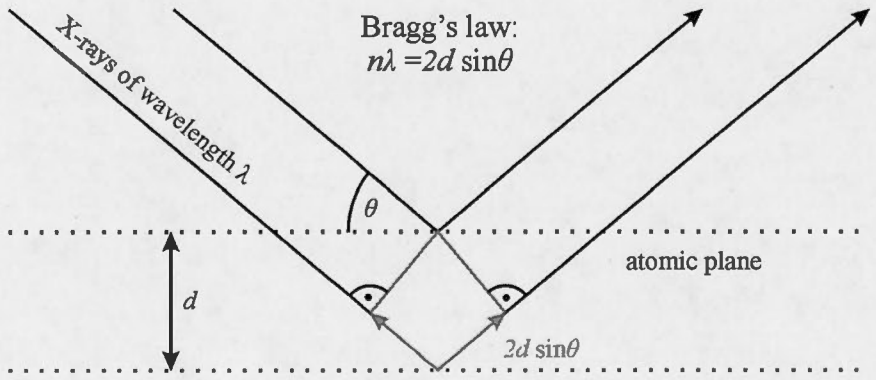

Figure 0.8 Illustration of X-ray diffraction at atomic planes according to Bragg's law.

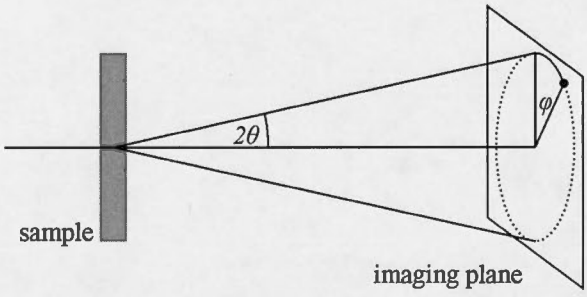

Figure 0.9 Difference between diffraction angle and imaging plane angle

Depending on the solid's symmetry, some planes may be oriented differently but exhibit the same lattice distance, *i.e.* are symmetry equivalent. Different from single crystal diffraction, in powder diffraction, these do not form separate diffraction peaks, but all contribute to one reflex. The number of measured peaks is thus dependent on the symmetry, whereas solids with high symmetry (many symmetry operations possible in the periodic unit) exhibit less diffraction spots than solids with low symmetry.

Diffracting planes are commonly identified by their Miller's indices. These describe a normal vector in reciprocal space, identifying an atomic plane. As such, a plane that intersects with the lattice axes at $a = a_1$, $b = b_1$ and $c = c_1$ will have the Miller's indices $h = 1/a_1$, $k = 1/b_1$ and $l = 1/c_1$. Given the Miller's indices and diffraction angles of different diffraction spots, it is possible to obtain the lattice constants and angles for a specified crystal system, using Bragg's law, and the equations given in Table 0.1.

The diffraction intensity depends on how strongly X-rays interact with the diffracting atoms. Since X-rays interact mainly with electrons, elements that have low electron density around the core (*e.g.* H^+ or Li^+ ions) diffract very little, whereas heavier elements diffract much stronger. Diffraction intensity also depends on the lattice spacing, the X-ray wavelength, the X-ray polarization and other factors and

can be determined mathematically.(Waseda, et al., 2011) These dependencies will be quickly introduced below.

The intensity of a diffraction reflex is described by the general equation

$$I_{h,k,l} \sim |F_{h,k,l}|^2 \cdot m \cdot f_P \cdot f_L \cdot f_A \cdot f_T \ , \quad (0.12)$$

Where F is the structure factor, and depends on the structure and the atom type. m is the multiplicity of a reflex, *i.e.* how many symmetry equivalent lattice planes contribute to the reflex, f_P represents a polarization factor, f_L the Lorentz factor, f_A the absorption factor and f_T the temperature factor. X-ray polarization, which arises in laboratory X-ray tubes from the monochromator and is native to synchrotron X-rays, leads to a modulation of the diffraction intensity with diffraction angle. This factor thus depends on the X-ray source and/or the instrumental geometry, *i.e.* the location of the monochromator. The Lorentz factor arises from the circumstance that different amounts of sample are probed depending on the diffraction angle. The absorption factor is only relevant for very thin samples, as it reduces otherwise to a constant value and does not change relative intensities. The temperature factor is a sign of atomic vibrations, which reduce the efficiency of the diffraction from the periodic lattice.

Most important to structure refinement is arguably the structure factor, as it incorporates most structural information, *e.g.* fractional coordinates, atom type, site occupancy etc. It takes on the general form

$$F_{h,k,l} = \sum_{j=1}^{n} f_j e^{2\pi i\left(\frac{hx_j}{a}+\frac{ky_j}{b}+\frac{lz_j}{c}\right)} \ , \quad (0.13)$$

Where the summation is over all atoms j in the unit cell, f_j is the atomic scattering factor, h, k and l are Miller's indices for the corresponding reflex, x_j, y_j and z_j are the coordinates of atom j, and a, b and c are the lattice parameters. The atomic scattering

factor takes into account the number of electrons per atom, as well as their approximate distribution. It can also incorporate a correction for the electron delocalization due to thermal motion, and the occupancy of any given site.

Table 0.1 Relation between lattice spacing, Miller's indices and lattice constants for the seven crystal systems

Cubic	$\frac{1}{d^2} = \frac{h^2 + k^2 + l^2}{a^2}$
Tetragonal	$\frac{1}{d^2} = \frac{h^2 + k^2}{a^2} + \frac{l^2}{c^2}$
Hexagonal	$\frac{1}{d^2} = \frac{4}{3}\left(\frac{h^2 + hk + k^2}{a^2}\right) + \frac{l^2}{c^2}$
Trigonal	$\frac{1}{d^2} = \frac{(h^2 + k^2 + l^2)\sin^2\alpha + 2(hk + kl + hl)(\cos^2\alpha - \cos\alpha)}{a^2(1 - 3\cos^2\alpha + 2\cos^3\alpha)}$
Orthorhombic	$\frac{1}{d^2} = \frac{h^2}{a^2} + \frac{k^2}{b^2} + \frac{l^2}{c^2}$
Monoclinic	$\frac{1}{d^2} = \frac{1}{\sin^2\beta}\left(\frac{h^2}{a^2} + \frac{k^2\sin^2\beta}{b^2} + \frac{l^2}{c^2} - \frac{2hl\cos\beta}{ac}\right)$
Triclinic	$\frac{1}{d^2} = \frac{1}{V^2}(S_{11}h^2 + S_{22}k^2 + S_{33}l^2 + 2S_{12}hk + 2S_{13}hl + 2S_{23}kl)$ With, $S_{11} = b^2c^2\sin^2\alpha$ $S_{22} = a^2c^2\sin^2\beta$ $S_{33} = a^2b^2\sin^2\gamma$ $S_{12} = abc^2(\cos\alpha\cos\beta - \cos\gamma)$ $S_{12} = bca^2(\cos\beta\cos\gamma - \cos\alpha)$ $S_{12} = acb^2(\cos\alpha\cos\gamma - \cos\beta)$

0.3.5.2 Peak shapes

The previous equations are used to obtain location and intensity of diffraction reflexes. However, such reflexes are not ideally sharp, leading to a peak shape and width for each reflex. This is the result of finite crystal domain sizes, structural disorder and thermal motion. The most commonly used peak shapes in crystallography are Gaussian curves,

$$I_G = I_{max} e^{-\frac{4\ln 2(2\theta - 2\theta_0)^2}{W^2}}, \quad (0.14)$$

Lorentzian curves,

$$I_L = I_{max} \frac{\left(W/2\right)^2}{\left(W/2\right)^2 + (2\theta - 2\theta_0)^2}, \quad (0.15)$$

And, combining the two, Pseudo-Voigt curves,

$$I_{PV} = \eta_L \cdot I_L + (1 - \eta_L) \cdot I_G \,. \quad (0.16)$$

Gaussian curves exhibit the same shape as a Normal distribution. At the same width, they distribute more intensity near the maximum and fall quicker to the background, than Lorentzian curves. In most cases, an intermediate curve shape between Gaussian and Lorentzian functions fits the experimental data best. As such, the Pseudo-Voigt function combines the two in a linear combination with the Lorentz fraction η_L.

The peak shape, but more importantly its width, can provide important information on the microstructure of the sample.(Waseda, et al., 2011) As such, a universal measure of the peak width is needed. Most widely applied is the Full Width at Half Maximum, denoted W in the equations above, which is the diffraction angle difference between the two points of the curve that exhibit half the intensity of the peak maximum. A more stringent measure with respect to the width of the

distribution of the peak, *i.e.* one that is independent of peak shape, is the integral breadth W_I. This is the angle difference between the two integration limits, equidistant to the peak maximum, of the curve integral that is half the total peak integral.

The peak width mainly depends on the coherently scattering domain size and the distribution of lattice parameters. This former can be deduced from the geometrical considerations of Figure 0.8. This figure shows the phase shift of two scattered X-ray beams from two lattices. The criterion for constructive interference, *i.e.* the phase shift is a multiple of the wavelength, leads to Bragg's law. Completely destructive interference occurs if the phase shift is exactly half the wavelength, *i.e.* $2d \sin\theta = n\lambda 2$. At this diffraction angle, there is no diffracted beam intensity. Let's consider an X-ray beam scattered at two lattices at an intermediate diffraction angle that leads to $2d \sin\theta = n\,\lambda/4$. The intensity of the resulting X-ray beam is $(\sin\pi/2 + \sin\pi)/2 = 0.5$, so half the intensity of the constructive interference. This is still a significant intensity, even though the diffraction angle is quite different. With an increasing number of wave functions interfering, *i.e.* an increasing number of contributing lattices, the intensity and the sharpness of the constructive interference peak increases. This behavior is illustrated in Figure 0.10.

The origin of peak width due to micro-strain, which is commonly quantified by Stoke's equation, can be understood more intuitively. The derivation of Stoke's equation is based on a distribution of lattice parameters with finite width. As such, diffraction conditions, and the diffraction angle change over the sample. This is reflected in the width of the diffraction peak.

Relationships exist, that quantitatively describe the effect of crystal domain size and micro-strain on peak width. For this purpose, the peak width must first be corrected for an instrumental broadening, *i.e.* the intrinsic peak width of the instrument. This can be determined with a highly crystalline large crystallite standard

sample. After width correction for instrumental effects, Scherrer's equation is frequently used to determine crystallite size L from the remaining sample-contributed peak width:(Jones, 1938)

$$L = \frac{\lambda}{W_{I,size} \cos\theta} \quad . \quad (0.17)$$

The micro-strain S, instead, is obtained from Stokes' equation:(Stokes & Wilson, 1944)

$$S = \frac{\tan\theta}{2W_{I,strain}} \quad . \quad (0.18)$$

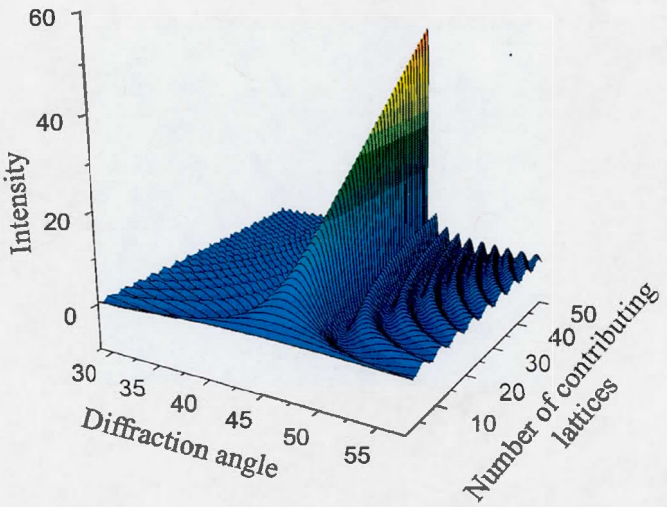

Figure 0.10 Diffraction peak development with the number of diffracting lattices, *i.e.* the number of interfering scattered X-ray beams

Since micro-strain and crystal domain size affect peak width with different diffraction angle dependence, it is possible to distinguish between the two, when the diffractogram is recorded in a large diffraction angle range. Hall's method combines both equations linearly, plotting $W_I \cos\theta$ *vs.* $\sin\theta$:(Williamson & Hall, 1953)

$$W_I \cos\theta = \frac{\lambda}{L} + 2S \sin\theta \quad . \quad (0.19)$$

From linear regression, one then obtains $2S$ from the slope and λ/L from the intercept with the abscissa. Since both, crystal domain size and micro-strain, may be dependent on the crystallographic direction, *i.e.* be anisotropic, Hall's method might only yield linear relationships for reflexes of the same group of planes.

0.3.5.3 Rietveld refinement and other data treatments

Given the extensive theory behind X-ray diffraction, it is possible to estimate a diffractogram from a given structure. This requires guessing the crystal structure, peak width and shape, the background signal, and the properties of the X-ray source. Estimates of intensity, location and peak shape of diffraction reflexes have been described above. Furthermore, gas phase scattering, inelastic scattering in the sample and electronic noise lead to a signal background. Different mathematical functions can be used to fit the background, most commonly polynomials or quadratic splines. Many more theoretical relationships exist to account for other crystallographic information, *e.g.* strain, size and temperature factor anisotropy and quantitative phase analysis.

With an initial theoretical diffractogram in hand, parameters are varied to match the theoretical diffractogram to experimental data by Rietveld refinement.(Rodriguez-Carvajal, 2001) This process employs a least squares method to reduce a variance weighted difference between theoretical and experimental data. The variances are estimated from the counts, at which commonly a Gaussian distribution is assumed.

The improvement of the fit is best observed in overlaying experimental and theoretical diffractogram, as well as plotting the residual. However, in many cases, the quality of the fit can be estimated from agreement factors. These are the weighted profile factor

$$R_{wp} = 100 \sqrt{\frac{\sum_{i=1}^{n} w_i \left(I_{t,i} - I_{e,i}\right)^2}{\sum_{i=1}^{n} w_i y_i^2}} , \quad (0.20)$$

Which is viewed relative to the expected weighted profile factor

$$R_{exp} = 100 \sqrt{\frac{N - P}{\sum_{i=1}^{n} w_i y_i^2}} . \quad (0.21)$$

w_i is the weight factor, the summations extend over all points i of the diffractogram, I_t are the calculated and I_e the experimental diffractogram intensities at the same diffraction angle, N is the total number of recorded points and P is the number of varied parameters. The Goodness of Fit GoF is given as the ratio between the two profile factors

$$GoF = \frac{R_{wp}}{R_{exp}} , \quad (0.22)$$

and indicates a good fit as it approaches one. Values below one indicate a non-significant fit, *i.e.* too many parameters are fitted for the amount of data available.

This method is widely used to determine structure parameters for new structures, and to confirm already reported structures. As such, the report by Padhi *et al.* on the use of *olivine* electrode materials in general, and $LiFePO_4$ specifically, in lithium batteries also published the respective Rietveld refined structures.(Padhi, et al., 1997)

0.3.5.4 Synchrotron X-ray sources

For some X-ray diffraction studies of dynamic processes, conventional X-ray equipment is too slow in collecting high quality diffractograms. In order to decrease collection time, it is necessary to either improve detector technology to be more sensitive, or to increase X-ray intensity. As such, many *in situ* diffraction studies are performed with the most intense man-made X-ray radiation: synchrotron radiation.

Synchrotrons are particle accelerators, in which electrons are accelerated close to light speed, and then maintained at that speed.(Wiedemann, 1998) While the electrons move at high speed, controlled and synchronized magnetic fields keep them on a defined track. Similar to the process in a radio antenna, electrons release electromagnetic radiation as they are deflected, but due to their high speed in a synchrotron, the radiation energy is much higher. Instead of radiofrequency radiation, X-ray radiation is released. Furthermore, at such high speed, relativistic effects lead to a bundling and linear ejection of these X-rays in the laboratory observation frame, comparable to a light beam. These X-rays are many orders of magnitude more intense then laboratory X-ray sources.

A synchrotron essentially consists of a cathode electron gun, in principle similar to the electron source in tube TVs or electron microscopes, which injects electrons into the linear electron accelerator (Linac).(APS/ANL, 2013) There, radio frequency electro-magnetic fields accelerate the electrons to several MeV, from which they are in turn injected to the booster ring, which again accelerates the electrons by several orders of magnitude, to the GeV range. In order to focus the electron beam and keep it on the ultra-high vacuum track, magnetic fields are necessary. These also define the trajectory of the electrons in the storage ring, where they are not accelerated anymore, but maintained at the same speed and focus.

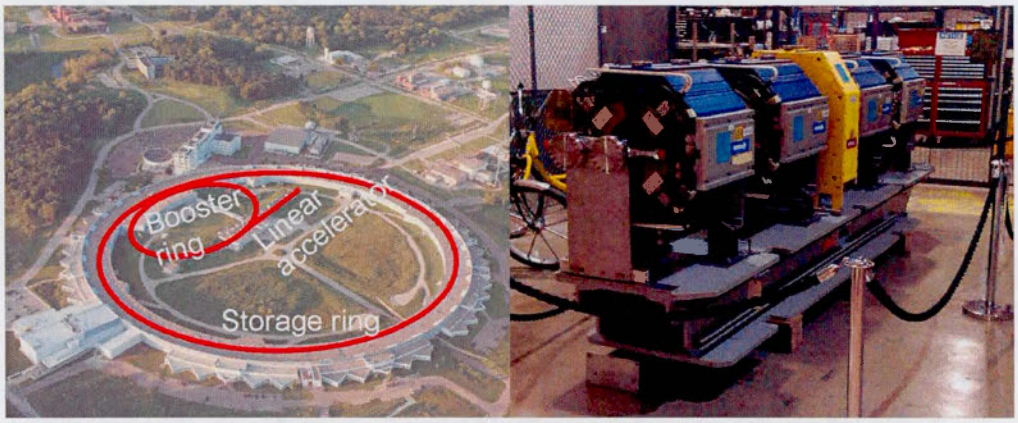

Figure 0.11 The Advanced Photon Source (APS, photograph courtesy of the APS, Argonne National Laboratory, operated for the Department of Energy), and decommissioned quadrupole magnets, used to focus the electron beam.

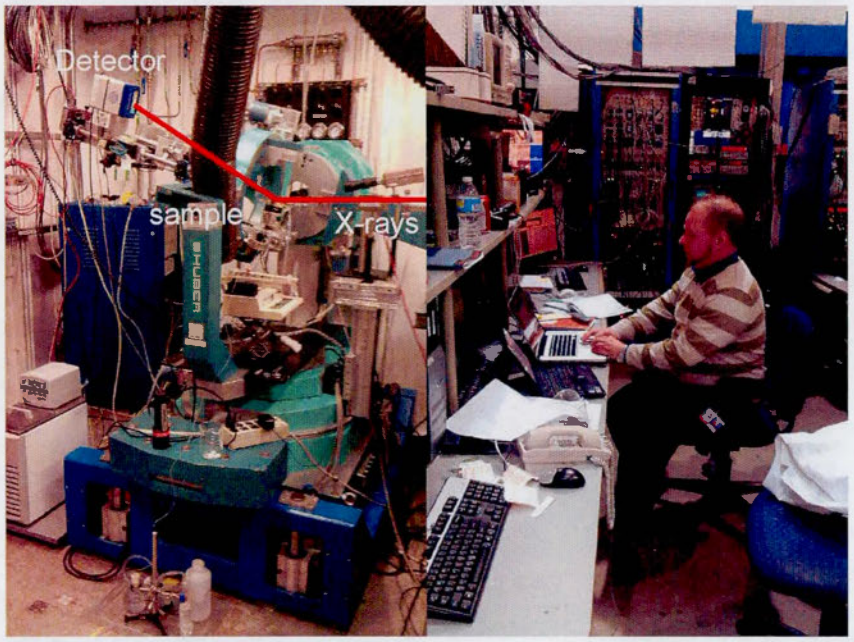

Figure 0.12 Beamline 7-ID, hutch C during *in situ* diffraction experiments described in Chapter (left) and the beamline control station (right).

While the purpose of the Linac and the booster ring is to accelerate electrons, the storage ring serves to produce X-rays. This occurs when electrons are deflected in magnetic fields. Each charged particle has an electric field, which changes upon acceleration of the particle, and spreads as an electromagnetic wave. In a synchrotron, relativistic electrons, *i.e.* electrons that move close to the speed of light, produce such electromagnetic waves, but from the observer's point of view, these are not spreading uniformly in all directions, as from a radio antenna, but are collimated forward. Furthermore, the Doppler Effect modifies the observed wavelength in the laboratory frame. The emitted radiation is strongly polarized, and its characteristics depend on the speed of the electrons and the direction and strength of the force acting on the electrons.(Kim, 2009)

The magnets that define the electron trajectory can be bending magnets, that maintain the overall circular track of the electrons in the storage ring, or insertion devices, that return the electrons back onto a linear path. Insertion devices can be undulators or wigglers, which generally consist of a series of alternating magnetic fields. As such, the electron beam undulates around its linear track. At each magnet, synchrotron radiation is emitted. Insertion devices are optimized, as to obtain constructive interference between such synchrotron beams, to increase the overall brilliance of the emitted beam. Bending magnets produce synchrotron radiation as well, which is less brilliant, but polychromatic. With the help of these magnets the overall electron track describes a circle, which may be quite large. For example the storage ring of the Advanced Photon Source (APS), which delivers the highest intensity X-rays in the western hemisphere, has a circumference of more than one kilometer.

At each insertion device and at each bending magnet, X-rays are harvested in beamlines to perform experiments. Each beamline is specialized for specific techniques, and for which the produced X-rays can be optimally used. Two common

techniques, present in such beamlines, have already been introduced: X-ray microscopy and X-ray diffraction.

Synchrotron X-ray absorption spectroscopy and X-ray diffraction have both been used to study $LiFePO_4$ kinetics *in situ* and *in operando*.(Orikasa, Maeda, Koyama, Minato, et al., 2013; Orikasa, Maeda, et al., 2013a, 2013b; X. Yu, et al., 2012) The high intensity synchrotron radiation in connection with fast X-ray detectors can record fast changes inside battery materials, thus giving insight into the dynamic properties of such materials under high load.

0.4 Challenge

The previous sections have shown that diffusion phenomena are of fundamental importance to the charging speed of lithium batteries. To improve charging rates, it is thus crucial to have a deep understanding of these lithium transport processes.

The aim of this thesis is to address knowledge gaps related to lithium mobility in the electrode material $LiFePO_4$. Atomistic models, *in situ* tracking of the progress of charging and discharging reactions, and *in situ* crystallographic observation of the phase change during ultrafast charging have been used to shine light onto some transport features that have not yet been fully understood. The focus lies on the fast rate mechanisms.

In particular the chapters address the following questions:

Chapter I.	What is the limiting reduction/discharging rate of $LiFePO_4$?
Chapter II.	What is the limiting oxidation/charging rate of $LiFePO_4$?
Chapter III.	At ultrafast rate, transforms $LiFePO_4$ to $FePO_4$ in two phases or in one?
Chapter IV.	What is the influence of site exchange defects on the performance of $LiFePO_4$?

The first chapter reports on the use of *in situ* photometry to follow the chemical reduction of $FePO_4$ to $LiFePO_4$ with LiI. This chemical approach to study the intrinsic lithium transport kinetics in $LiFePO_4$ eliminates the problems of solvent ionic conductivity, tortuous electron and lithium transport and electronic conductivity/connectivity inherent to electrochemical techniques. The resulting reaction rate shows that lithium transport inside $LiFePO_4$ is not rate limiting in current lithium battery technology.

A similar approach was used in the second chapter to study the limiting charging rate of $LiFePO_4$. Here, the oxidant was not dissolved in a liquid, but was a gas. X-ray diffraction was applied *in situ*, however, the achieved 10 s time resolution of this technique was still too slow to obtain well resolved data of the phase transition from $LiFePO_4$ to $FePO_4$. Nevertheless, the data clearly shows a very fast complete charge of $LiFePO_4$ in less than one minute.

Time resolution of *in situ* X-ray diffraction was drastically improved in Chapter III, which applied a synchrotron X-ray source to the problem. At an acquisition frequency of 10 Hz, diffractograms of high quality show the detailed crystallographic changes in $LiFePO_4$ during this phase transition. Asymmetric peak broadening shows quantifiable anisotropic asymmetric strains, which likely originate from a wide interface between the $LiFePO_4$ and the $FePO_4$ phase. Comparing the strain along the different crystallographic directions, the interface aligns perpendicular to the crystallographic *a*-axis. Most significantly, however, the data shows that phase separation into a lithium rich and a lithium poor phase in $LiFePO_4$ during charging persists even at ultrafast delithiation rate.

While the first three chapters are concerned with the lithium mobility on the particle scale, the fourth chapter looks at lithium mobility at the atomic scale. After introducing a new set of potential parameters of the $LiFePO_4/FePO_4$ system, empirical atomistic modeling shows that iron antisite defects may not impede lithium

diffusion significantly. Instead, such defects may be removed after the first few charge/discharge cycles.

Finally, the fifth chapter summarizes all findings and proposes recommendations towards improving $LiFePO_4$ type materials. It also summarizes the characteristics that seem to make $LiFePO_4$ a high rate lithium battery material, with the goal to provide new information to future development of high power and energy density electrode materials.

CHAPTER I

KINETICS OF HETEROSITE IRON PHOSPHATE LITHIATION BY CHEMICAL REDUCTION

To understand the interior dynamics of a material, it is important to know its kinetic reaction behavior. For battery materials, this is particularly difficult, as normally one measures these kinetics electrochemically, in a very complex environment. In most cases, assumptions are made, that this environment's impact on the kinetics can be neglected, but these assumptions are challenging to confirm. Less problematic are chemical reactions, which require only determination of temperature, possibly pressure, and control of the concentration of reaction species. The first three chapters of this dissertation make use of this simplification. The present chapter uses LiI as reducer of $FePO_4$ to mimic its discharging behavior, and follows the reaction by determining formation of I_2 *in situ*.

This chapter has been accepted for publication in Journal of Physical Chemistry C. Christian Kuss, Murielle Carmant-Dérival, Ngoc Duc Trinh, Guoxian Liang and Steen Brian Schougaard are co-authors of this article. The Supporting Information for this article can be found in Appendix A.

The contributions of all authors are as follows:

- Christian Kuss: Design of experiment, kinetic experiments, figures, data analysis, discussion, redaction of manuscript;

- Murielle Carmant-Derival: Preliminary kinetic experiments, product characterizations;
- Ngoc Duc Trinh: Electrochemical tests incl. data treatment;
- Guoxian Liang: Discussion, Preparation of $LiFePO_4$ materials;
- Steen Schougaard: Supervision, redaction of manuscript.

1.1 Abstract

Understanding the kinetics of the charging and discharging processes in battery materials is important to improving high power performance. As such, we here investigate the kinetics of $LiFePO_4$ relithiation by reduction with lithium iodide. Unlike standard electrochemical kinetic analysis, which yields a convoluted response of all the components of the composite electrode, this approach probes only the kinetics of the electroactive material particles. The kinetic data was compared to the Avrami solid state reaction model, and a statistical model by Bai and Tian.(Peng Bai & Tian, 2013) Different from chemical delithiation, the lithiation reaction does not fit a solid solution one-dimensional diffusion model, rather it follows the Avrami equation (Avrami exponent 0.6) with an activation energy of 50 kJ mol^{-1}. The obtained reaction rate information is central to the development of physically accurate quantitative battery models.

1.2 Introduction

In 2006, the introduction of the Tesla Roadster brought prestige to electrified personal transport,(Voelcker, 2006) leaving other car manufacturers to pick up the pace in the development of mass market electric cars. Since then most major car manufacturers have introduced an electric or hybrid electric car in their portfolio. Unfortunately, mainstream consumers remain unsatisfied, particularly with respect to driving range and charging time.(Graham-Rowe et al., 2012) Consequently, research towards improving lithium battery rate performance continues.

To identify the rate limiting step in composite battery electrodes, complex physical models are often employed.(Cornut, Lepage, & Schougaard, 2012; Thorat, Joshi, Zaghib, Harb, & Wheeler, 2011) Due to the complexity of ion transport in batteries – through active materials, auxiliary materials and tortuous paths in the liquid electrolyte – a large number of parameters are needed. Of these, only few have been acquired experimentally, while most are derived from fitting modeled data to

experimental ones. Models that are based on processes that are physically very different may therefore yield comparable reproducibility of experimental results, simply due to the number of adjustable variables available during the nonlinear fitting process. The situation is further complicated by the fact that some experimental parameters are reported with great variability. This is the case for the lithium diffusion coefficient of $LiFePO_4$.

$LiFePO_4$ has been extensively researched over the past fifteen years as a positive lithium battery material, as it exhibits very advantageous properties.(Padhi, et al., 1997) Nevertheless, its *reported* lithium diffusion coefficients span an unusually large range from 10^{-18} cm^2 s^{-1} to 10^{-12} cm^2 s^{-1}.(Park, et al., 2010) Importantly, recent research has shown that apparently slow lithium mobility in $LiFePO_4$ may be an artefact of the lithium movement in the complex composite electrodes. Thus the apparent $LiFePO_4$ kinetics are faster if the material is investigated separately from the conventional electrode coating.(Huang, et al., 2012; Kuss, Lepage, Liang, & Schougaard, 2013; Lepage, Sobh, Kuss, Liang, & Schougaard, 2014) *E.g.* in a recent electrochemical single particle study $LiFePO_4$ was charged to 70% of its slow rate capacity in two minutes.(Huang, et al., 2012) Thus, to get reliable diffusion coefficients while avoiding the kinetic limitations imposed by the composite electrode, we recently used chemical oxidation, to study $LiFePO_4$ delithiation kinetics.(Kuss, et al., 2013; Lepage, et al., 2014) In the present paper, we are expanding on these results, by investigating the relithiation kinetics by an *in situ* method. To this end, we used a chemical reducing agent to insert lithium into $FePO_4$, thus avoiding the need to connect the particles electronically to a current collector. As such, neither binder, nor conductive matrix are needed. Instead, electrons and lithium ions are drawn from the surrounding solution. Due to stirring, the diffusion path around each particle is kept short, ensuring quick concentration equilibration. Consequently, the thermodynamic driving force for the relithiation reaction is well distributed over the entire particle population, as well as, the surface of each

individual particle. Overall the methodology employed here is therefore similar to the familiar electrochemical potential step, except, electrons are delivered *via* the molecular redox reaction at the surface of the particle rather than from the current collector through the composite electrode structure. As such, the effects of non-uniform electronic potential and lithium concentration, which complicate analysis of the electrochemical potential step experiments(Malik, Abdellahi, & Ceder, 2013) are minimized or eliminated here. Finally, the progress of the relithiation reaction(Prosini et al., 2002)

$$FePO_4 + LiI \rightarrow LiFePO_4 + \tfrac{1}{2} I_2 \qquad (1)$$

can be conveniently followed photometrically *in situ* due to formation of the strongly colored iodine molecules.

1.3 Experimental

Industrial hydrothermally synthesized carbon coated $LiFePO_4$ was employed as starting material. The $LiFePO_4$ was exposed to a solution of 2.4 % hydrogen peroxide and 0.1 % acetic acid in water to delithiate the material to $FePO_4$.(Lepage, et al., 2014) Complete relithiation was achieved by suspending the produced $FePO_4$ in a 14 mM solution of LiI in Acetonitrile, allowing for more than 60 minutes reaction time. The product was subsequently filtered, washed with Acetonitrile and dried.

Starting material, $FePO_4$ and relithiated $LiFePO_4$ were subjected to attenuated total reflectance fourrier transform spectroscopy (ATR-FTIR), X-ray diffraction (XRD) and transmission electron microscopy (TEM). ATR-FTIR was performed on a Thermo Scientific Nicolet 6700 FTIR spectrometer using a Smart iTR diamond crystal accessory in the wavenumber range of 600 cm^{-1} to 2000 cm^{-1}. X-ray diffraction (XRD) was performed with a Co-Kα source (λ = 1.789 Å), to avoid interference from iron X-ray fluorescence. Transmission electron micrographs (TEM) were recorded on a JOEL JEM-2100F with an acceleration voltage of 200 kV, after

suspending the samples in acetonitrile and depositing them on a lacey carbon / nickel grid. The lithium insertion yield was determined by atomic emission/absorption spectroscopy. To this end, the produced material was dissolved in concentrated nitric acid (Anachemia ACS), and diluted. Spectroscopy standard solutions (Li: Alfa Aesar, Fe: Fisher Scientific) were diluted to the same concentration range as the sample, using dilute nitric acid, to obtain a calibration curve. Concentrations were determined by flame atomic emission spectroscopy at 670.8 nm for lithium and by flame atomic absorption spectroscopy at 248.3 nm for iron. Elemental analysis was performed in triplicates. The error is estimated based on a student's t distribution for a confidence level of 95%.

The electrochemical performance was determined with CR2032-type coin cells using metallic lithium (Alfa Aesar 99.9 %) as the anode. The positive electrode was prepared by casting a slurry of 84.2 wt.% $LiFePO_4$, 8.8 wt.% acetylene black and 7 wt.% polyvinylidene fluoride (Kynar KF Polymer W#1100) in N-methyl-2-pyrrolidone (Alfa Aesar 99.5%) on carbon-coated Al current collector (Exopack). The coating was subsequently dried at 60 °C under atmospheric pressure for 2 hours, and under reduced pressure overnight. The dried electrode exhibited a thickness of 40 μm and a density of 0.36 g cm^{-3}. A 1 M $LiPF_6$ in 1:1 ethylene carbonate / dimethyl carbonate (Novalyte Technologies) electrolyte and Celgard 2500 separator were used. The coin cells were assembled in an argon atmosphere glove box (H_2O < 1 ppm, O_2 < 1 ppm). Electrochemical testing was performed by galvanostatic cycling at a C/5 rate with a cell voltage range of 2.2-4.2 V at room temperature using a BST8-MA 8 channels battery analyzer (MTI corp.). An open circuit rest period of 60 minutes was imposed after every charge/discharge step. The plotted capacity was calculated with respect to the amount of carbon coated $LiFePO_4$ employed in the positive electrode.

In situ photometry of the described relithiation reaction was performed at 361 nm in a standard UV/Vis spectrometer (Ocean Optics) with a 1 cm light path standard

quartz cuvette. Lithiation experiments were performed in a 13.4 mM solution of LiI in acetonitrile. The initial light absorption of 1.8 ml of the LiI solution was recorded for about 10 seconds. Then 0.2 ml of a 0.042 mM $FePO_4$ suspension was added and the absorption vs. time was collected for an additional 10 min. The cuvette was kept closed to avoid significant solvent evaporation. Stirring was maintained during data collection. The experiment was performed in a cuvette holder that allows temperature control. All solutions were thermalized in a waterbath before experimentation. The temperature was confirmed using an infrared thermometer (Mastercraft). To obtain calibration curves, the same concentration of LiI solution was treated with varied known amounts of $FePO_4$ and left to react for one hour, before filtering and measuring their absorption. This ensures that absorption changes due to formation of oligo-/poly-iodide ions are considered. To account for parasitic iodide oxidation by air, as well as, particle scattering, blanks were recorded using the same procedure as for the *in situ* runs, but adding $LiFePO_4$ instead of $FePO_4$.

Finally, to test the hypothesis that diffusion in the liquid and surface oxidation reaction kinetics are not limiting the reaction rate, the same photometric experiment was carried out at room temperature with a LiI solution diluted to ¼ of the previous concentration. No effect of the dilution on the reaction rate could be observed.

1.4 Results and discussion

1.4.1 Validation of the relithiation products

Carbon coated $FePO_4$, obtained by delithiating commercial $LiFePO_4$, using a solution of H_2O_2 in water, was relithiated according to equation (1). The resulting materials were submitted to different characterization techniques, in order to confirm the nature of the reaction products. XRD(Rousse, Rodriguez-Carvajal, Patoux, & Masquelier, 2003), as well as, ATR-FTIR(Burba & Frech, 2004) spectroscopy show the formation of *heterosite* $FePO_4$ after oxidation with hydrogen peroxide.

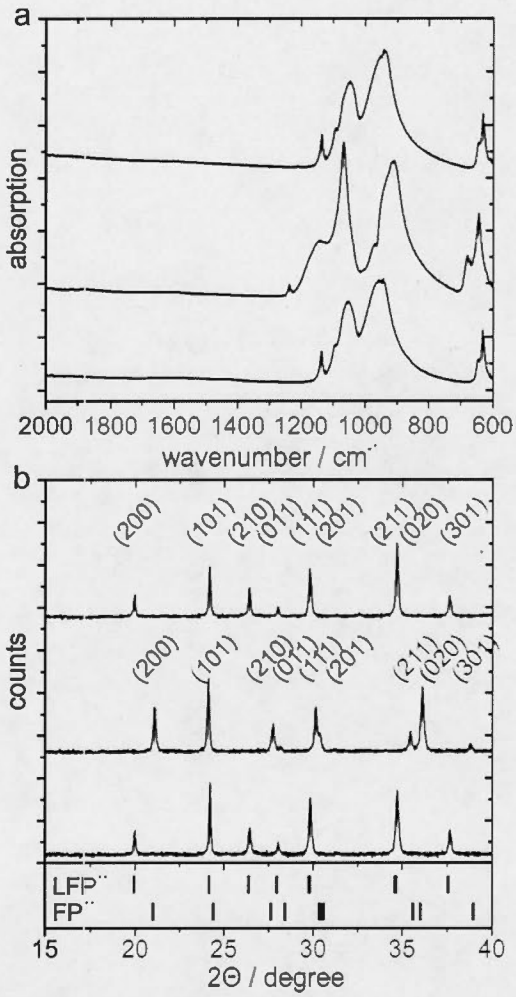

Figure 1.1 Characterization of reaction products. ATR-FTIR (phosphate stretching modes above 800 cm^{-1} and phosphate bending modes between 600 and 700 cm^{-1})(Burba & Frech, 2004) spectra (a) and X-ray diffractograms(Rousse, et al., 2003) (b) of initial $LiFePO_4$ (top), H_2O_2 delithiated $FePO_4$ (middle) and LiI relithiated $LiFePO_4$ (bottom). The effect of H_2O_2 oxidation is completely reversed by exposure to LiI.

After relithiation, the produced $LiFePO_4$ is indistinguishable from the starting material by ATR-FTIR spectroscopy (figure 1.1a) and XRD (figure 1.1b). Furthermore, atomic emission spectrometry confirms a lithium to iron ratio of 1.1 ±

0.1 in the relithiated product. Consequently, all three techniques confirm that this reaction is chemically analogue to the electrochemical discharge of lithium iron phosphate.

Dissolution and redeposition effects may change the product crystallinity or morphology under chemical reduction conditions, which might not appear in XRD or ATR-FTIR data. Transmission electron microscopy (TEM) of the initial sample (figure 1.2 a, c) and the relithiation product (figure 1.2 b, d) was therefore undertaken. Similar to XRD and ATR-FTIR results, no change in the material is observable, thus supporting the hypothesis, that the lithiation reaction with LiI can be used as a model for lithium iron phosphate discharge.

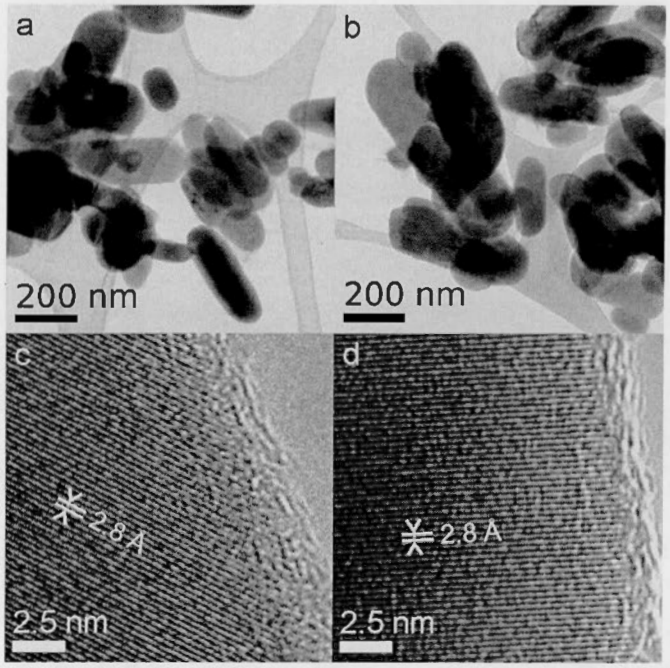

Figure 1.2 Morphology and crystallinity. TEM micrographs of the initial $LiFePO_4$ (a and c) and the relithiated $LiFePO_4$ (b and d) at standard and high resolution (2.8 Å lattice distance is consistent with the $LiFePO_4$ (3,0,1) lattice plane).

Particle morphology and crystallinity remain intact after the complete chemical lithiation cycle.

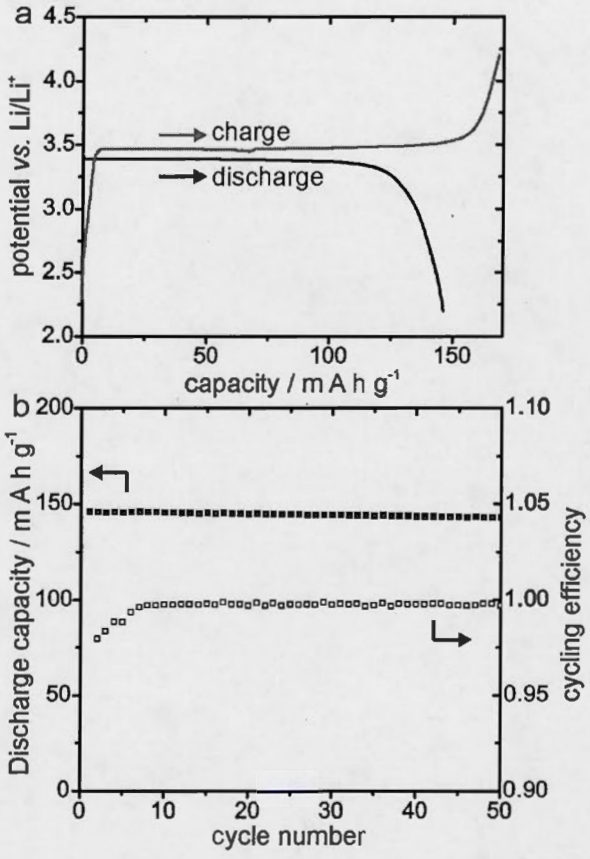

Figure 1.3 Electrochemical performance of the chemically cycled $LiFePO_4$. a. First charge / discharge cycle of a battery containing the relithiated $LiFePO_4$. b. Cycling efficiency and cycling stability of the same battery.

Finally, in order to confirm that the material remains electrochemically active, the product $LiFePO_4$ was electrochemically cycled in research coin cells. As can be seen in figure 1.3 a and b, the electrochemical cell discharges and charges with stable potential plateaus around 3.4 V *vs.* Li/Li^+. The obtained capacity remains stable over the 50 recorded test cycles.

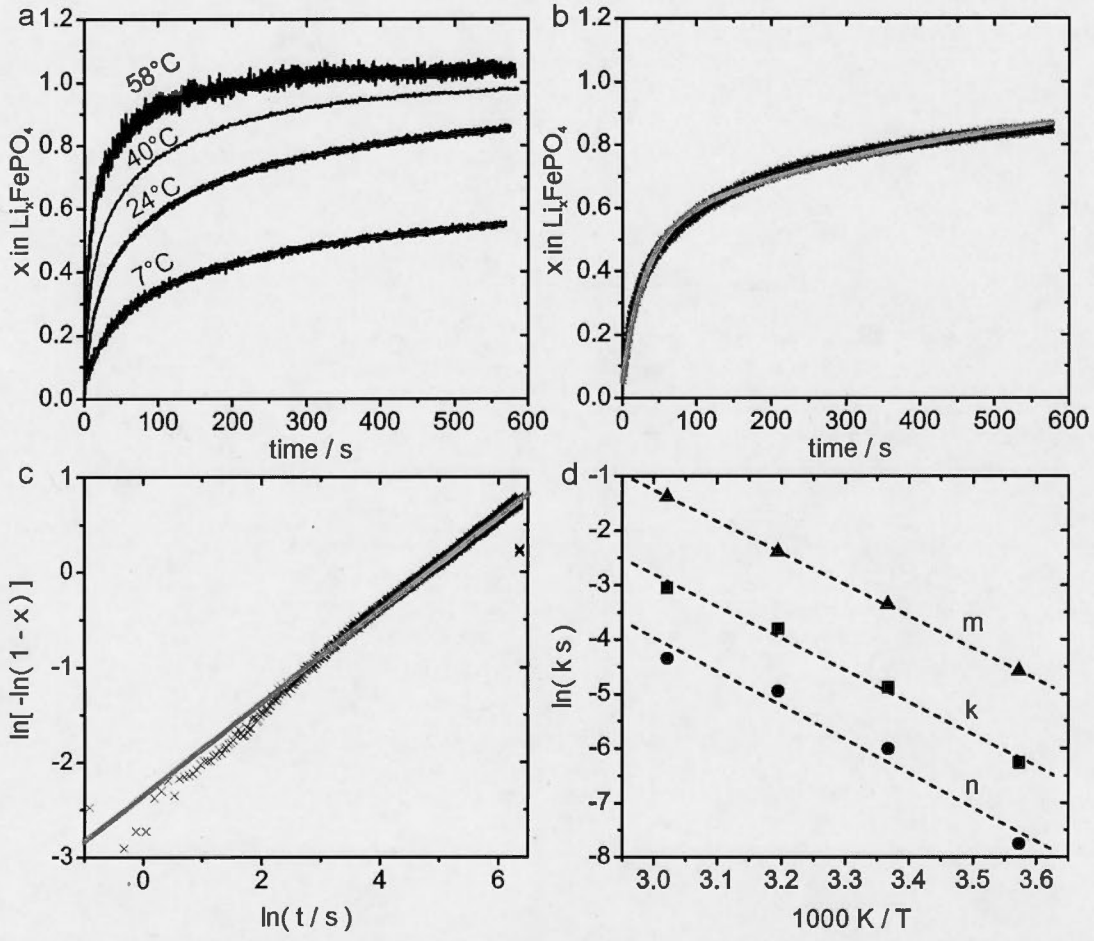

Figure 1.4 *In situ* photometry data. Lithiation curves of Li_xFePO_4 (a), fit to the Bai model (black: experimental data, grey: model) (b), fit to the Avrami model (black: experimental data, grey: model) (c), and Arrhenius plot (d) of the obtained kinetic data. *m* corresponds to the rate of active particle to transformed particle conversion and *n* to the particle activation rate of the Bai model. *k* corresponds to the reaction rate of the Avrami model. Respective equations can be found in the supporting information. The room temperature reaction has been shown to reach x = 1.1 ± 0.1 at prolonged reaction time by elemental analysis.

1.4.2 *In situ* UV/Vis photometry

UV/Vis spectroscopy was used to follow the reaction *in situ*, subsequent to the confirmation the reaction product as being crystalline and electrochemically active $LiFePO_4$, The formation of iodine leads to a strong increase in light absorption in the visible spectrum. Figure 1.4a therefore shows well-resolved photometric data with a high.

To quantify the reaction rate, classic solid state kinetic models(Khawam & Flanagan, 2006) may be chosen, *e.g.* the Avrami model has been applied previously to study $LiFePO_4$,(Allen, Jow, & Wolfenstine, 2007, 2012; Lepage, et al., 2014). Alternatively, a statistical model has been developed by Bai and Tian(Peng Bai & Tian, 2013; Levi et al., 2013) for the transformation of $LiFePO_4$ particles in an electrode. Based on a statistical understanding of the reaction progress, the Avrami and Bai models lead to mathematically similar expressions for the reaction progress. In fact, all the following models are of the same mathematical form $-\ln(1-\alpha) = kt$ (α conversion fraction, k reaction rate constant, t time):

i. Bai model under the condition that the transformation rate of "activated" particles is very fast, compared to the "activation" rate (*e.g.* nucleation rate),

ii. Bai model under the condition that all particles are already activated and reaction progress is only determined by the transformation rate,

iii. Avrami model for a transformation that is solely controlled by 1D boundary movement,(Khawam & Flanagan, 2006) and

iv. spherical Fick's diffusion limited transformation.

Consequently, the Avrami and Bai models produce fits of similar qualities (figure 1.4 b, c). The Avrami model fit with exponent of 0.6 suggests a diffusion controlled crystallite growth, with reaction rate contribution from a strongly

decelerating nucleation rate. In comparison, the Bai model produces activation (nucleation) rates that are 10 to 30 times slower than the respective conversion rates, at an initial amount of activated particles of about 40%. Given the similar curve shape of nucleation and transformation limited models, mechanistic information cannot be extracted from the reaction rate information alone, but different *in situ* observations are necessary to determine the limiting mechanism with certainty. The choice of model and the observed fits are thus only relevant for comparison with other reaction rates observed in the $LiFePO_4$ system. However, one value, the activation energy, exhibits remarkable robustness with regards to the applied model. Moreover, the fact that this activation energy is the same for the two rate constants of the Bai model, suggests that not two, but only one rate contributing step exists, which does not seem to follow the simple statistical assumptions underlying these models. For the Avrami rate constant, as well as the two Bai model rate constants, the activation energy for this limiting step amounts to a comparably large(Allen, et al., 2007, 2012; Kuss, Liang, & Schougaard, 2012; Morgan, Van der Ven, & Ceder, 2004) 50 kJ mol^{-1} (figure 1.4 d).

The obtained Bai model parameters are surprisingly different from electrochemically obtained data,(Levi, et al., 2013) even though the material was obtained from the same source. The activation rates are in the same order of magnitude, however, the transformation rate is near 10 times larger during the chemical lithiation. This may very likely be an effect of the increased thermodynamic driving force of the chemical lithiation.

The present chemical lithiation study, as well as, the corresponding electrochemical results by Levi *et al.*(Levi, et al., 2013) produce results that are in stark contrast to the chemical delithiation. The delithiation exhibits larger rates and fits an Avrami exponent of one, thus fitting all the four listed situations above. In fact, the Bai model with two independent steps cannot produce reproducible parameters

for the delithiation data. Most notably, however, the delithiation rate is much less temperature dependent: the lithiation activation energy is nearly three times larger than the delithiation activation energy. Thus the delithiation reaction is clearly limited by a different mechanism than the lithiation reaction.

1.5 Conclusions

Chemical lithiation of lithium iron phosphate with LiI is a chemical model equivalent to an electrochemical potential step to about 3.0 V *vs.* Li/Li^+ (underpotential of 350 mV),(Yamada, Kudo, & Liu, 2001) with the distinct advantage that the entire sample and surface experience the same potential. The formation of iodine can be conveniently followed by *in situ* photometry, providing kinetic data on the progress of the lithiation reaction with sub second time resolution. The kinetic data fits the Avrami model at an Avrami exponent of 0.6, and follows the Bai statistical model with relatively slow nucleation. It is, as such, different from the known chemical *delithiation* kinetics, since it cannot be made to fit a simple one-dimensional solid solution diffusion model and exhibits a significantly higher activation energy. Thus, the underlying rate limiting mechanism must be different for the chemical lithiation and delithiation processes. Because a purely diffusion limited lithium (de-)intercalation would have to be largely symmetric with respect to the direction of lithium movement, the lithiation reaction cannot be solely limited by diffusion. The strong temperature dependence of the lithiation reaction rate also entails that, different from the charging reaction, it may be of interest to heat a discharging battery when withdrawing high peak currents.

1.6 Acknowledgements

Jean-Philippe Masse (CM^2) is acknowledged for his technical support. This work received financial support through the National Science and Engineering Research Council (NSERC), Grant CRD 385812-09.

CHAPTER II

ULTRAFAST CHARGING OF $LiFePO_4$ WITH GASEOUS OXIDANTS UNDER AMBIENT CONDITIONS

Whereas LiI can reduce $FePO_4$ to form $LiFePO_4$ and mimic the discharge reaction, we discovered that some gases oxidize $LiFePO_4$ by delithiation, forming $FePO_4$ and a lithium salt. Similar to the previous chapter, this reaction can be used to study kinetics *in situ*. A distinct advantage of this reaction for *in situ* studies is the low density of the gas, which reduces matrix effects in many analytical techniques, and fast diffusion of the gas, ensuring best possible control over concentration and distribution of the oxidant. The present chapter will introduce the discovered reactions and discuss their effect on the material properties.

This chapter has been published as research article in Chemical Science, 2013, 4(11), pp. 4223-4227. Christian Kuss, David Lepage, Guoxian Liang and Steen Brian Schougaard are co-authors of this article. The Electronic Supplementary Information for this article can be found in Appendix B.

The contributions of all authors are as follows:

- Christian Kuss: Design of experiments, experimentation with exception of electrochemical tests, XPS, XRD, data analysis, figures, discussion, redaction of manuscript
- David Lepage: Electrochemical tests, incl. data treatment, discussion
- Guoxian Liang: Discussion, Preparation of $LiFePO_4$ materials

- Steen Schougaard: Supervision, redaction of manuscript

2.1 Abstract

Lithium iron phosphate is a lithium-ion battery positive electrode material with widespread use, as well as unusually complex redox chemistry. Here we report on the discovery of a direct gas-solid delithation reaction. Unique to this reaction, in addition to the lack of solvent, is remarkably fast kinetics. *In situ* X-ray diffraction, corroborated by elemental analysis, shows for the first time that $LiFePO_4$ bulk diffusion supports nearly complete delithiation / charging of carbon coated $LiFePO_4$ micro powder at ambient temperature in less than 60 seconds.

2.2 Introduction

Electric cars are back on the mass market as an environmentally friendly mode of personal transportation. However, current consumers are cautious and voice concerns about long charging times which limits autonomy.(Graham-Rowe, et al., 2012) Importantly, speed of charge is related to slow transport kinetics inside the battery. This is, in turn, often associated with the kinetics of the lithium insertion/deinstertion reaction in the ceramic electroactive solid, since solid state diffusion generally is slow compared to the liquid and the gas phase.(Park, et al., 2010) Specifically, $LiFePO_4$ though superior in many aspects to other positive electrode materials, is criticized for low electronic conductivity and bulk lithium diffusivity.(Y. Zhang et al., 2012) Yet, in model systems, $LiFePO_4$ electrode materials repeatedly exhibit a much larger diffusion coefficient (around 10^{-8} cm^2 s^{-1})(Kuss, et al., 2012; Morgan, et al., 2004) than in $LiFePO_4$ powders designed for application (around 10^{-14} cm^2 s^{-1}).(Park, et al., 2010) Moreover, a limited number of experimental results have recently shown that commercially relevant $LiFePO_4$ might be capable of much higher charge/discharge rates, than previously thought. *E.g.* Ceder and co-workers published a controversial(Zaghib, Goodenough, Mauger, & Julien, 2009) study on a modified $LiFePO_4$ material with non-stoichiometric composition and amorphous surface layer, with which approximately 75% of the theoretical capacity could be achieved within a

one minute discharge.(Kang & Ceder, 2009) Similarly an electrochemical single particle study by Munakata and co-workers showed about 75% of the initial capacity at a one minute discharge.(Munakata, Takemura, Saito, & Kanamura, 2012)

At the same time, industry is concerned with the stability of $LiFePO_4$ in ambient atmosphere, as this is of great importance to the storage and handling of commercial $LiFePO_4$ during productions. *E.g.* complete transformation of $LiFePO_4$ into the NASICON analogue $Li_3Fe_2(PO_4)_3$ and *hematite* was observed during exposure to air at 300 °C and above,(Hamelet, et al., 2009) whereas at temperatures below 120 °C, in humid air, the formation of hydroxide containing compounds has been reported.(Brunetti, et al., 2011; Cuisinier et al., 2010) Yet, it remains unclear, why lithium is *not* extracted under oxidative aging conditions, even though this is the dominating mode of oxidation in solution.

To address this question of different reaction modes in air compared to electrolyte, and to shed light on the lithium transport kinetics of these reactions, we have examined different gaseous oxidants impact on commercial $LiFePO_4$. Surprisingly, we have found that even though exposure to O_2/O_3 did *not* significantly alter the $LiFePO_4$ materials, NO_2 consistently delithiates $LiFePO_4$ completely within a short period of time according to the following reaction:

$$LiFePO_4\,(s) + 2\,NO_2\,(g) \rightarrow FePO_4\,(s) + LiNO_3\,(s) + NO\,(g) \qquad [1.1]$$

This reaction differs significantly from previous oxidative delithiation transformations, as it does not include a liquid phase that can solvate the lithium ion and transport it away from the surface as the reaction progresses. More importantly, it exhibits unseen fast reaction rates for commercial $LiFePO_4$ materials.

2.3 Results and Discussion

2.3.1 Characterization

To confirm, that this reaction indeed is comparable to electrochemical charging, the solid reaction products have been characterized using attenuated total reflectance infrared spectroscopy (ATR-FTIR), X-ray diffraction (XRD), electrochemical cycling and transmission electron microscopy.

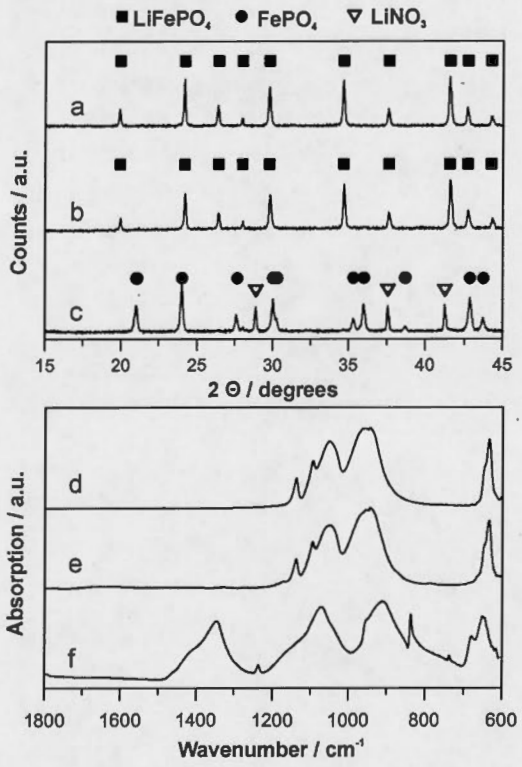

Figure 2.1 Crystallographic and chemical analysis of the reaction product of C-$LiFePO_4$ with O_3, and NO_2. X-ray diffractograms (a, b, c) and ATR FTIR spectra (d, e, f) of pristine C-$LiFePO_4$ (a, d), O_3 exposed C-$LiFePO_4$ (b, e), NO_2 oxidized C-$LiFePO_4$ (c, f). The symbols mark the location of strong reflexes according to literature crystallographic data.(Hönnerscheid, Nuss, Mühle, & Jansen, 2003; Rousse, et al., 2003; Wu, Fronczek, & Butler, 1994)

After treatment of carbon coated $LiFePO_4$ (C-$LiFePO_4$) micro-powders with NO_2, evidence of delithiation was given by $LiNO_3$ and *heterosite* $FePO_4$ as identified by ATR-FTIR and XRD (Figure 2.1 c, f). Specifically, the $LiNO_3$ gives rise to FTIR bands at 737 cm^{-1}, 838 cm^{-1}, 1072 cm^{-1}, 1135 cm^{-1} and a broad feature between 1300 cm^{-1} and 1500 cm^{-1}, as well as, a number of shoulders, which are added to the standard *heterosite* $FePO_4$ spectrum (Figure 2.1 f).(Malik, et al.)

The completeness of the delithiation was confirmed by atomic emission spectroscopy (AES): 100 ± 3 % lithium was extracted, while 2 ± 1 % lithium remained in the washed $FePO_4$ sample.

As the use of aggressive oxidants to delithiate $LiFePO_4$ might lead to the formation of non-crystalline by-products or particle dissolution, high resolution transmission electron micrographs of nano-sized carbon free $LiFePO_4$ were recorded to assess structural integrity of the reaction product. From Figure 2.2, it is clear that the overall shape, size and appearance of the particles remain unaltered. Furthermore, $FePO_4$ particles remain crystalline while a salt layer forms non-uniformly on the surface, accumulating in gaps and contact points. X-ray photoelectron spectroscopy reveals a nitrogen containing compound on the material surface. Figure 2.3 shows the nitrogen 1s peak at 406.7 eV, lying in between the values reported for $AgNO_3$ (Kaushik, 1991) and NH_4NO_3,(Aduru, Contarini, & Rabalais, 1986) thus suggesting the presence of $LiNO_3$ on the surface. The same references report O 1s peaks at 532.3 eV and 532.5 eV, which compares well to the observed component at 532.4 eV.

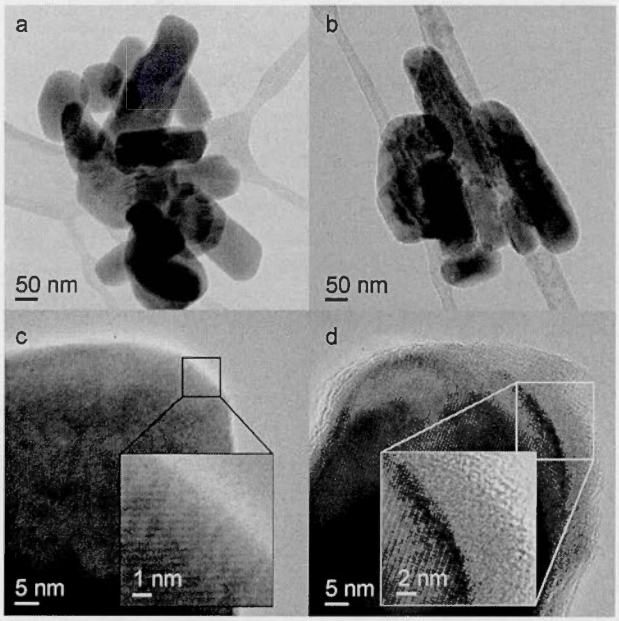

Figure 2.2 TEM images of $LiFePO_4$ before oxidation (a, c) and after oxidation with nitrogen dioxide (b, d). HRTEM images show crystallinity of particles up to the surface before oxidation (c) and an amorphous surface layer after oxidation (d).

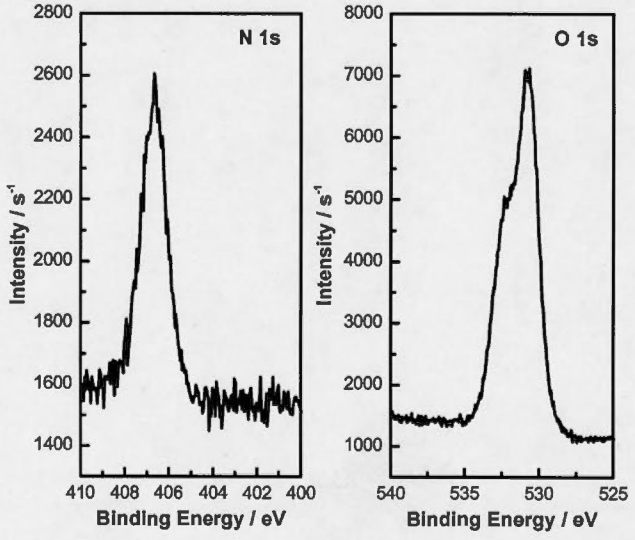

Figure 2.3 XPS analysis of the nitrogen and oxygen 1s peaks of the oxidized sample confirms the presence of $LiNO_3$ at the surface.

The electrochemical activity of oxidized C-$LiFePO_4$ was assessed in research coin cell batteries, assembled with great care to avoid any accidental short-circuit. Electrochemical testing was initiated in discharge mode, without prior charging. This first discharge (Figure 2.4a) indicates a stable potential plateau around 3.4 V vs. Li/Li^+ and practical capacity of 165 mA h g^{-1} (theoretical capacity: 170 mA h g^{-1}). Combined with the cycling stability over 50 cycles (Figure 2.4b), this indicates that the material retains its electrochemical properties and is not damaged by the aggressive delithiation.

As mentioned above, $LiFePO_4$ was also exposed to ozone. This gas did not lead to a significant alteration of the starting material, *i.e.* the bulk *olivine* structure remains intact, as observed in XRD, and further confirmed by only very minor changes to the ATR-FTIR spectrum (Figure 2.1 b, e).

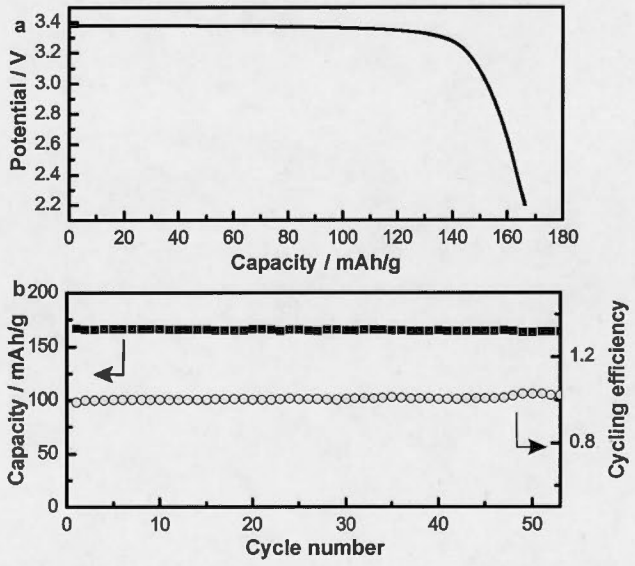

Figure 2.4 a) First cycle discharge curve (rate C/10) and b) cycling performance (rate C/2) of oxidized, washed and dried C-$LiFePO_4$ confirm complete oxidation and retention of electrochemical activity of the oxidized material.

Table 2.1 Gibbs free energies of delithiation reactions under reaction / ambient conditions.*(Dean, 1999; P. Zhang et al., 2008)

Reaction	$\Delta_R G$ / kJ/mol
$LiFePO_4 + ½\ Cl_2 \rightarrow LiCl + FePO_4$	-53
$LiFePO_4 + 2\ NO_2 \rightarrow LiNO_3 + FePO_4 + NO$	-65
$LiFePO_4 + ½\ O_3 \rightarrow ½\ Li_2O + FePO_4 + ½\ O_2$	-19
$LiFePO_4 + ½\ O_3 + ½\ H_2O \rightarrow LiOH + FePO_4 + ½\ O_2$	-60
$LiFePO_4 + ¼\ O_2 \rightarrow ½\ Li_2O + FePO_4$	+51
$LiFePO_4 + ¼\ O_2 + ½\ H_2O \rightarrow LiOH + FePO_4$	+11
$LiFePO_4 + ¼\ O_2 + ½\ CO_2 \rightarrow ½\ Li_2CO_3 + FePO_4$	-38

* 20°C, 20.9% O_2, 0.035% of CO_2, and 70% rel. humidity were assumed ambient conditions.

2.3.2 Thermodynamics of $LiFePO_4$ delithiations with gases

It is clear, that the key to the observed differentiated reaction behaviours lies within the nature of the oxidant. Table 1 summarizes some reaction Gibbs free energies for delithiation reactions of $LiFePO_4$ with different oxidizing gases using actual reaction conditions for NO_2, Cl_2 and O_3 oxidations, and ambient conditions for O_2. The thermodynamic discussion of oxidation pathways of $LiFePO_4$ with gases may further be extended to the extraction of iron ions from, or introduction of oxygen into the $LiFePO_4$ structure. However, molecular modelling shows, that those ions are strongly bound to their lattice site in the $LiFePO_4$ structure, compared to a more mobile lithium.(P. Zhang, et al., 2008) Bulk diffusion kinetics should hence favour delithiation reactions. Delithiation of $LiFePO_4$ with O_3 and O_2 in the presence of CO_2 is thermodynamically possible with free energies down to – 60 kJ/mol at standard conditions depending on the pathway.(Dean, 1999) This delithiation is *not* observed,

suggesting surface kinetics are responsible for its inhibition *e.g.* surface localized species may block the reaction. Given that ozone is a strongly oxidizing allotrope of oxygen, the reaction products of O_2 / $LiFePO_4$ and O_3 / $LiFePO_4$ may be quite similar, thus potentially yielding new information on the dry air aging mechanism of $LiFePO_4$.

2.3.3 Kinetics

In an attempt to quantify the exceptionally high reaction rate, *in situ* time resolved XRD was performed. Figure 2.5 shows evidence of complete delithiation of C-$LiFePO_4$ particles of 590 nm average diameter within significantly less time than one minute. The rate of delithiation was also confirmed by AES with 61 ± 14 % delithiation at 30 s and 94 ± 4 % delithiation at 60 s. This translates into a $LiFePO_4$ charge to 160 m A h g^{-1} within one minute. Importantly, the reaction temperature peaked at 29.7 °C ± 1.1 °C, thus excluding any major thermal increase of the kinetics resulting from the exothermic nature of the reaction. Moreover, preliminary tests using C-$LiFePO_4$ and Cl_2 have shown similar kinetics. $LiFePO_4$ nano-powder of approximately 200 nm average particle diameter with and without carbon coating have been studied as well. Regardless of the presence or absence of coating, these showed reaction rates that were too fast to be captioned with the 15 seconds time resolution of this conventional X-ray diffraction set-up.

For comparative purposes, our data provides a *lower limit* on the apparent diffusion coefficient of about 3.1 10^{-11} cm^2 s^{-1}, using a one dimensional pure diffusion model, as has been done in previous electrochemical studies.(D. Y. W. Yu, Donoue, Inoue, Fujimoto, & Fujitani, 2006) As such, this study shows that the rates provided by Ceder *et al.*(Kang & Ceder, 2009) and Munakata *et al.*(Munakata, et al., 2012) are entirely feasible *provided* that the removal of electrons from the particle surface is sufficiently fast.

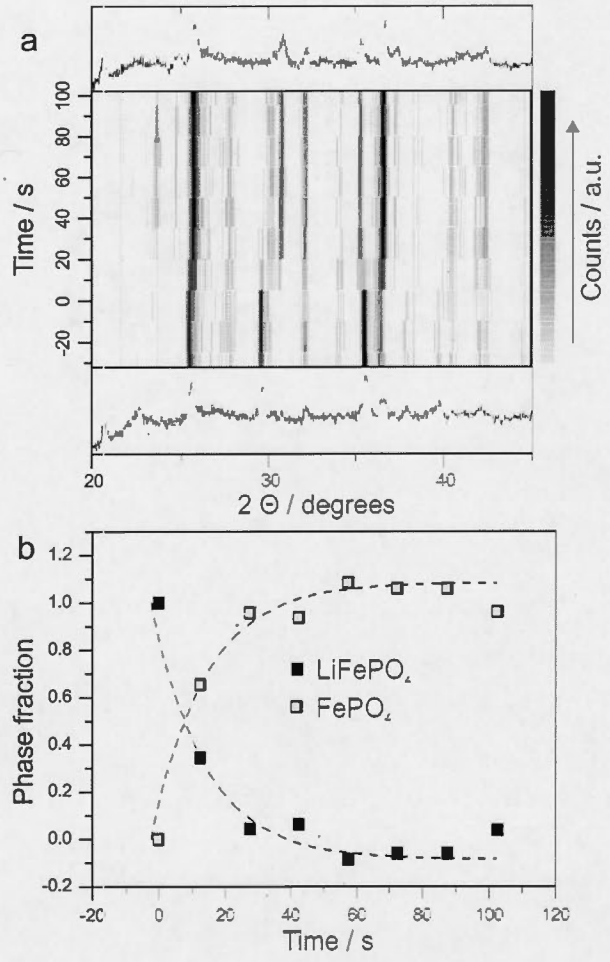

Figure 2.5 a) Time resolved XRD during delithiation of C-$LiFePO_4$ by NO_2 gas as a greyscale map. The initial and final diffractograms are displayed on top and bottom, respectively. t = 0 marks the time of gas injection. b) Composition of the mixture $LiFePO_4/FePO_4$. The composition was determined from time resolved XRD by integration and normalization to the corresponding theoretical intensity of the $LiFePO_4$ reflex at 30° 2θ and the $FePO_4$ reflex at 31° 2θ (based on a Cu Kα anode X-ray source).

2.4 Conclusions

Unique to the gas reaction discovered here, is the delithiation of $LiFePO_4$ at high speed *without* the presence of a liquid. *In situ* X-ray diffraction corroborated by elemental analysis provides proof that $LiFePO_4$ bulk kinetics supports a charge to 160 m A h g^{-1} in less than 60 seconds under ambient conditions. This finding has been confirmed with two $LiFePO_4$ materials resulting from different synthesis routes regardless of the presence or absence of carbon coating. The reaction is comparable to the electrochemical process in so far as the resulting $FePO_4$ is indistinguishable from electrochemically delithiated Li_0FePO_4 and the thermodynamic driving force corresponds to a charge to 4.1 V vs. Li/Li^+. It provides thus new possibilities to study the delithiation mechanism of $LiFePO_4$ *in situ* and *ex situ*. As such, XRD and TEM studies are currently underway. The findings further disprove the paradigm of slow lithium bulk diffusion in $LiFePO_4$.

In conclusion, the presented data suggest that developing $LiFePO_4$ materials with improved bulk lithium diffusivity will not improve rate capabilities of the derived lithium-ion batteries. Instead, electrode design, electronic conductivity and surface kinetics should be the focus of continued research.

2.5 Experimental

Micro-sized carbon coated $LiFePO_4$ (C-$LiFePO_4$, US Patent 7,457,018) and carbon free nano $LiFePO_4$ (US Patent 7,807,121 B2) were donated by Clariant (Canada) Inc. (former Phostech Lithium Inc).

C-$LiFePO_4$ (chemical and crystallographic analysis) and carbon free nano $LiFePO_4$ (used for XPS) samples were exposed to nitrogen dioxide and ozone gas respectively for at least 30 minutes. For chemical quantification of the oxidation, oxidized samples were washed in water and filtered. $FePO_4$ was subsequently dissolved in conc. HNO_3. Wash water and dissolved $FePO_4$ were analysed by AES.

To achieve time resolution, the oxidation was stopped after different exposure times by replacing NO_2 gas with a stream of dry air. TEM samples were prepared by depositing carbon free nano $LiFePO_4$ onto lacey carbon nickel grids from a suspension in acetonitrile. Select sample covered grids were exposed to NO_2 gas before analysis in the TEM. Carbon coated nano $LiFePO_4$ shows the same characteristics.

The electrodes for battery testing were produced by coating 85 wt-% washed, completely oxidized $LiFePO_4$, 6 wt-% PVDF binder and 9 wt-% carbon additive on to a carbon coated aluminium foil. The battery contained a metalic lithium negative electrode and a $LiPF_6$ in 1:1 ethylene carbonate and dimethyl carbonate mixture electrolyte.

Time resolved X-ray diffraction was performed using a flow of NO_2 gas below a filter paper on which $LiFePO_4$ was fixed. X-ray access to the XRD cell was enabled through a Kapton window. In similar experiments, the peak temperature of $LiFePO_4$ during NO_2 oxidation was recorded, using an infrared thermometer and confirmed in independent experiments with a thermocouple.

For more experimental details, suppliers and instruments, please see the Electronic Supplementary Information.

2.6 Funding

Clariant (Canada), Inc., who carried part of the costs of conducting this study, is a commercial producer of lithium iron phosphate.

2.7 Acknowledgements

The authors acknowledge gratefully technical assistance by Yanis Bouktit (elemental analysis), Michel Preda (XRD), Thierry Maris (time resolved XRD), Jean-Phillipe Masse (TEM), and Pascale Chevallier (XPS) as well as the National Science

and Engineering Research Council of Canada (NSERC), Grant no. CRD 385812-09 for financial support. The carbon coated Al foil was kindly donated by Exopack.

CHAPTER III

STRUCTURAL TRANSFORMATION OF $LiFePO_4$ DURING ULTRAFAST CHARGING

As the reaction has been established to be suitable to study ultrafast delithiation of $LiFePO_4$, the present chapter employs it for *in situ* diffraction with synchrotron X-rays. The ultrafast delithiation reaction could not be captured with standard XRD equipment in the previous chapter, but the high intensity X-rays of the Advanced Photon Source, together with fast resetting 2D X-ray detectors, allowed obtaining detailed structural information of the progress of this reaction.

This chapter is a prepared manuscript, soon to be submitted to a peer reviewed journal in form of a communication. Christian Kuss, Ngoc Duc Trinh, Stefan Andjelic, Eric Dufresne, Guoxian Liang and Steen Brian Schougaard are co-authors of this article. The supporting information for this article can be found in Appendix C and Matlab/Octave routines and functions employed in fitting diffraction data are given in Appendix F.

Additional *in situ* observations based on light absorption are presented in Appendix E.

The contributions of all authors are as follows:

- Christian Kuss: Design of experiment, experimentation, data analysis, figures, discussion, redaction of manuscript

- Ngoc Duc Trinh: Experimentation
- Stefan Andjelic: Experimentation
- Eric Dufresne: Set-up of beamline equipment
- Guoxian Liang: Discussion, lithium iron phosphate
- Steen Schougaard: Experimentation, supervision, redaction of manuscript

Improving charging rates is a major challenge in renewable electrical energy storage. *E.g.* consumer would more accepting of a 200 km electric car driving range, if recharging required only minutes rather than hours. Focusing on the lithium-ion technology due to its high energy density, the charging rate is ultimately determined by the constituent materials. Among these, lithium iron phosphate $LiFePO_4$ is a safe, environmentally benign, economical and competitively performing positive electrode material.(Padhi, et al., 1997; Zaghib, Mauger, Groult, Goodenough, & Julien, 2013) Recently, $LiFePO_4$ has also been shown to achieve remarkably fast extraction and insertion of lithium,(Huang, et al., 2012; Kuss, et al., 2013; Zaghib, et al., 2013) yet the underlying mechanism is still a subject of intense debate. Here, we use a unique gas-solid reaction to drive *complete* lithium extraction to the highest reported speed at ambient conditions, and simultaneously follow structural and electronic changes with high time resolution using *in situ* synchrotron X-ray diffraction and optical reflectance spectroscopy. We show that even in this ultrafast limit, phase separation competes with the kinetically accessed solid solution.

During charging and discharging, intermediate compositions between $FePO_4$ and $LiFePO_4$ are created. Under equilibrium conditions, these phase separate to the equilibrium compositions *heterosite* type $Li_{0.04}FePO_4$ and *olivine* type $Li_{0.96}FePO_4$.(Yamada, et al., 2005) This phase separation limits the number of lithium transporting species in the two equilibrium phases, and as such the lithium transport rate. The discrepancy between this apparent intrinsic limitation on lithium diffusion and the observed fast charging and discharging rates has led to the proposal of different mechanisms that facilitate lithium dynamics. The Domino-Cascade model(Brunetti, et al., 2011; Delmas, et al., 2008) assumes that phase separation prevails also under dynamic conditions, and lithium diffusion is enabled by a strained interface between the lithium rich and lithium poor phase. Yet, certain phase field and electronic structure models predict the suppression of the phase separation under dynamic conditions,(Cogswell & Bazant, 2012; Malik, et al., 2011) whereas others

rely on an interplay between amorphization and phase separation to explain *fast* lithium transport.(Kao, et al., 2010; Tang, Carter, Belak, & Chiang, 2010; Tang, Carter, & Chiang, 2010) Recent experimental evidence further shows extended solid solution ranges,(Orikasa, Maeda, Koyama, Minato, et al., 2013; Orikasa, Maeda, et al., 2013a, 2013b; Sharma, et al., 2012) that may be responsible for the high rate performance. *In situ* TEM has shown the formation of a wide interface between lithium rich and poor phases that exhibits intermediate lithium contents.(Niu et al., 2014) At high rates, recent *in operando* X-ray diffraction corroborates the formation of a metastable solid solution, that appears to suppress phase separation as the reaction rate is increased.(H. Liu et al., 2014) Importantly, interpreting particle scale properties using *in operando* X-ray diffraction based on battery-native electrochemical techniques is associated with significant difficulty. The main reason for this difficulty is an analytical response that consists of a convolution of particles reacting in different environments, due to electrode inhomogeneity and the electrochemical potential lost to internal resistances.(Malik, et al., 2013) Contrastingly, chemical redox reactions that mimic the electrochemical charging and discharging of battery materials are ideally suited to provide a homogenous environment over the whole sample *i.e.* the thermodynamic driving force is quickly balanced through fast reactant diffusion along short diffusion paths. The recently discovered high rate delithiation reaction of $LiFePO_4$ with the gaseous oxidant NO_2 provides thus an unrivaled opportunity to study the particle scale fast delithiation (charging) of $LiFePO_4$.(Kuss, et al., 2013) Importantly, it can be combined with visible and high intensity synchrotron X-ray light sources to obtain high time-resolution *in situ* X-ray diffraction from ultrafast charging $LiFePO_4$, as well as electronic spectra information, since carbon coating is not required.

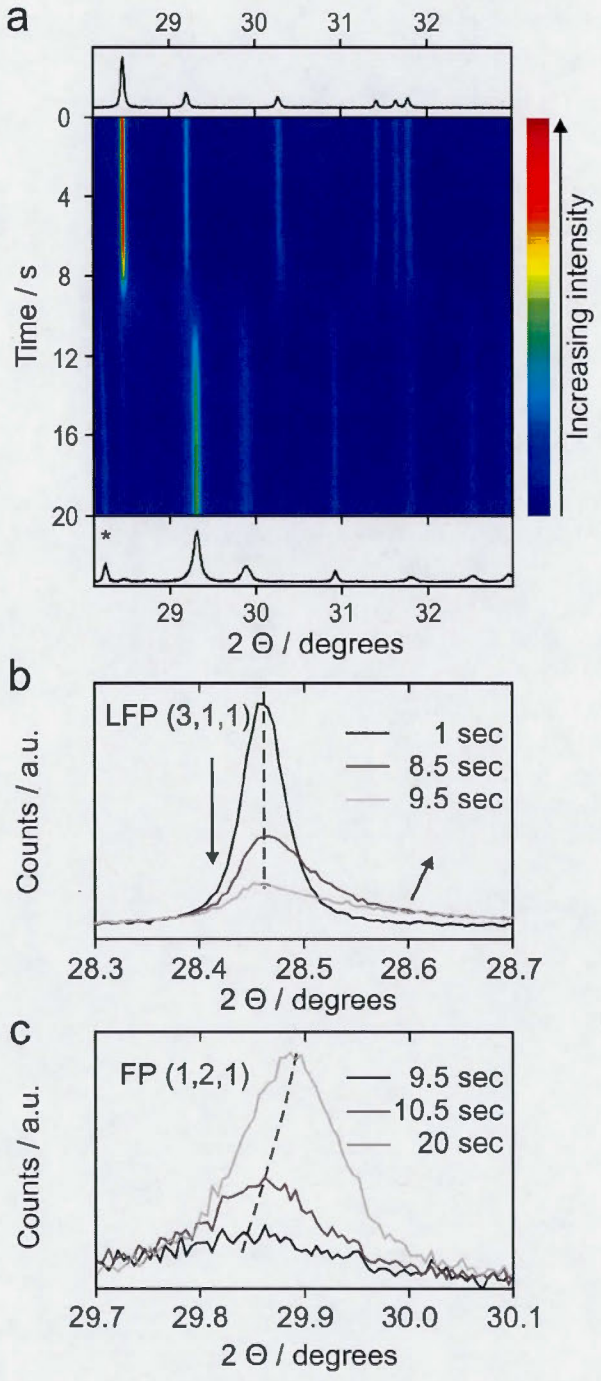
a
29
30
31
32
0
4
8
12
16
20
Time / s
*
Increasing intensity
2 Θ / degrees
b
LFP (3,1,1)
1 sec
8.5 sec
9.5 sec
Counts / a.u.
28.3
28.4
28.5
28.6
28.7
2 Θ / degrees
c
FP (1,2,1)
9.5 sec
10.5 sec
20 sec
Counts / a.u.
29.7
29.8
29.9
30.0
30.1
2 Θ / degrees

Figure 3.1 Time dependent diffraction during complete oxidation. a. Diffraction intensity *vs.* diffraction angle-time contour map. The top line plot shows the initial, the bottom line plot the final diffractogram (asterisks mark reflections of the $LiNO_3$ phase). Gas injection was started at 2 seconds, and was measured to arrive at the sample at 6 ± 1 seconds. b. $LiFePO_4$ (3,1,1) reflection during the phase transition (increasing time is displayed in lighter grey). The reflection intensity decreases and the peak width increases asymmetrically. (black arrows) Whereas the peak maximum remains largely unmoved (dashed line), the peak center shifts to higher angles. C. $FePO_4$ (1,2,1) reflection during phase transition. As the reflection grows the peak maximum shifts to higher angles (dashed line), whereas no significant peak asymmetry is observed.

The full delithiation of $LiFePO_4$ with NO_2 gas is shown in a time-diffractogram map in Figure 1a. NO_2 flow is started at time = 2 seconds, and the flow has been measured to arrive at the powder at about 6 seconds. After only 16 seconds, *i.e.* 10 seconds after the arrival of the gas, the material has been completely transformed to the lithium poor phase. The deintercalation of lithium during this structural rearrangement is further confirmed by the concurrent formation of crystalline $LiNO_3$. At well below 20 seconds, this complete transformation from $LiFePO_4$ to $FePO_4$ has never been observed at such speeds. This high rate made possible by the NO_2 gas phase reaction is especially noteworthy considering that commercial $LiFePO_4$ particles with diameters greater than 200nm was used here. During the 10 second transformation reaction, the initial single phase modifications within the lithium rich structure can be observed in the first 2 to 3 seconds. Subsequently, the lithium rich and lithium poor phase both exhibit considerable diffraction intensity during a period of at least 2 seconds.

Investigating the diffractograms of both phases individually, the lithium rich phase diffraction peaks widen with significant asymmetry as their intensity

diminishes, suggesting the formation of pronounced micro-strains (Figure 1b). Accordingly, the peak width has been quantified to increase to about three-fold the initial value. A significant volume of the lithium rich phase is as such strained, yet the diffraction angle of the lithium rich phase peak maxima, representing the bulk structure, remains largely unchanged. In contrast, the lithium poor phase bulk structure contracts as it crystallizes, as witnessed by the moving peak maxima (Figure 1c). The peak width reduces significantly during the phase transformation, but does not reach the value of the $LiFePO_4$ starting material, suggesting smaller crystallite size, residual symmetric strains or defects in this phase. Thus, qualitatively the lithium poor structure crystallizes homogenously with imperfections, whereas the lithium rich structure responds to its oxidation with pronounced local micro-strains.

In order to obtain bulk structural parameters and to quantify the observed strain, we fitted calculated diffractograms to the recorded patterns, allowing for the refinement of a bulk structure, representing the diffraction peak maxima, and an average structure, representing the diffraction peak means, thus accounting for peak asymmetry. Figure 2 shows that even the strongly strained *a* and *b* axes still exhibit an abrupt change of lattice parameters from one phase to the other. Further, no diffraction intensity is observable between the (4,1,0) reflections of the lithium rich and poor phases (Figure 3). Consequently, phase separation prevails even in this ultrafast limit.

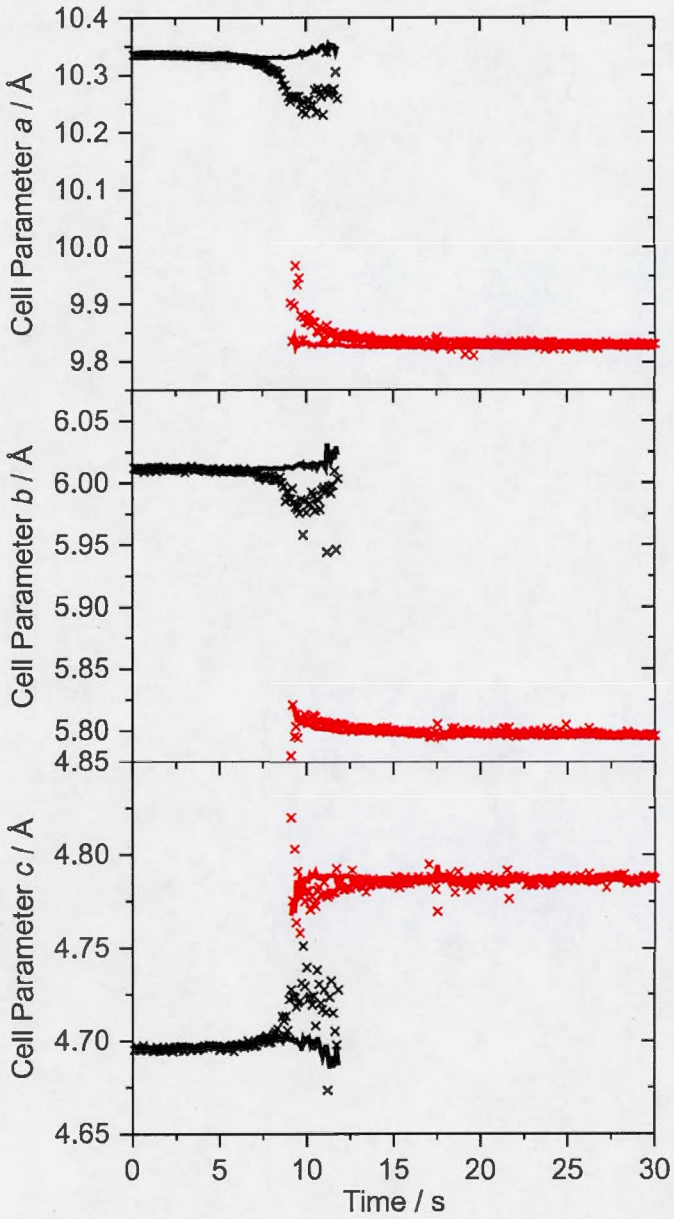

Figure 3.2 Structure refinement. a. Cell parameters of the bulk structure (lines), and the average structure (crosses) of the lithium rich (black) and lithium poor (red) phase.

The origin of the observed inhomogeneous strain of the lithium rich phase may be a compositional change, *i.e.* lithium concentration gradients, or formation of a coherent interface, which leads to coherency strain.(H. Liu, et al., 2014) Following Vegard's law, compositional strain would be isotropic, while coherency strain exhibits anisotropy, depending on the crystallographic orientation of the interface. The absence of significant anisotropy in the normalized strain favors inhomogeneous lithium solid solution rather than interface coherency as being responsible for the peak asymmetry. However, this solid solution would entail a phase with extensive iron mixed valance, as such, independent evidence of this mixed valance state would be required to confirm the assignment.

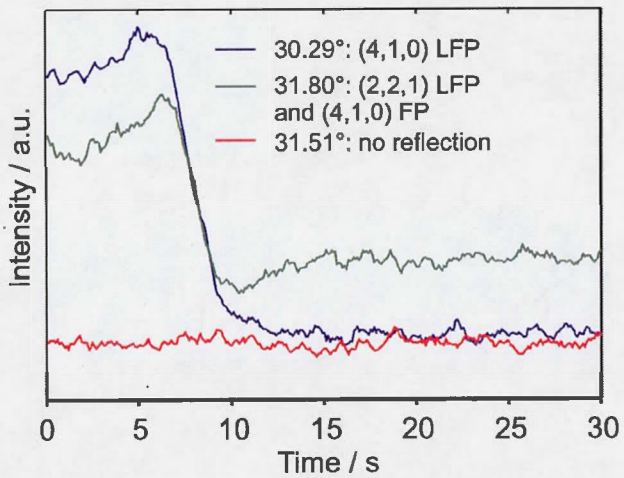

Figure 3.3 Diffraction intensity of the (4,1,0) reflections of $LiFePO_4$ (LFP) and $FePO_4$ (FP) and the background in between the two peaks. A continuous solid solution between both phases would entail an increase in the diffraction intensity of the background between the two peaks.

Importantly, Yamada *et al.* has made use of the particle size dependence of the stable solid solution ranges within Li_xFePO_4, to show that the mixed valence leads to a strong intervalence charge transfer band in the visible spectrum (shaded region in Figure 4a) .(Furutsuki et al., 2012) This transfer band has not previously been studied during dynamic delithiation, since the carbon coating required for electrochemical oxidation precludes its observation. During the chemical oxidation of *uncoated* $LiFePO_4$ (Figure 4b) a strong transient decrease in reflectance in the 600-900 nm region is observed, confirming the temporary presence of mixed valence. Moreover, the appearance of this feature correlates closely with the increase of diffraction intensity in a mixed valence region (30.46° 2 θ, corresponding to the strained (4,1,0) plane) of this slower reacting carbon-free sample (Figure 4d). The spectroscopic analysis therefore confirms that the observed diffraction peak asymmetry is an effect of a solid solution with inhomogeneous lithium concentration and mixed valence on the iron sites.

The concentration increase of both ionic and electronic charge carriers that ensues the extended compositional range of the mixed valance state induced by the dynamics of delithiation is required for the ultra high delithiation reaction rate witnessed here. Yet, the concurrent phase separation suggests that the kinetically accessible structures of intermediate lithium content still exhibit a transitional maximum in free energy. The energy barrier between the crystallographically distinct lithium rich and lithium poor phases would however be strongly modified by the smaller unit cell mismatch arising from the formation of the solid solution. In accordance, no buildup of the strained structure diffraction peaks, as the bulk $LiFePO_4$ peak is disappearing, can be found. Consequently, the conversion from the strained lithium rich to the crystallographically distinct lithium poor phase is not rate limiting.

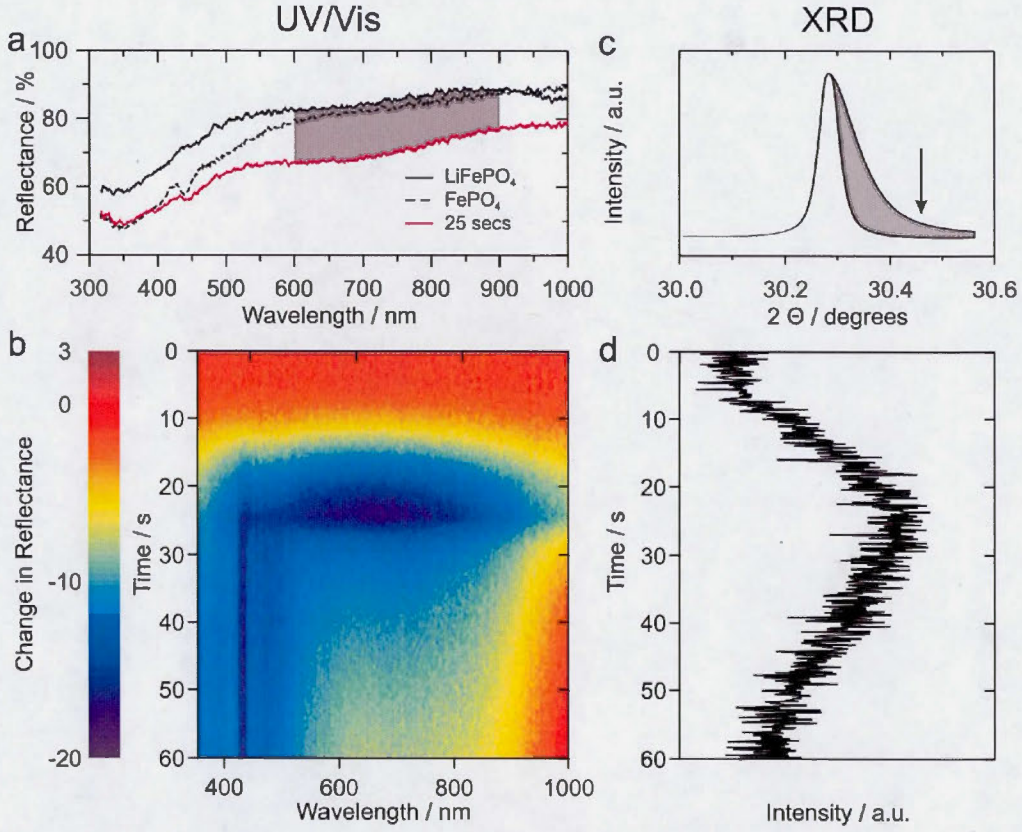

Figure 3.4 Evidence of the transient solid solution. a. Reflectance spectra of pristine $LiFePO_4$, $LiFePO_4$ after 25 seconds of NO_2 gas exposure, and $FePO_4$ showing a significant transient decrease in reflectance in the mixed valence region (shaded). b. Change in reflectance (%) from initial spectrum showing temporary decrease in reflectance in the mixed valence region from 600 to 900 nm and permanent changes due to the phase change and absorption by the NO_2 gas in the region up to 600 nm. c. Fitted (4,1,0) reflection of lithium rich phase during phase transition, showing significant asymmetry which accounts for composition strain. The arrow marks the angle chosen for the intensity plot in d. d. Temporary increase in diffraction intensity at 30.46 ° (asymmetry region of (4,1,0) reflection of the lithium rich phase).

In conclusion, the unique ability of the chemical oxidation to rapidly reach complete delithiation leads to unified $LiFePO_4$ reaction model valid for high rates, where *olivine* $LiFePO_4$ is partly delithiated to yield a strong concentration gradient and mixed valence, which is converted to a lithium poor *heterosite* phase, surprisingly without the phase transformation leading to severe rate limitations.

3.1 Methods:

Hydrothermally synthesized carbon coated $LiFePO_4$ powder was donated by Clariant (Canada), Inc. $LiFePO_4$ particles exhibit an average size of 243nm determined by dynamic light scattering.(Lepage, et al., 2014) Dry nitrogen dioxide / dinitrogen tetraoxide gas was obtained from Air Liquide.

Delithiations were performed in a specially made 316 stainless steel reaction chamber with Kapton® window for X-ray access. Filter paper (Whatman) was used to press the sample to the window, while allowing contact to the streaming gas. The layout of the cell is described in detail in reference (Kuss, et al., 2013). The temperature of the cell was controlled at 22 °C by connecting the stainless steel cell to a thermostat, using water as heat carrier. The time-resolved powder diffraction experiment was performed on the 7-ID beamline of the Advanced Photon Source.(Dufresne et al., 2010) The cell was mounted on a Huber 6-circle goniometer and illuminated by 10 keV X-rays. A Dectris Pilatus 100k detector was used at a 7.6 keV threshold level to minimize iron fluorescence interference. Gas flow was controlled using two independent computer controllable syringe pumps (KD Scientific and New Era), and glass syringes. For complete oxidation experiments, a 20 ml/min NO_2 gas flow started 2 seconds after the first diffractogram was recorded. Diffractograms were recorded at 10 Hz, using 95 ms collection time and 5 ms dead time, for 62 seconds (thus for 1 minute from the start of the gas flow). For partial oxidation experiments, the NO_2 gas flow started as well at 2 seconds, but was stopped at 4 seconds, to be replaced by a 20 ml/min air flow. For partial oxidation

experiments, diffraction data was recorded for 662 seconds (thus for 11 minutes from the start of the gas flow), whereas 100 diffractograms (10 seconds) were averaged per presented data point.

Data was treated using GNU Octave 3.6.4 and Matlab R2014a. Each detector image was transformed into an intensity - 2θ diffractogram. For each experiment 2θ was calibrated for the $LiFePO_4$ (9,1,1) reflection of the first diffractogram, systematically yielding a correction below 0.1 degrees. For 10 Hz data rate diffractograms, a boxcar filter over 6 adjacent diffractograms (0.6 seconds) was applied to reduce noise. Reflections of $LiFePO_4$ and $FePO_4$ in the angle range from 28.3° to 32.8° were fitted. Fitting was performed using split Pseudo-Voigt peak profiles for diffraction peaks, applying a different peak width below and above the maximum intensity, to account for the peak asymmetry and a tangent background. The fitting routine employed a least squares Levenberg-Marquardt algorithm, at which the squared residuals were weighted by the inverse of the X-ray counts of the respective point. For all displayed data, the smallest refined peak height of that phase is at least 5 times the standard deviation of the noise. Bulk structures were calculated, using the diffraction angle at the peak maxima. Average strains were calculated, using the diffraction angle of the peak means. Reference structures for strain calculation were obtained by averaging over the first 1.5 seconds for $LiFePO_4$ and the last 1.5 seconds for $FePO_4$ of the complete oxidation experiment. To obtain the anisotropic contributions to the interface strain, each calculated average strain per axis was normalized by the respective maximum expected interface strain, *i.e.* the misfit strain of a sharp coherent interface between the two reference structures along that axis.

For *in situ* UV/Vis reflectance measurements, delithiations were performed in the same reaction cell describe previously, replacing the Kapton® with a glass window for optical access. A mixture of uncoated LFP and NaCl (Bioshop, purity > 99.5%)

25% w/w was ground and placed on a filter paper for measurements. Ground NaCl on filter paper was used as reference. The cell was installed in a closed box to avoid ambient light contamination. The reflectance UV/Vis spectroscopy measurements were performed between 200nm and 1000nm with a reflection/backscattering probe (Ocean Optics, p/n: R-400-7-UV-vis), a deuterium-tungsten halogen light source (Ocean Optics, p/n: DH-2000-BAL) and detected by a high-resolution fiber optic spectrometer (Ocean Optics, p/n: HR-2000CG-UV-NIR). A 10 mL/min NO_2 gas flow started 10 seconds after the first spectrum was recorded. Reflectance UV/Vis spectra were recorded at a 500 msec acquisition time for a total time of five minutes. To treat the spectra, a boxcar over 5 points was applied along the wavelength axis. For figure 3.4b the difference in reflectance value at each point was determined in reference to the average spectrum over the initial 10 seconds.

3.2 Acknowledgements

This work received financial support through the National Science and Engineering Research Council (NSERC), Grant CRD 385812-09. Use of the Advanced Photon Source, an Office of Science User Facility operated for the U.S. Department of Energy (DOE) Office of Science by Argonne National Laboratory, was supported by the U.S. DOE under Contract No. DE-AC02-06CH11357

3.3 Competing financial interest statement

Clariant (Canada), Inc., who carried part of the costs of conducting this study, is a commercial producer of lithium iron phosphate.

CHAPTER IV

MODELING OF SITE EXCHANGE DEFECTS IN LITHIUM IRON PHOSPHATE AND IRON PHOSPHATE

The previous chapters explored the kinetic limits of industrial $LiFePO_4$ materials. These frequently contain crystallographic defects, most frequently antisite and site-exchange defects.(Badi et al., 2011; Boulfelfel, Seifert, & Leoni, 2011; J. Chen & Graetz, 2011; Chung, Choi, Yamamoto, & Ikuhara, 2008; Islam, et al., 2005) Such defects have been connected with performance issues of the material.(Malik, Burch, Bazant, & Ceder, 2010) The present chapter uses atomistic modeling, to investigate the influence of such defects on delithiation thermodynamics and the lithium mobility in the $LiFePO_4$ system. The goal of the investigation is to determine whether different synthesis conditions, which eliminate site exchange defects and are commonly more costly due to higher sintering temperature or longer sintering time, are likely to significantly improve the performance of the $LiFePO_4$ material.

This chapter has been published as research article in Journal of Materials Chemistry, 2012, 22(47), pp. 24889-24893. Christian Kuss, Guoxian Liang and Steen Brian Schougaard are co-authors of this article. Electronic Supplementary Information is presented in Appendix D and the source code of the program that was used in generating input files and analyzing output files for GULP can be found in Appendix F.

The contributions of all authors are as follows:

- Christian Kuss: Modeling and experimental work, data analysis, figures, discussion, redaction of manuscript
- Guoxian Liang: Discussion, lithium iron phosphate and iron phosphate samples
- Steen Schougaard: Supervision, redaction of manuscript

4.1 Abstract

A new set of potentials is presented that allows for modeling of the entire lithium insertion range of the lithium iron phosphate system (Li_xFePO_4, $0 \leq x \leq 1$). By comparing calculated values to experimental crystallographic, spectroscopic and thermodynamic data, the potentials ability to reproduce experimental results consistently and reliably is demonstrated. Calculations of site exchange defect thermodynamics and diffusion barriers for lithium and iron inside the lithium diffusion path suggest that site exchange defect related capacity loss may be justified exclusively by thermodynamic considerations. Moreover, a low activation barrier for iron transport in the lithium diffusion channel in $FePO_4$ brings into question the significance of the antisite iron ion as an obstacle to lithium diffusion.

4.2 Introduction

In recent years, interest in the global climate crisis has been rising. This interest and the belief that the limits of global fossil fuel resources exploitation are imminent(Lorca-Susino, 2008) have boosted the search for alternative energy sources and storage devices. Hence, lithium ion batteries are being developed on a massive scale for applications ranging from electric transportation to storage facilities buffering the energy needs of whole communities.(Testa, 2009) One very promising positive electrode material for medium to large lithium ion batteries is lithium iron phosphate ($LiFePO_4$),(Padhi, et al., 1997) as it is produced from low cost, non-toxic raw materials, is stable(Takahashi, Tobishima, Takei, & Sakurai, 2002) and achieves relatively high charge storage capacities with the theoretical limit of 170 mAh/g.(Padhi, et al., 1997)

Many different synthesis routes have been developed to produce what is nominally *olivine*-$LiFePO_4$,(Arnold et al., 2003; Cho & Chung, 2004; Franger, Le Cras, Bourbon, & Rouault, 2003; Palomares et al., 2007; Yang, Zavalij, & Whittingham, 2001) however, the material exhibits significant performance

differences depending on its preparation route.(Franger, et al., 2003) To achieve consistently the best possible product, it is therefore essential to understand the mechanisms behind these performance fluctuations. To this end material modeling plays a crucial role as a compliment to nanoscale characterization techniques like TEM *etc.*(Chung, et al., 2008; Dathar, Sheppard, Stevenson, & Henkelman, 2011; Delmas, et al., 2008; Fisher, Hart Prieto, & Islam, 2008)

Several modeling techniques have already been exploited to investigate $LiFePO_4$ batteries at different levels spanning from atomistic to macroscopic scales. At the atomic scale, *ab initio,*(Hou et al., 2008; Ong, Jain, Hautier, Kang, & Ceder, 2010; Ong, Wang, Kang, & Ceder, 2008; Ouyang, Shi, Wang, Huang, & Chen, 2004; Wang et al., 2008; Zhou, Maxisch, & Ceder, 2006) as well as empirical(Adams & Rao, 2011; Gardiner & Islam, 2010; Islam, et al., 2005) techniques have been employed to study $LiFePO_4$. Investigation of the Li_xFePO_4 system has been conducted very thoroughly using the computationally expensive first principles methods.(Ong, et al., 2011; Ong, et al., 2008; Ouyang, et al., 2004; Zhou, et al., 2006) Yet, approaching some of the system's central issues, such as defect chemistry and interface dynamics,(Yuan et al., 2011) these techniques quickly reach the available resource limits. Alternatively, using empirical techniques, as is the case in the present paper, makes it possible to investigate problems that require a several orders of magnitudes larger number of atoms to capture the central properties.

Most widely available empirical modeling software for ionic solids are based on calculations employing a set of interatomic empirical potentials. In the case of the $LiFePO_4$ system a set of potential parameters has previously been derived, however, for use exclusively with *fully* lithiated $LiFePO_4$.(Islam, et al., 2005) Other studies use a more general set of potentials, entailing a loss in specificity of the applied assumptions of the model.(Adams & Rao, 2011) By means of atomistic modeling, site exchange defects have been determined to exhibit a low defect energy.(Islam, et

al., 2005) Consequent investigation of antisite and site exchange defects led to the direct observation and quantification of these defects and the study of their effect on the materials performance.(Badi, et al., 2011; J. Chen & Graetz, 2011; Chung, et al., 2008) Depending on the preparation route site exchange defects can occur in concentrations up to 8%.(J. Chen & Graetz, 2011)

To investigate the whole compositional range of the Li_xFePO_4 system ($0 \leq x \leq 1$), a new set of potential parameters is presented here that covers the various iron oxidation states. Moreover, in a first application of this new set of potentials, we study the importance of thermodynamics in the lithium extraction process of $LiFePO_4$ with site exchange defects, as well as, lithium and iron ion mobility in the lithium diffusion channel of these materials.

4.3 Materials and Methods

4.3.1 Model and interatomic potentials

The modeled systems were represented by a group of point ions, signifying the ionic constituents of the real material and by interactions between these elements through empirical potential functions. The well-established General Utility Lattice Program (GULP) code by J.D. Gale was used for all presented calculations. It has been extensively reviewed elsewhere.(Gale & Rohl, 2003) The empirical potential method works particularly well for purely ionic systems, but can also be employed successfully for mixed ionic and covalent substances such as $LiFePO_4$.(Gardiner & Islam, 2010; Girard, Gale, Mellot-Draznieks, & Férey, 2001; Islam, et al., 2005) In this study, long range interactions, were modeled by simple Coulomb interaction, whereas short range repulsive and van der Waals interactions took on the form of the Buckingham potential.(Buckingham, 1938) These Buckingham pair potentials were applied for Li–O, Fe(II)–O, Fe(III)–O, P–O and O–O interactions. A shell model, binding a charged massless shell to the point ion of the core with a harmonic spring model,(Dick & Overhauser, 1958) was employed for the polarizable oxygen ions.

Table 4.1 Potential parameters

Interaction	Buckingham potential parameters		
	A_B / eV	ρ_B / Å	C_B / eV · Å^6
Li^+–O^{2-}	381.5244	0.30491	0
Fe^{2+}–O^{2-}	13207.008	0.22245	0
Fe^{3+}–O^{2-}	2111.9671	0.28941	0
P^{5+}–O^{2-}	1028.9741	0.33530	0
O^{2-}–O^{2-}	39.7594	0.47713	53.204
Species	Core charge	Shell charge	k_s / eV/Å^2
Li^+	+1	–	–
Fe^{2+}	+2	–	–
Fe^{3+}	+3	–	–
P^{5+}	+4.9708	–	–
O^{2-}	+0.9015	−2.8942	67.3564

As the potential parameters are dependent on the system being modeled, they have been fitted extensively to the experimentally found crystal structures of pure *olivine* $LiFePO_4$ and pure *heterosite* $FePO_4$ (see reference (Gale & Rohl, 2003) for a detailed account of the fitting procedure). In an advanced stage of the fitting process, the strongest vibrational frequency from the *heterosite* $FePO_4$ infrared spectrum was included as an observable parameter. The final optimized parameters are summarized in Table 1.

For the calculation of intermediate compositions Li_xFePO_4, primitive unit cells were created in which lithium defects were placed in different orderings. After geometry optimization the most stable configuration was chosen for further calculations. Intermediate oxidation states of iron, required for solid solution calculations, were treated using a mean field approach. The iron sites were thereby

assumed to be partially occupied by Fe(II) and Fe(III) at the same time, while their interactions were scaled by the appropriate factor. The vibrational energies and infrared activities of Gamma point phonon modes have been calculated from single point vibrational calculations of the relaxed structures.

4.3.2 Defect Calculations

For site exchange defect calculations, 50 super cells of 48 formula units each, containing randomly distributed site exchange defects for 1/12 or 1/24 of all crystallographic lithium and iron sites (corresponding to approximately 8% and 4% site exchange defects respectively) were used. Free energies of defects were obtained from single point vibrational calculations at the 0 K optimized structure with a Monkhorst-Pack grid of 2x2x2 k-points, where free energies were converged to 0.04 eV (at the chosen super cell size). No statistically significant change in the defect energies were observed when reducing the super cell size. Cited statistical errors are based on a 95 % confidence interval for a two-tailed Student distribution.

4.3.3 Diffusion Calculations

The ion diffusion activation barriers were calculated using the Mott-Littleton approach (Mott & Littleton, 1938) as implemented in the GULP code (Gale & Rohl, 2003) with a region 1 size of 14 Å and a region 2 size of 24 Å. Diffusion paths were obtained by displacing the moving ion along the *b*-axis and allowing relaxation in *a* and *c* crystallographic directions only. Diffusion coefficients have been estimated for room temperature using the Einstein-Smoluchovski equation. Perfectly anisotropic diffusion along the b-axis and an attempt frequency of $1.4 \cdot 10^{13}$ Hz was assumed. This frequency was derived from the phonon mode with strongest lithium movement along the *b*-axis in $LiFePO_4$. As the oxidation state of antisite iron ions is not known, the activation barrier for iron ion diffusion was calculated with the extreme values of the oxidation state, i.e. +2 and +3.

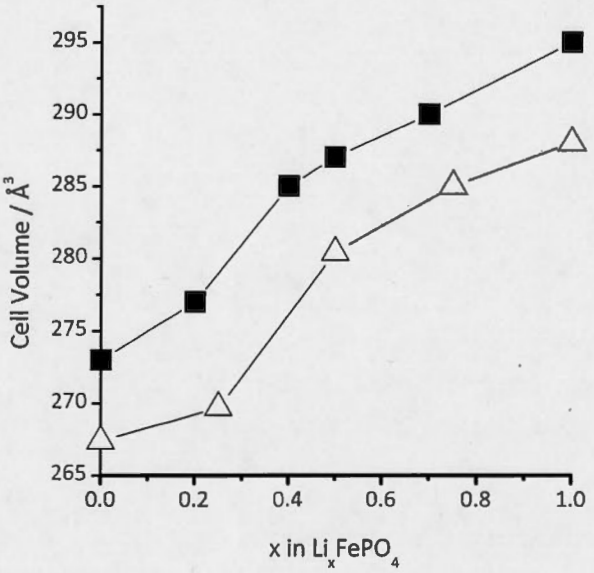

Figure 4.1 Experimental (solid squares, by Delacourt *et al.*(Delacourt, Poizot, Tarascon, & Masquelier, 2005)) and calculated (open triangles) cell volume as a function of composition in the solid solution Li_xFePO_4.

4.4 Results and Discussion

4.4.1 Potential validation

The crystal structure of both end members of the Li_xFePO_4 system is very well reproduced by the model (Table 2) with relative errors for crystal structure parameters within 0.5 %. The same general agreement can be found when comparing the calculated dielectric constant of $LiFePO_4$ to earlier results (electronic supplementary information). Properties and crystal structures of intermediate compositions Li_xFePO_4 have also been calculated. Li_xFePO_4 equilibrates into a two phase system under ambient conditions. However, when heating the phase separated material, a solid solution behavior can be observed.(Delacourt, et al., 2005) As shown in Figure 4.1 the experimentally found unit cell volume compares well to the calculated ones. Since the interatomic potentials have been fitted to ambient condition

structures while the experiment is conducted at 350°C the calculated unit cell is slightly smaller. Transferability of the potentials to other structures of composition $Li_xFe_yPO_4$ ($2y \leq 3\text{-}x \leq 3y$) is presented in the electronic supplementary information.

Crystal structures serve to evaluate a model's ability to predict local minima in the potential energy surface. However, in order to calculate most properties accurately, the curvature of the potential energy surface needs to be reproduced as well. To this end, tests of the reproduction of vibrational energies using infrared spectroscopic results showed strong correlation between calculation and experiment (Figure 4.2).

Table 4.2 Reproduction of experimental crystal structures

$LiFePO_4$	Calculated	Experimental (Rousse, et al., 2003)	Δ / %
a / Å	10.362	10.338	+ 0.2
b / Å	5.983	6.011	− 0.5
c / Å	4.680	4.695	− 0.3
$FePO_4$			
a / Å	9.763	9.760	+ 0.04
b / Å	5.740	5.752	− 0.2
c / Å	4.767	4.756	+ 0.2

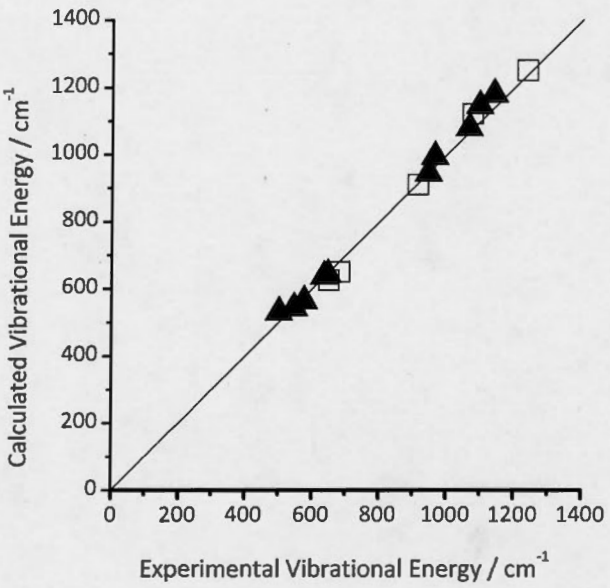

Figure 4.2 Correlation between calculated and experimental vibrational energies derived from infrared spectroscopy for $LiFePO_4$ (Burba & Frech, 2004) (solid triangles) and for $FePO_4$ (Trinh, Liang, Gauthier, & Schougaard, 2012) (open squares). Black line: Perfect correlation.

4.4.2 Lithium diffusion in $FePO_4$ and $LiFePO_4$

Olivine $LiFePO_4$, as well as, *heterosite* $FePO_4$ crystalize in the *Pnma* space-group. Lithium and iron thereby occupy 4a and 4c Wyckoff positions respectively. In the following, the abbreviation M1 for the crystallographic lithium site and M2 for the crystallographic iron site will be used. The mechanism of lithium motion in the Li_xFePO_4 system during battery operation is a subject of intense research and discussion, as such it is not yet clear if lithium moves through a lithium rich phase, a lithium poor phase, an interphase or in a solid solution.(Delmas, et al., 2008; Malik, et al., 2011; Prosini, 2005) However, it is generally accepted that lithium moves preferably along the *b* crystallographic direction.(Islam, et al., 2005; Li, Yao, Martin, & Vaknin, 2008; P. Zhang, et al., 2008) We therefore apply the technique employed

by Islam *et al.* to compare the movement of lithium ions in $FePO_4$ and $LiFePO_4$ within our model.(Islam, et al., 2005) The activation barrier for a lithium ion to move from one M1 site to the next along the *b*-axis was calculated to 0.415 eV in $FePO_4$ and 0.420 eV in $LiFePO_4$. Based on these values, the estimated lithium diffusion coefficient is $5 \cdot 10^{-10}$ cm^2/s in both $FePO_4$ and $LiFePO_4$. Moreover, investigating the diffusion path, little difference can be found between lithium diffusion in $LiFePO_4$ and $FePO_4$. It follows a curved trajectory, in order to maximize the distance to the positively charged iron ions. This is consistent with previously reported models.(Dathar, et al., 2011; Islam, et al., 2005) It has been suggested before that electron transport has a significant impact on ion diffusion barriers in the Li_xFePO_4 system.(Dathar, et al., 2011; Ong, et al., 2011) Nevertheless, the comparably good agreement of our calculations, which does not invoke electronic transport, with the experimental values of 10^{-11} - 10^{-17} cm^2/s is noteworthy.(Park, et al., 2010) Furthermore, site exchange defects exhibit little effect on the geometry of the $FePO_4$ framework. Hopping of an isolated iron antisite defect compared to an interstitial lithium iron in $FePO_4$ should thus mainly affect the activation energy of the iron hop, and not the electron hop.

4.4.3 Thermodynamics of delithiation of site exchange defects

Defects have frequently been used to explain the discrepancy between calculated and observed diffusion coefficients. (Dathar, et al., 2011; Malik, et al., 2010) Particularly, site exchange defects are a frequent finding, whereby a lithium ion is found in a M2 site, while an iron ion is found in the M1 site. (Badi, et al., 2011; J. Chen & Graetz, 2011; Chung, et al., 2008) The concentration of these defects may reach levels of more than 8%. (J. Chen & Graetz, 2011) At these concentrations, correlation between defects can have a significant impact on defect energies. We therefore investigated 50 super cells with 4 or 2 randomly distributed site exchange defects each (corresponding to approx. 8 % and 4 % defect concentration respectively).

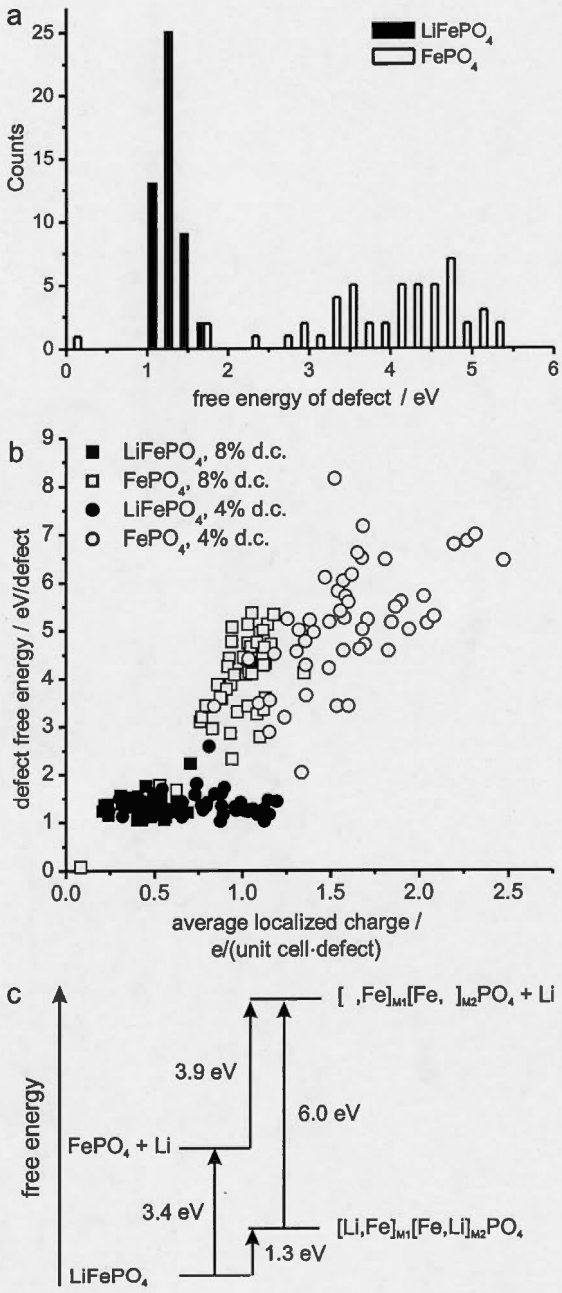

Figure 4.3 a) Histograms showing the distribution of free energies of defects in $LiFePO_4$ (solid bars) and $FePO_4$ (open bars) among 50 Super Cells with 8% site exchange defect concentration. b) Correlation of free energy of defects with average

local charge in $LiFePO_4$ (solid symbols) and $FePO_4$ (open symbols) at 8% defect concentration (squares) and 4% defect concentration (circles). c) Illustration of average site exchange defect energies in $LiFePO_4$ and $FePO_4$ and the consequence for electrochemical cycling.

Figure 4.3a illustrates the significant differences in defect energy and in width of energy distribution for $LiFePO_4$ and $FePO_4$ at 8% defect concentration. Free energies of defects in $LiFePO_4$ average to 1.3 eV, compared to 0.7 eV defect energy modeled by Fisher and Islam,(Fisher, et al., 2008; Islam, et al., 2005) while an average of 3.9 eV was found in $FePO_4$. Furthermore, correlations between the average defect energy and the position of the defects relative to each other were investigated. No statistically significant correlation could be observed in $LiFePO_4$ or $FePO_4$ with respect to average distance between point defects. However, the point defects are generally charged and as such the defect energy will likely depend on the local accumulation of charges. To assess this accumulation, a quantity was derived that we termed average localized charge. This value is calculated through integration of all charges within the volume of one unit cell, which is transposed across the relaxed super cell in ¼ unit cell length steps to obtain an average charge (Figure D.1). The average localized charge is therefore zero in a theoretically perfect crystal. In general we found that super cells that exhibit a larger localized charge, also exhibit larger defect energy. In addition this effect is correlated to the material lithiation state. As a point defect in $FePO_4$ (± 3e) is more highly charged than in $LiFePO_4$ (± 1e), generally, the average localized charge also increases. Defects in $FePO_4$ therefore have more significant long range effects compared to $LiFePO_4$. This difference in range of interaction provides an explanation for the strong energy difference observed between site exchange defects in $LiFePO_4$ and in $FePO_4$ (Figure 4.3b). The increase of defect charge during oxidation of iron and removal of lithium from the structure leads to a strong increase in defect energy. Especially empty M2 sites are highly unstable. Transferring this to the electrochemical charging process, it is possible to

calculate an additional potential necessary to fully oxidize $LiFePO_4$ containing site exchange defects.

From the reaction free energy of

$$[Li_{1-\varepsilon},Fe_{\varepsilon}]_{M1}[Fe_{1-\varepsilon},Li_{\varepsilon}]_{M2}PO_4 + [\ ]_{M1}[Fe]_{M2}PO_4 \rightarrow$$

$$[Fe_{\varepsilon}]_{M1}[Fe_{1-\varepsilon}]_{M2}PO_4 + [Li]_{M1}[Fe]_{M2}PO_4 \qquad [2.1]$$

this additional potential is estimated to 2.6 eV ± 0.5 eV at 25 °C (Figure 4.3 c), *i.e.* the potential *vs.* Li/Li^+ required to remove lithium from the antisite defects is 6.0 V. Electrolyte stability dictates an oxidation potential no larger than ~5 V *vs.* Li/Li^+ for most lithium ion batteries.(Xu, 2004) Consequently, in the absence of a concerted exchange of the defect lithium ion by another positively charged ion, this lithium is inaccessible to electrochemical cycling (Figure 4.4).

Even before removing the antisite lithium, oxidation of iron and removal of lithium ions will increase defect charge. Considering the aforementioned dependence of the defect energy on defect charge, a slight increase in the lithiation and delithiation potential relative to Li/Li^+ is therefore expected in the presence of site exchange defects.

Recent computational studies describe the kinetic hindrance of delithiation by the presence of iron in the lithium diffusion channel.(Dathar, et al., 2011; Malik, et al., 2010) It was concluded that this hindrance is large and decreases the diffusion rate by several orders of magnitude compared to the theoretical perfectly crystalline $LiFePO_4$. Even the slowest estimates by Malik *et al.*, however, allow lithium transport through a 1 μm particle within approximately 15 minutes. Nevertheless, a capacity loss of the order of the site exchange defect concentration has been observed experimentally in nano-sized particles after 30 minutes delithiation time.(Badi, et al.,

2011) The present study suggests that this capacity loss is thermodynamic, *i.e.* permanent.

4.4.4 Fe diffusion in $LiFePO_4$ and $FePO_4$

In the above mentioned computational studies iron was regarded as immobile in the M1 site. To the best of our knowledge this assumption has not yet been proven experimentally and can rapidly be tested using the new set of potentials. To this end, the mobility of iron ions in the M1 site along the *b*-axis in $LiFePO_4$ and in $FePO_4$ has been examined. With a transport barrier of 1.2 eV, the assumption holds true for $LiFePO_4$. However, in $FePO_4$, a low diffusion barrier of only 0.45 eV to 0.50 eV is observed. Iron in the M1 site in $FePO_4$ therefore exhibits a mobility that is comparable to lithium. The migration path in both cases resembles closely the path observed for the lithium ion, with a slightly larger deviation from the linear path. In turn this puts into question the ability of iron in the M1 site to block the diffusion of the lithium, as it can move to the particle surface where its behavior is difficult to predict, but could include, dissolution into the electrolyte, inclusion in the carbon coating or displacement into a surface defect site. This would lead to an increase in capacity during the first discharge/charge cycles as has been observed by several groups.(Morales, Trócoli, Franger, & Santos-Peña, 2010; Palomares, et al., 2007)

4.5 Conclusions

The presented set of potentials is a simple new tool to access accurate mechanical atomistic data across the complete composition range Li_xFePO_4 ($0 \leq x \leq 1$). Its estimate of the lithium diffusion barrier produces diffusion coefficients that are consistent with experimental values.

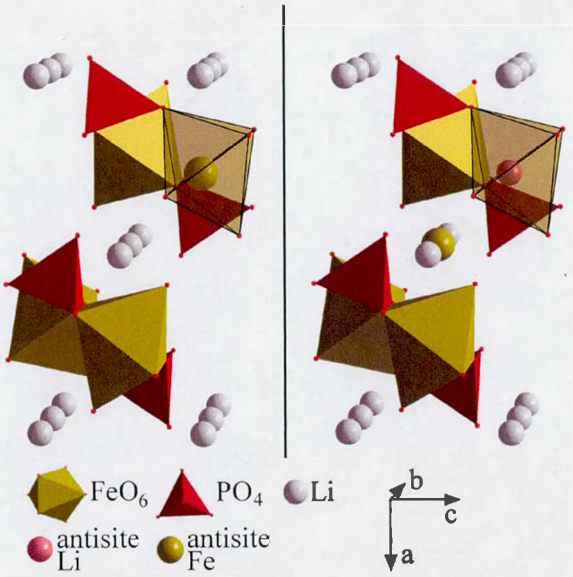

Figure 4.4 The site exchange defect. Left: crystalline *Pnma* $LiFePO_4$, Right: *Pnma* $LiFePO_4$ with site exchange. The lithium ion, which is hindered from delithiation, is tinted red.

While probing the site exchange defect, a strong dependence of the defect energy on defect charge is observed. As the charge of the site exchange defect increases during delithitation, an increase in the systems energy has been predicted. This increase was quantified and is especially substantial when removing antisite lithium and leaving an empty M2 site, making this lithium inaccessible to electrochemical cycling in common batteries. Together with calculations predicting high mobility of antisite iron in the iron phosphate lithium diffusion channel, these findings challenge the current view on the mechanism of battery performance depression due to site exchange defects.

4.6 Acknowledgements

The authors acknowledge gratefully Compute Canada's CLUMEQ for providing computational resources for this project and the National Science and Engineering

Research Council of Canada (NSERC), Grant no. CRD 385812-09 for financial support. We furthermore thank Dr. S. Islam for assistance and Dr. R. Cornut for helpful discussions.

CHAPTER V

SUMMARY AND CONCLUSIONS

The experimental findings, presented in the last four chapters, have provided specific insight into the lithium mobility in $LiFePO_4$ during fast redox reactions, and the influence of site-exchange defects from an atomistic model. While each chapter presents its own conclusions, all results together, including observations of the literature, may provide a deeper understanding of the overall dynamics of $LiFePO_4$ during charging and discharging. This is the goal of the present chapter.

5.1 Equilibrium thermodynamics of the Li_xFePO_4 system

Before revisiting the experimental results, the next three sections provide an overview over the current knowledge on the overall thermodynamics and kinetics of the Li_xFePO_4 system. Depending whether the oxidation of $LiFePO_4$ occurs in single phase or two phases, one would expect a different voltage response. The cell voltage is given by the lithium chemical potentials in the two electrode materials(Bruce, 1997)

$$E = -\frac{\mu_{Li}^{Li_xFePO_4} - \mu_{Li}^{Li}}{zF} . \quad (5.1)$$

For the electrode reactions [0.1] and [0.2], the chemical potential at the lithium metal electrode remains constant over the whole (dis-)charging range, since the Gibbs free energy changes linearly with the amount of lithium. At the lithium iron

phosphate electrode, however, the Gibbs free energy only changes linearly during a two-phase reaction. As such, the cell voltage slopes according to the chemical potential of lithium in a Li_xFePO_4 solid solution, whereas it remains constant during the two-phase reaction.

Figure 5.1 summarizes several hypothetical situations for the Gibbs free energy behavior of Li_xFePO_4. In an ideal solution, lithium is completely miscible over the whole insertion range. The lithium chemical potential changes slowly, and so does the cell potential. The second case displays the simplified Li_xFePO_4 system, showing two equilibrium structures near the end members of the solid solution. Here, a low energy path (dashed) exists, at which compositions in the miscibility gap decompose to the two equilibrium structures. As shown above, the cell voltage remains constant over the two phase reaction. The more likely scenario for Li_xFePO_4 is sketched in the third case. Here, metastable structures exist in the miscibility gap and other low energy paths are possible (dashed-dotted). The equilibrated system would still phase separate to the two equilibrium structures. However, kinetics may favor a different path.

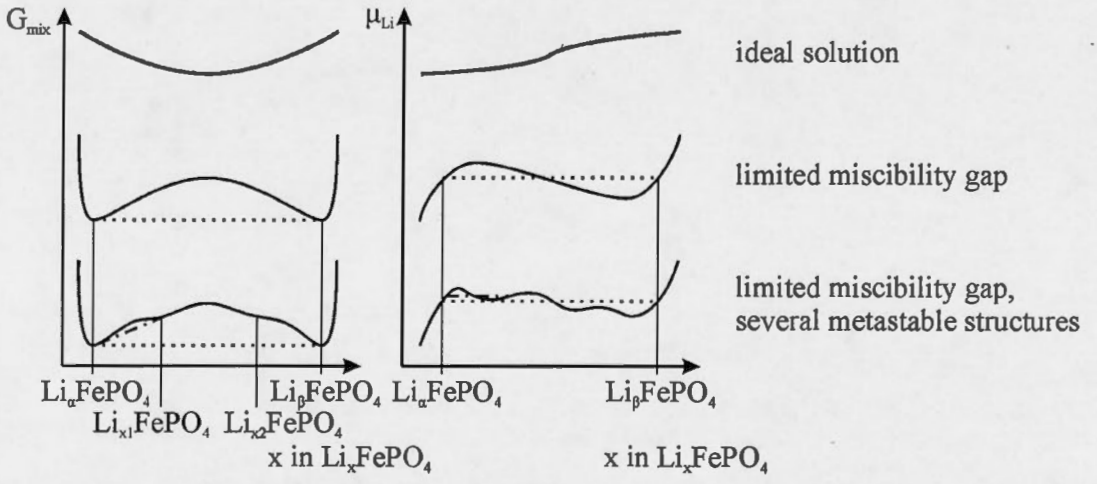

Figure 5.1 Three scenarios of the equilibrium thermodynamics of the Li_xFePO_4 system. The dotted lines indicate low energy paths.

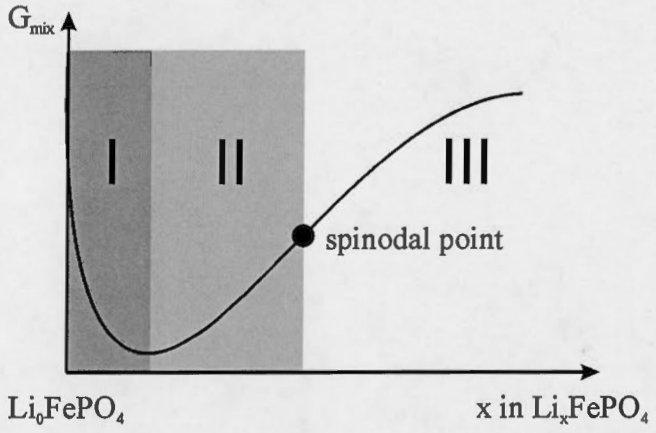

Figure 5.2 Three regions in the Gibbs free energy - composition curve: I. stable solid solution, II. metastable solid solution: nucleation-growth may occur if activation barrier can be overcome, III. unstable solid solution: at finite temperature spinodal decomposition occurs.

5.2 Non-equilibrium thermodynamics of the Li_xFePO_4 system

The kinetic behavior of the $LiFePO_4$ system depends on additional variables. Besides the Gibbs free energy curve, the presence or formation rate of nuclei of different phases, interfacial strains, temperature and size of the driving force all play a role in the pathway in which lithium is intercalated and deintercalated into $LiFePO_4$.

In principle, the system can follow different routes to relax to a lower energy state. For example, considering Figure 5.2 and lithiating $FePO_4$ the system will lithiate up to the low lithium concentration equilibrium structure $Li_\alpha FePO_4$ (region I) in a solid solution. From this point, lithiation can progress in two ways:

1. If the high lithium concentration equilibrium structure $Li_\beta FePO_4$ is present as nucleus in the same particle, or the nucleation rate is sufficiently fast (low activation energy, high temperature), the second phase will start growing at compositions in region II while $Li_\alpha FePO_4$ is diminished. As such, the lithium

intercalation will progress in the two equilibrium phases when $Li_{\alpha}FePO_4$ is reached.

2. If no $Li_{\beta}FePO_4$ nucleus is present, and nucleus formation is slow, the reaction will progress in a solid solution within region II until the curvature of the Gibbs free energy with x becomes negative at the spinodal point. Past that point, *i.e.* in region III, phase separation starts to occur by a process called spinodal decomposition,(Hebert, 2011) which is a diffusive process that is driven by local gradients in the chemical potential due to an unstable solid solution.

When the material is completely transformed to $Li_{\beta}FePO_4$, lithium will be further inserted in a solid solution.

Considering now the third scenario of Figure 5.1, nuclei of $Li_{x1}FePO_4$ or $Li_{x2}FePO_4$ would lead to the formation of intermediate phases during the lithiation. Their formation during spinodal decomposition depends on the activation barriers, applied potential and temperature. As such, kinetics may vary significantly, depending on the charging and discharging conditions.

5.3 The phase diagram of $LiFePO_4$

As explored in the last two sections, the curvature of the Gibbs free energy curve and the presence of metastable phases may be very important to the kinetics of $LiFePO_4$ lithiation and delithiation. As such, the present section explores features of the Li_xFePO_4 phase diagram. The earliest publications on this topic determined the values α and β of the equilibrium structures(Yamada, et al., 2005) and the temperature dependence of the solid solution.(Delacourt, et al., 2005)

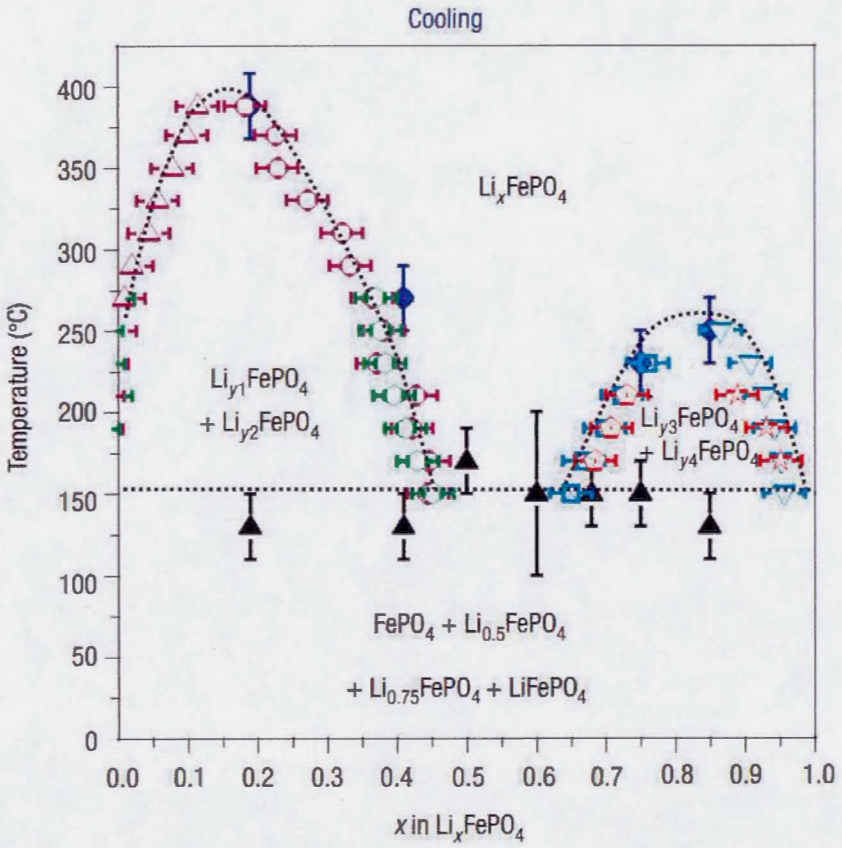

Figure 5.3 Phase diagram of 500 nm Li_xFePO_4 particles obtained by cooling the respective solid solutions. Reprinted by permission from Macmillan Publishers Ltd.: Nature Materials (Delacourt, et al., 2005) copyright 2005.

Yamada and co-workers determined α and β to be 0.032 and 0.962 respectively, based on interpretation of crystallographic structures of the equilibrium compositions with Vegard's law. Delacourt and co-workers took this study further and heated partially delithiated $LiFePO_4$, at which they found a transition from two phases to solid solutions Li_xFePO_4 at temperatures between 150 and 400 °C. Upon quenching of these solid solutions, they discovered two metastable phases near $Li_{0.5}FePO_4$ and $Li_{0.75}FePO_4$ (again based on Vegard's law). A large number of metastable structures

was also reported based on *ab initio* modeling of intermediate compositions with random ordering.(Malik, et al., 2011) The authors speculate that these structures enable a low energy solid solution pathway between $LiFePO_4$ and $FePO_4$, however without discussing the kinetic transitions between these ordered structures and failing to reproduce the negative free energy of mixing for the two equilibrium structures $Li_\alpha FePO_4$ and $Li_\beta FePO_4$, with respect to the $LiFePO_4/FePO_4$ mixture. The temperature dependence of the solid solution was further investigated by Chen and co-workers, who showed a strong size dependence of the limiting compositions and temperature dependence.(G. Chen, Song, & Richardson, 2007) This demonstrates that the free energy curve depends significantly on both temperature and particle size. This effect is highlighted by Zhu and co-workers, who furthermore find a dependence of the existence and stability of metastable structures on particle size.(C. Zhu et al., 2014)

It is not unexpected, that different behaviors of phase transition have been reported in the literature, due to the phase transition's dependence on temperature, applied potential, synthesis conditions (*i.e.* impurities and crystallinity), and crystallite size. Electrochemical lithiation of $FePO_4$ during TEM imaging was achieved with a solid electrolyte but only at very low rate. At such low rate, the $LiFePO_4$ system is more likely to relax to equilibrium conditions through nucleation and growth of the equilibrium structures. This is confirmed by the sharp phase boundary observed by (Y. Zhu, et al., 2013). *In operando* studies with standard electrochemical cells were conducted by Orikasa and co-workers, who found the formation of a metastable phase, which became more pronounced upon fast cycling.(Orikasa, Maeda, et al., 2013a) This would be in line with nucleation and growth of a metastable phase as suggested in scenario 3 of Figure 5.1. As this is the only publication reporting the formation of this phase, it may be unique to this $LiFePO_4$ material, *e.g.* impurity phases may facilitate nucleation and growth of this metastable phase. Other *in operando* work found extended solid solutions near the

equilibrium structures in concert with a two phase reaction mechanism,(Orikasa, Maeda, et al., 2013b; Sharma, et al., 2012) likely due to oversaturation of the solid solution with lithium vacancies or lithium interstitials, because of delayed nucleation of the second phase, possibly even leading to spinodal decomposition.

Deviating from the scenarios in Figure 5.1, which consider the $FePO_4$ framework constantly crystalline, Kao and co-workers reported the formation of amorphous Li_xFePO_4 upon cycling at intermediate overpotentials by *in operando* XRD, while they showed a crystalline to crystalline phase transition at low and high overpotentials.(Kao, et al., 2010) This brings crystallinity into play as third dimension to the free energy curve. Even though measurements of the amorphous-crystalline phase transition have been performed,(Gorzkowska, Jozwiak, Garbarczyk, Wasiucionek, & Julien, 2008) neither its activation energy nor the crystallization energy have been reported.

In summary, the literature confirms the theoretical considerations, and shows a multitude of possible reaction pathways for $LiFePO_4$. As such, it may be possible to define the most effective pathway, that allows fast lithium transport at low cost, and direct further material development to enable this process.

5.4 Combined discussion of chapters I to IV

How do these considerations affect the interpretation of the research results presented earlier? In general, it is safe to assume, that initially (*i.e.* up to the equilibrium concentration) the particle reacts in solid solution (Figure 5.4, second step). The amount of material that can react in this solid solution region is dependent on particle size and charging/discharging rate, since at high rate, only a surface layer may be affected. In the absence of nuclei of the second phase, this reaction proceeds further in solid solution up to the point at which the reaction driving force is compensated by the positive mixing free energy (Figure 5.4, third step). If this point exhibits a negative second derivative of the Gibbs free energy with respect to the

lithium concentration, spontaneous spinodal decomposition leads to nucleation of the second phase (Figure 5.4, left). If, however, the second derivative is still positive and $FePO_4$ nuclei are absent, nucleation (again by spinodal decomposition) is an activated process (Figure 5.4, right). The new phase grain first propagates along the faster diffusing *b* and *c*-directions (Amin, Balaya, & Maier, 2007) and hence forms an interface perpendicular to the crystallographic *a*-axis. This way, a reacting grain is produced, that grows at a lithium diffusion dependent rate, similar to the proposed Domino-Cascade model (see section 0.1.2.1). In chapter III, we report on an initial single phase delithiation, followed by strong anisotropic and asymmetric strains of the lithium rich phase, which reach 100% of the expected misfit strain of a coherent interface in the (100) plane. During the consumption of the lithium rich phase, the lithium poor phase crystallizes with slowly relaxing cell parameters. This is consistent with the described nucleation by spinodal decomposition. Crystalline domain size may reduce due to the formation of several nuclei per particle, or partial amorphization near the interface, in accordance with (Kao, et al., 2010) and (Tang et al., 2009).

The chemical lithiation reaction should behave similarly to the delithiation, if the free energy curve was symmetric. However, in chapter I we observe a quite different Avrami exponent for the chemical lithiation, compared to the chemical delithiation. This may be due to an asymmetric free energy curve, such that its inflection point, *i.e.* the point at which spinodal decomposition can occur, lies at higher mixing free energies on the lithium poor side than on the lithium rich side. This would lead to a higher activation energy for spinodal decomposition. In the Avrami model, this is reflected in a lower nucleation rate, and as such reduces the Avrami exponent, as well as the overall reaction rate.

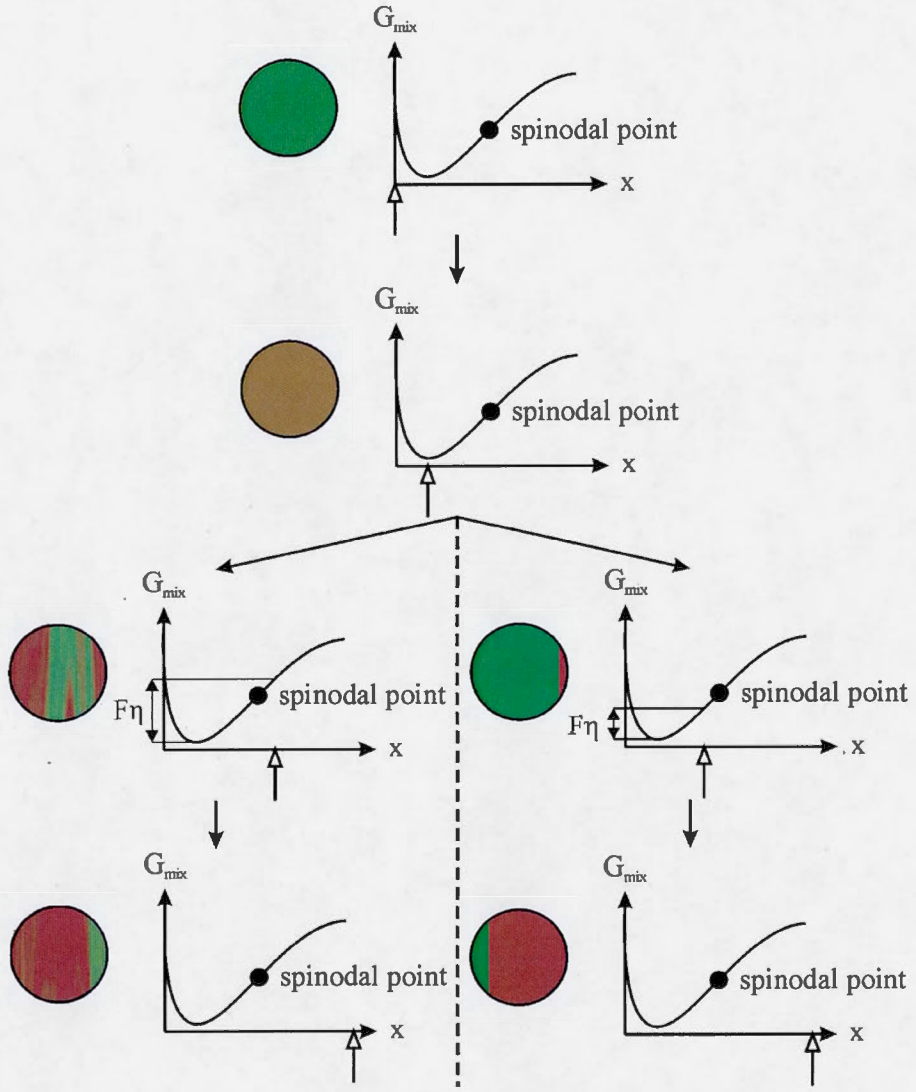

Figure 5.4 Dependence of $FePO_4$ lithiation mechanism on overpotential. Empty arrowheads indicate approximate overall composition. Lithiation proceeds initially in solid solution. Depending on thermodynamic driving force (overpotential $F\eta$ or reaction Gibbs free energy) the reaction proceeds by spinodal decomposition (left) or nucleation-growth (right).

Finally, since nucleation occurs by spinodal decomposition, initially immobile iron antisite defects may retain lithium longer during the first charge reaction. As delithiation continues, these defects would then become mobile if liberated from the lithium environment (chapter IV). As such, they may be one reason for the observed slower relaxation of the lithium poor phase in chapter III. Contrastingly, they should play a decreasing role or no role at all, in consequent cycling reactions, as they are removed during complete oxidation of $LiFePO_4$.

It is noteworthy, that while divalent cations are commonly regarded less likely to be mobile in a solid framework, a recent study has confirmed such mobility in $FePO_4$ (Zhao, Si, Liu, He, & Liang, 2013). The authors showed a small extent of intercalation of Mg^{2+} ions into $FePO_4$ when in competition with Li^+ ions. Mg^{2+} ions exhibit an ionic radius that is in between the Fe^{2+} high spin and low spin state ions (Dean, 1999).

5.5 Summary

The collected results in this dissertation suggest that $LiFePO_4$ is delithiated even at ultrafast rate following a domino-cascade type model. Nucleation of a non-equilibrium phase is initiated by local spinodal decomposition that leads to the formation of an oriented interface. Consequently, this non-equilibrium phase grows, while it is continuously depleted of additional lithium. Hence, at constant potential, the reaction is initially slow, as it is limited by the small number of mobile species in the lithium rich phase. As nucleation of the lithium poor phase occurs, lithium is rapidly removed from the structure. This conclusion is supported by findings of *in situ* photometry, as presented in Appendix E. A similar process likely occurs in the lithiation reaction, whereas nucleation rate is smaller, due to a higher activation energy for the local spinodal decomposition. Iron antisite defects play only a minor role in the kinetics, and are removed from the structure upon cycling.

It appears that the fastest rate delithiation of $LiFePO_4$ occurs at non-equilibrium interface structures, which support faster diffusion due to a higher concentration of mobile species. This is not unexpected and underlines the importance of the search for electrode materials that transport lithium in a solid solution, such as the lithium iron phosphate glasses. However, solid solution behavior is not a requirement for fast lithium (de-)intercalation. Phase separation mechanisms from oversaturated solution in fact impose an additional driving force to move species in the solution. Thus, while phase separation leads to a lower concentration of mobile species, these mobile species experience not only a concentration gradient dependent driving force, but also a chemical potential gradient. Consequently, their diffusion rate may even be faster, than in solid solution. These results may be confirmed by single particle studies, *e.g.* fast *in situ* microscopic electron and X-ray diffraction and microscopy. To be meaningful, such studies should take care to distribute the thermodynamic driving force over the complete particle surface.

5.6 Outlook

According to the presented results, improved kinetics of phase-transition electrode materials may be achieved by reducing the activation energy for spinodal decomposition. Possible paths to attain this goal include the introduction of dopants or the directed design of nucleation sites for intermediary structures.

Regarding the overall kinetics of lithium batteries, it is clear that $LiFePO_4$ is currently not limiting their charging and discharging rate. Consequently, improving battery kinetics is tied to the improvement of kinetics at the negative electrode and the electrode/battery design. *E.g.* promising results have been achieved with the negative electrode $Li_4Ti_5O_{12}$ (Zaghib et al., 2014) and work is currently underway in the laboratory of Professor Schougaard, analyzing porosity and tortuosity effects of electrodes on lithium mobility, and reducing lithium transport paths in batteries with 3D intertwined electrodes.

In all, the presented findings provide a positive outlook: electrode materials can be completely charged and discharged in less than five minutes, and there is no intrinsic obstacle that impedes lithium and electron storage and extraction at such rates. Therefore, considering the intensity of research efforts in this area, it may not take long until whole lithium batteries can be completely charged within a few minutes.

APPENDIX A

SUPPORTING INFORMATION TO KINETICS OF HETEROSITE IRON PHOSPHATE LITHIATION BY CHEMICAL REDUCTION

A.1 Treatment of *in situ* photometry data

In situ photometry data of the iodine formation was fitted to the Avrami model (Johnson Mehl Avrami Kolmogorov, or JMAK) by least squares fit to the linear form:(Khawam & Flanagan, 2006)

$$\ln(-ln(1-\alpha)) = n_a \cdot \ln(t) + n_a \cdot \ln(k)$$

Where α is the volume fraction of transformed material, n_a is the Avrami exponent, t is the time and k is the reaction rate constant.

It can be shown, that for an Avrami exponent of one, this equation becomes equivalent to first order reaction kinetics, as well as, a one-dimensional Fick's diffusion model.(Lepage, et al., 2014) The data was also fitted to the derived spherical diffusion model:

$$-\ln(1-x) = \frac{\pi^2 D_{Li}}{4R^2} \cdot t$$

Whereas D_{Li} is the lithium diffusion coefficient and R is the average particle radius.

Table A.1 Rate constants and Avrami exponents at different temperatures.

Temperature / °C	7	24	40	58
Rate constant k / 10^{-3} s^{-1}	1.86	6.56	31.1	107
Avrami exponent	0.59	0.55	0.59	0.57

APPENDIX B

ELECTRONIC SUPPLEMENTARY INFORMATION TO ULTRAFAST CHARGING OF LIFEPO$_4$ WITH GASEOUS OXIDANTS UNDER AMBIENT CONDITIONS

B.1 Experimental Information

All $LiFePO_4$ materials donated by Clariant (Canada) Inc., (former Phostech Lithium Inc.) were research grade. Micro-sized carbon coated $LiFePO_4$ (C-$LiFePO_4$) was produced according to US Patent 7,457,018. Carbon free $LiFePO_4$ nano-powder was produced according to US Patent 7,807,121 B2. Particle size distribution of C-$LiFePO_4$ was determined using dynamic light scattering (Zeta Plus Brookhaven Instruments Corporation).

Static XRDs were recorded on a Siemens D5000 diffractometer using a Co Kα X-ray source. ATR FTIR was performed on a Thermo Scientific Nicolet 6700 FTIR spectrometer with a diamond ATR crystal Smart iTR accessory in the wavelength range from 550 cm^{-1} to 4000 cm^{-1}. XPS spectroscopy was performed with a PHI 5600-CI (Physical Electronics) XPS spectrometer using an Mg Kα anode. Calibration was performed by shifting the C 1s peak to 284 eV.

XRD and ATR FTIR spectroscopy were accomplished on samples exposed to high concentrations of nitrogen dioxide (Praxair), chlorine (Linde) and ozone (Welsbach T-408 Ozone Generator, 3-5 % O_3 in dry O_2 flow) gas respectively for at least 30 minutes. The wet nitrous oxide gas mixture produced in the reaction of

copper with concentrated nitric acid led to the same results as presented for nitrogen dioxide.

The samples for atomic emission spectroscopy (AES) were washed with water and filtered. Washed $FePO_4$ samples were dissolved in concentrated nitric acid. The wash water and the dissolved $FePO_4$ were analysed at 670.8 nm by AES to determine the lithium content. The reported confidence interval is based on a Student's t distribution at the 95% level using at least three measurements.

The samples for transmission electron microscopy (TEM) were suspended in acetonitrile and brought onto a lacey carbon TEM grid. Oxidation was then performed directly on the grid. Transmission electron micrographs were recorded on a Jeol JEM-2100F microscope with an acceleration voltage of 200 kV.

For battery testing, carbon coated nano $LiFePO_4$ was oxidized using dry NO_2 gas (Praxair). Completion of oxidation was confirmed by ATR FTIR. The product was then washed and dried at 60 °C under vacuum. A coating was prepared from a suspension of 85 % w/w active material, 6 % w/w PVDF binder (Kynar KF Polymer W#1100) and 9 % w/w carbon additive (Super C65 Timcal) in N-methylpyrrolidone (Sigma Aldrich) on carbon coated Al foil (Exopack #2651). The electrode coating thickness was 10 μm with a density of 0.6 g/cm^3. A CR2032 type coin cell battery was prepared from this coating with a metal lithium anode (Alfa Aesar, 99.9 %), polyethylene separator (Celgard 2500) and a $LiPF_6$ electrolyte in 1:1 ethylene carbonate and dimethyl carbonate mixture (BASF, Materials No 50316367). The battery was subsequently cycled under constant current conditions between 2.2 V and 4.2 V on a MTI Corporation BST8-WA eight channel battery cycler at a C/10 rate for the first cycle and a C/2 rate for subsequent cycles up to 53 cycles. Rate performance was subsequently tested on a Bio-Logic VMP3 8 channel potentiostat at a charge rate of C/5 and discharge rates from C/2 to 15 C.

Time resolved X-ray diffractograms were recorded on a Bruker D8 Discover diffractometer using a Cu Kα X-ray source and a HI-STAR area detector. Dry NO_2 gas was injected through a syringe pump injection system at a speed of approximately 20 ml/min. The gas was guided through Teflon® tubing to a Teflon® reaction chamber (Figure B.1). There it passes underneath a filter paper and is evacuated through Teflon® tubing opposite the inlet. The sample (~10 mg) was placed onto the filter paper and covered with Kapton® film. The cell was then sealed using a metal disk and Teflon® tape.

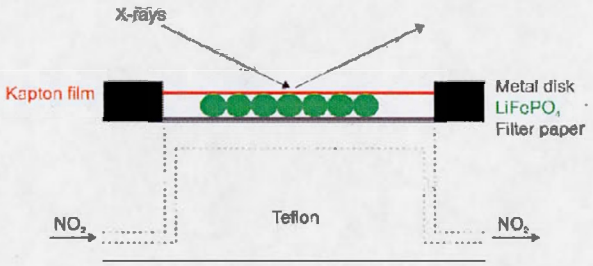

Figure B.1 Schematic representation of the *in situ* XRD cell.

The temperature was recorded in similar experiments without X-ray irradiation, using an infrared thermometer or a thermocouple, measuring three oxidations with each method.

The *ex-situ* time resolved AES was performed by introducing a wet NO/NO_2 gas mixture into an evacuated vessel at time t = 0 and removing the gas with a flow of dry air at time t. The formed lithium salt was then dissolved and quantified as described above.

For calculations of the thermodynamics of delithiations of $LiFePO_4$ with gases, 20°C, 20.9% O_2, 0.035% of CO_2, and 70% rel. humidity were assumed.

The diffusion coefficient was estimated from the solution to Fick's 2nd law in one dimension.(D. Y. W. Yu, et al., 2006) Equation 3 of this reference can be differentiated and introduced into Fick's first law to give

$$\frac{\partial n}{\partial t} = ADc_0 \sum_{m=0}^{\infty} \left\{ \frac{2}{R} \exp\left[-\left(m + {}^1/_2\right)^2 \frac{\pi^2 D}{R^2} t \right] \right\}, \quad (C.1)$$

where n is the amount of substance, t is the time, A is the surface area, D is the lithium diffusion coefficient, c_0 is the initial lithium concentration in $LiFePO_4$ and R is the average particle radius. Equation [1] can be integrated to give n:

$$n = \frac{2ARc_0}{\pi^2} \sum_{m=0}^{\infty} \left\{ \left(m + {}^1/_2\right)^{-2} \left[1 - \exp\left(-\left(m + {}^1/_2\right)^2 \frac{\pi^2 D}{R^2} t \right) \right] \right\}. \quad (C.2)$$

And since the mol fraction of reacted product α is related to n via

$$\alpha = \frac{n}{c_0 AR}, \quad (C.3)$$

equation (B.2) simplifies to

$$\alpha = \frac{8}{\pi^2} \sum_{m=0}^{\infty} \left\{ (2m+1)^{-2} \left[1 - \exp\left(-\left(m + {}^1/_2\right)^2 \frac{\pi^2 D}{R^2} t \right) \right] \right\}. \quad (C.4)$$

Time-resolved x-ray diffraction data (Figure 2.4 b) was used for estimating D, fitting to equation (C.4) with the summation expanded to the 7th term.

B.2 Rate performance

Figure B.2 shows the rate performance of the oxidized material after the 50th cycle. Charges were performed at a rate of C/5. As can be seen, the material exhibits a rate performance that is common for $LiFePO_4$.

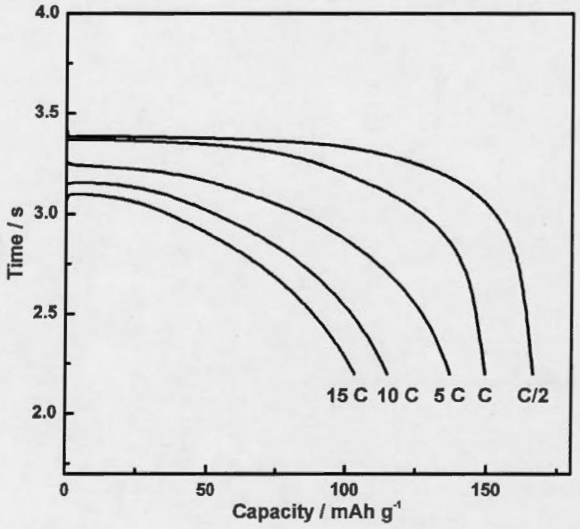

Figure B.2 Discharge curves at different rates of the same battery presented in Figure 2.4.

APPENDIX C

SUPPORTING INFORMATION TO STRUCTURAL TRANSFORMATION OF $LiFePO_4$ DURING ULTRAFAST CHARGING

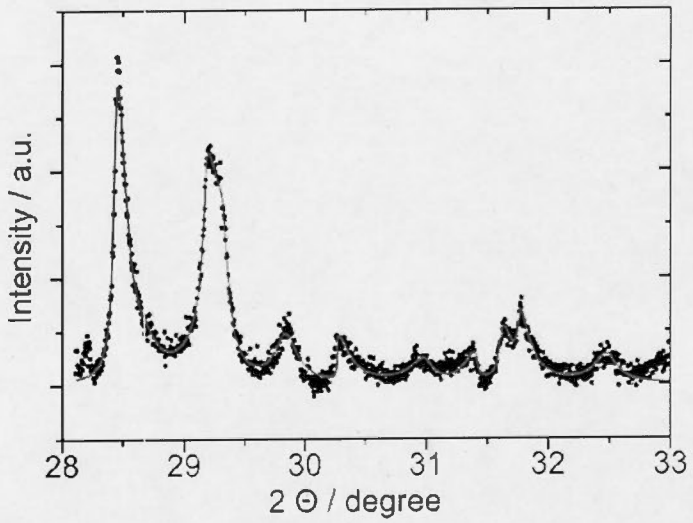

Figure C.1 Typical fit (green line) to a diffractogram during the phase transition. The asymmetries of all peaks could be well fitted.

APPENDIX D

SUPPORTING INFORMATION TO ATOMISTIC MODELING OF SITE EXCHANGE DEFECTS IN LITHIUM IRON PHOSPHATE AND IRON PHOSPHATE

Table D.1 Mechanical properties, dielectric constants and heat capacities of $LiFePO_4$ and $FePO_4$ from atomistic calculations.

	$LiFePO_4$	$FePO_4$
Bulk moduli		
K_{Reuss}	117.3 GPa	63.9 GPa
K_{Voigt}	118.0 GPa	64.4 GPa
K_{Hill}	117.6 GPa	64.1 GPa
Shear moduli		
G_{Reuss}	56.8 GPa	36.9 GPa
G_{Voigt}	59.6 GPa	42.5 GPa
G_{Hill}	58.2 GPa	39.7 GPa
Youngs moduli		
E_a	142.9 GPa	111.0 GPa
E_b	179.6 GPa	179.5 GPa
E_c	151.0 GPa	97.2 GPa
Dielectric constants		
ε_0	19.8	17.5
ε_{hf}	3.77	5.19
Heat capacities		
$C_{p,\,100K}$	43.5 J/(K.mol)	35.1 J/(K.mol)
$C_{p,\,200K}$	87.8 J/(K.mol)	70.3 J/(K.mol)
$C_{p,\,300K}$	113.6 J/(K.mol)	92.5 J/(K.mol)
$C_{p,\,400K}$	129.7 J/(K.mol)	107.1 J/(K.mol)
$C_{p,\,500K}$	140.2 J/(K.mol)	116.8 J/(K.mol)
$C_{p,\,600K}$	147.1 J/(K.mol)	123.3 J/(K.mol)

To assess the transferability of the set of potentials, we calculated the optimized crystal structures of γ-Li_3PO_4 and the Nasicon analogue $Li_3Fe_2(PO_4)_3$:

Table D.2 Comparison of calculated and experimental crystal structure parameters of γ-Li_3PO_4.

Li_3PO_4	Experimental(Zemann, 1960)	Calculated	Rel. error / %
a / Å	6.12	6.03	1.5
b / Å	10.53	10.27	2.5
c / Å	4.93	4.87	1.2
$Li_3Fe_2(PO_4)_3$	Experimental(Masquelier, Wurm, Rodríguez-Carvajal, Gaubicher, & Nazar, 2000)	Calculated	Rel. error / %
a / Å	8.32	8.20	1.4
c / Å	22.46	21.63	3.7

It can be seen, that the potentials are valid with restrictions also for other compounds of the lithium and iron phosphate system. Note: This potential set should only be used for structures where oxygen is covalently bonded to phosphor in phosphate groups.

For calculations of defect correlation, we determined a quantity of charge localization on the unit cell scale. This quantity was determined from the relaxed structures by integrating all charges within the volume of one unit cell. This volume was then moved across the complete super cell by ¼ unit cell steps in each crystallographic direction to obtain an average of charge localization in the super cell.

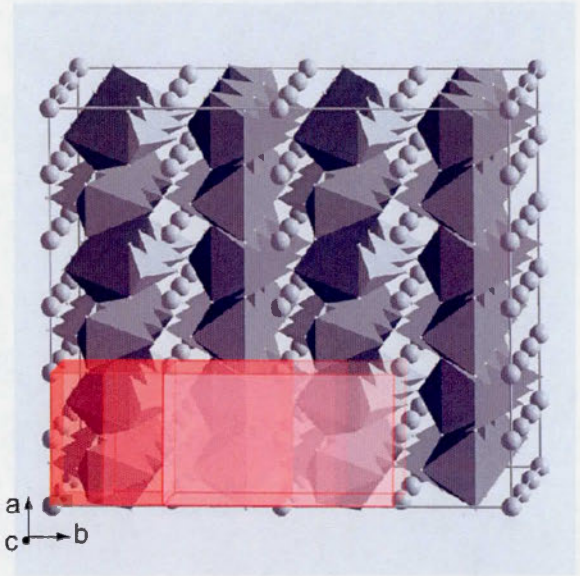

Figure D.1 Illustration of iterative charge integration to obtain the value termed average localized charge. The red cuboids correspond to the volume of one unit cell each. The left cuboid determines the integration boundaries for the first integration step. The other cuboids illustrate the movement of the integration boundaries during the iterative integration over the whole super cell. An average of integrated charge per unit cell is then determined for the complete super cell.

APPENDIX E

ADDITIONAL *IN SITU* OBSERVATIONS OF THE OXIDATION OF $LiFePO_4$

Many additional experiments were conducted in the course of this doctoral program, not all of which were included in the publications. This appendix wants to summarize three *in situ* experiments that are of particular interest to the overall project.

E.1 *In situ* photometry by videography

As $LiFePO_4$ is delithiated and lithiated, its electronic structure changes, leading to a visible change in absorption.(Zaghib, Mauger, Goodenough, Gendron, & Julien, 2007) This can be observed by a darkening of the powder and is in theory measureable by diffuse reflectance UV/Vis spectroscopy. However, the absorption of visible light can also be estimated, using a stable light source and a household digital camera. Such data can be used to extract crude visible light absorption curves by converting the image into grayscale and reading the pixel values of the recorded sample. In fact, in biological sciences it is quite common to quantify light intensity using photographs or videos. Depending on the internal software, in particular the applied gamma function, the recorded grayscale value for one pixel may be more or less linearly correlated to the measured light intensity. If only a small variation over all possible grayscale values is of interest, the linear approximation becomes more valid.

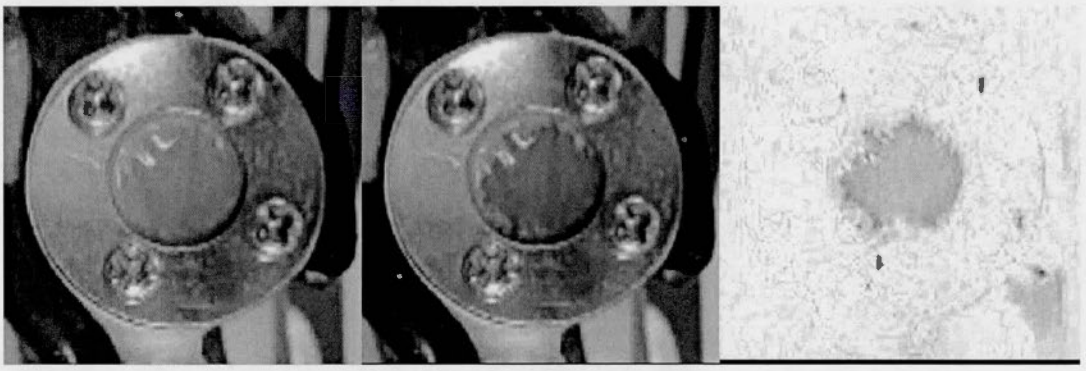

Figure E.1 Initial (left) and final (center) image of a video recording of the oxidation of a carbon free $LiFePO_4$ sample (within the steel ring under a Polyimide film). A slight change in coloration of the powder can be observed. The image on the right shows the inverted subtraction of the two images, with contrast enhancement. It is clear that the main color change can be observed in the sample. As such, it is likely due to changed absorption and not due to lighting fluctuation.

Such recordings were made of the oxidation of $LiFePO_4$ with the gaseous oxidant NO_2. The experiments were commonly performed as described for *in situ* XRD in chapter II, except the reaction progress was recorded with a conventional digital camera through the Kapton® film. Figure E.1 shows the initial and final state of a typical experiment, where a small change in absorption of the sample can be observed.

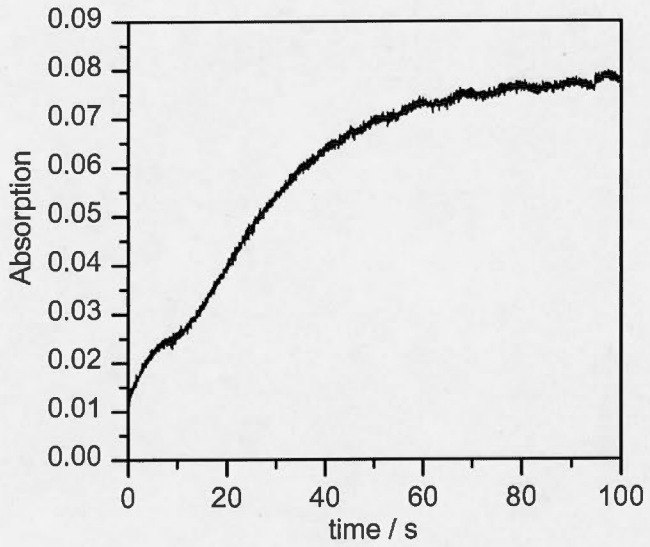

Figure E.2 Typical Absorption-Time data obtained from a video recording of the oxidation of $LiFePO_4$ with NO_2 gas.

Using picture analysis software, in this case the open source package ImageJ, (Schneider, Rasband, & Eliceiri, 2012) it is possible to analyze all frames of the video. From the intensity of the grayscale values, an absorption can be calculated, using a white reference point in the video and an average of the sample grayscale value. This technique provides a remarkably well resolved absorption-time plot (Figure E.2), at an acquisition rate of 30 Hz. From this data, it appears the reaction takes place in at least two steps. Taking the considerations of section 5.2 into account, the first step may correspond to the initial delithiation in solid solution, whereas the light absorption behavior changes upon nucleation of the second phase.

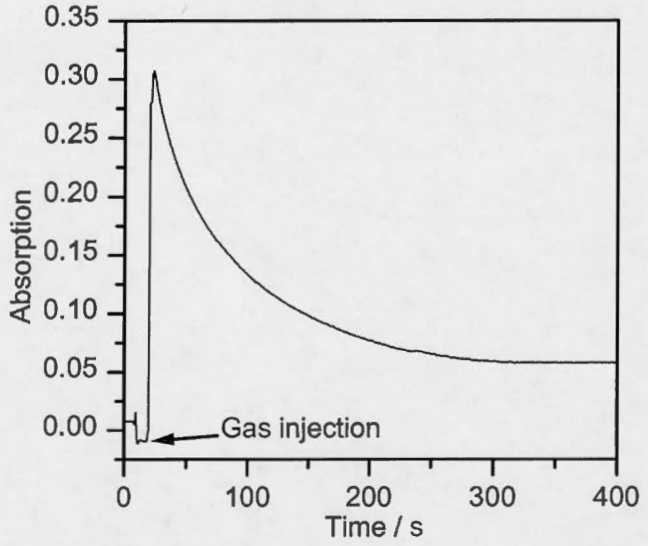

Figure E.3 Absorption-Time curve of *in situ* photometry at 430nm of consumption of NO_2 gas by oxidation of C-$LiFePO_4$ (solid state, see chapter II).

E.2 UV/Vis photometry of the oxidizing gas

Complementary to this video data, *in situ* UV/Vis absorption photometry of the oxidizing gas was also recorded, similar to the measurements presented in Chapter I. These experiments were performed in a cuvette with rubber septum at room temperature using an Ocean Optics fiber optics UV/Vis spectrometer. The $LiFePO_4$ sample was placed in the cuvette, following which the light absorption by NO_2 gas was recorded at a collection time of one second. After about 20 seconds, the oxidizing gas was injected through the septum.

In contrast to the video results, the reaction progress appears smoother. Considering that the non-homogenous features of the videography results are occurring on the second scale, it is, however, unclear, whether such features may get smoothed out by diffusion effects of the gas from the sample to the light path. Hence, this method did not provide additional information on the reaction mechanism, but it confirmed the observed reaction rates.

Finally, in a gas flow experiment, the gas concentration was monitored after exiting the reaction chamber. For this experiment, the sample was placed in PTFE tubing with two cotton stoppers. In order to increase the porosity of the sample and allow better contact between gas and active particles, sodium chloride as coarse grained non-reactive filler was added. At the exit of the tubing, a glass tube was connected, through which light absorption was monitored with an Ocean Optics fiber optics UV/Vis spectrometer. The gas flow, commonly a 2:3 volume mixture of NO_2 and N_2, was controlled by a syringe pump. An absorption difference was determined by recording light intensity in two runs: the first with a pristine $LiFePO_4$/NaCl sample, the second with the already oxidized, hence non-reacting, sample. In doing so, matrix effects could be eliminated.

Similar to the videography data, the obtained curve, which is essentially a measure of the reaction rate, shows clearly two separate steps. The initial separated peak has been observed consistently and is robust to small possible errors in the injection time. This early part of the reaction is more difficult to follow by the static method in the cuvette, as the gas injection requires few seconds, during which the gas concentration is equilibrated over the whole cuvette. In contrast to previous considerations (section 5.4), if this initial peak rate is in fact related to a single phase reaction, this initial step seems to progress faster, than the following two-phase reaction.

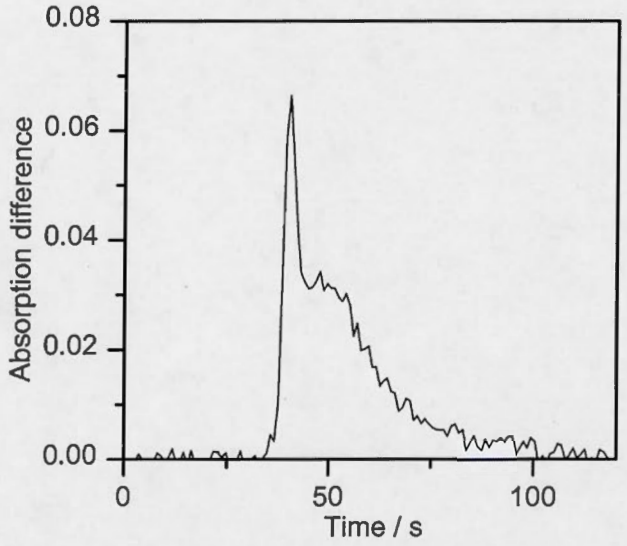

Figure E.4 Plot of the difference in absorption of a blank run and a sample run. The observed separation of two peaks is robust to an estimated error in the injection time of ± 2 seconds.

E.3 Summary

Three different UV/Visible absorption techniques have been applied to study the delithiation of $LiFePO_4$ with oxidizing gases *in situ*. These techniques suggest a reaction progress in two distinct steps, which is in agreement with a delithiation mechanism in solid solution, followed by a two-phase reaction, as proposed in sections 5.4 and 5.5. Even though it is difficult to distinguish between an early fast reaction mechanism and an initial absorption of NO_2 gas on the particle surface, the observation of two steps in both the optical properties of the material and in the concentration of the gas increases the confidence in these results.

APPENDIX F

PROGRAMS AND SCRIPTS

All programs and functions presented in this appendix were written by the author of this thesis and contributed to the presented data in the earlier chapters. Some functions and programs were adapted dynamically to changing requirements of the data. As such the code below may not be identical to the one used in deriving the data of the earlier chapters.

F.1 Octave: Diffractograms from tiff 2D detector data

This function was used to obtain intensity-diffraction angle plots for series of tiff detector images. It uses a series of tiff images and detector positioning input to produce an intensity matrix, whereas the columns correspond to different equally spaced angles, and the rows correspond to different images. Since each diffractogram data point is integrated from a different number of pixels, each point is normalized by the number of contributing pixels.

```
# This function calculates a powder diffractogram-time map from tiff
images of an area detector from its geometrical location.
# It requires the following format:
# timemap (det2th, detdis, detw, deth, pixw, pixh, deta, ares,
Filepath, startindex, nfile)
#     det2th: 2theta angle of the center of the detector
#     detdis: distance of the detector to the sample in length units
(e.g. cm)
#     dety: shift of detector from the plane described by the sample
and the incident X-ray beam in length units
#     detw: width of the detector in length units (e.g. 3.35 for
Pilatus 100k)
#     deth: height of the detector in length units (e.g. 8.38)
#     pixw: pixel width in length units (e.g. 0.0172)
```

```
#     pixh: pixel height in length units (e.g. 0.0172)
#     deta: angle between detector surface and detector-sample vector
#     ares: required angular resolution of diffractogram (below a
threshhold resolution intrinsic to the setup and depending on the
respective geometry, the lowest angles may become n/A)
#     Filepath: path to the image files without index number or tif
extension
#     startindex: first index number
#     nfile: number of tiff files
#
# All angles are required in degrees and all distances are required
to have the same unit. The unit should not be included in the
argument.
# The output is of the form of a matrix with the angle increasing
along the row and the time increasing along the column.
#
# Software written by Christian Kuss, Universite du Quebec a
Montreal.

function value = timemap (det2th, detdis, dety, detw, deth, pixw,
pixh, deta, ares, Filepath, startindex, nfile)
# Transform angles to radians
 det2th = det2th*pi/180
 deta = deta*pi/180
 ares = ares*pi/180

# Calculate detector position
 detx = detdis*sin(det2th)
 detz = detdis*cos(det2th)
 detlowedgez = detz+sin(deta-(pi/2-det2th))*deth/2
 detlowedgex = detx-cos(deta-(pi/2-det2th))*deth/2
 dethighedgez = detz-sin(deta-(pi/2-det2th))*deth/2
 dethighedgex = detx+cos(deta-(pi/2-det2th))*deth/2

# Calculate angle range and detector dimensions in pixels
 max2th                                                          =
acos(dethighedgez/(dethighedgex^2+(detw/2)^2+dethighedgez^2)^0.5)
 min2th = acos(detlowedgez/(detlowedgex^2+detlowedgez^2)^0.5)
 nangles = floor((max2th-min2th)/ares)
 detpixw = round(detw/pixw)
 detpixh = round(deth/pixh)

# Calculate 2theta matrix of detector and 3D matrix of valid pixels
per angular value
 pixx = (repmat(1:detpixh,detpixw,1)+0.5)*pixh-deth/2;
 pixy   =   (repmat(reshape(1:detpixw,detpixw,1),1,detpixh)+0.5)*pixw-
detw/2+dety;
 pixz = detz-sin(deta-(pi/2-det2th))*pixx;
 pixx = detx+cos(deta-(pi/2-det2th))*pixx;
 pix2th = acos(pixz./(pixx.^2+pixy.^2+pixz.^2).^0.5);
 for i = 1:nangles
```

```
  boleanangle(:,:,i)        =        (min2th+(i-1)*ares)<pix2th        &
pix2th<(min2th+i*ares);
 endfor

# open files
 for file = 1:nfile

  orig = tiffread2(strcat(Filepath, sprintf("%05d",file+startindex-
1), ".tif")) ;
  dataorig = double(orig.data);

# Integrate intensities
  for i = 1:nangles
   anglevalues = dataorig.*boleanangle(:,:,i);
   value(file,i) = sum(anglevalues(:))/sum(sum(boleanangle(:,:,i)));
  endfor
 printf(cstrcat(sprintf("%03d",file), " |"))
 endfor

# Display result
 disp('')
 disp('max angle')
 disp(max2th*180/pi)
 disp('min angle')
 disp(min2th*180/pi)
 imshow(uint16(value))

endfunction
```

F.2 Matlab: Fitting functions

In order to fit split pseudo voigt peak profiles to these diffractograms the following functions were employed. The asymmetric pseudo voigt function apsvgt() describes the peak shape. The fitting function apvfit() fits between three and four peaks to the diffractogram, using the cell parameters, peak heights, two widths per peak and the lorentz fractions as fitting parameters. The matlab program fitting.m is a routine that uses the above two functions to fit initial guesses to a series of diffractograms, and extract the fitted parameters, and their confidence intervals. Finally, in order to obtain the average strain, apvmean() uses peak position, shape and widths to calculate the mean of a hypothetical distribution of the same shape. Fitting.m and apvmean() are only examples, and need adjustment from one sample to the next.

F.2.1 Asymmetric Pseudo Voigt function

```
function res = apsvgt(k,x)
 if x(1) > round(k(4))
  x1 = [];
  x2 = x;
 elseif x(length(x)) < round(k(4))
  x1 = x;
  x2 = [];
 else
  x1 = [x(1):round(k(4))];
  x2 = [round(k(4))+1:x(length(x))];
 end
 res = psvgt([k(1),k(2),k(4)],x1);
 res(length(x1)+1:length(x2)+length(x1)) =
psvgt([k(1),k(3),k(4)],x2);
end

% Pseudo-Voigt function
 function res = psvgt(k,x)
  res = k(1)*Lorentz(k(2:3),x)+(1-k(1))*Gauss(k(2:3),x);
 end


% Lorentz function
  function res = Lorentz(k,x)
   wk = k(1)/2;
   res = wk.^2./(wk^2+(x-k(2)).^2);
  end

% Gauss function
  function res = Gauss(k,x)
   sigma = 0.5*k(1)*sqrt(pi/log(2));
   res = exp(-pi*(x-k(2)).^2/sigma^2);
  end
```

F.2.2 Fitting function

```
function res = apvfit(k)
%k has form [height,lorentz fraction,width left, width right, cell
param.
%a,...]
%function works only for three to four peaks

%fetch time step and raw data
 global signal;                %raw data
 global xrange;
 global time;                  %time step
 global hkl;                   %h,k,l for peaks
```

```
global anglerange;              %[start value,step] in degrees
global weight;
ffit = 0;

%extract peak position from cell parameters

abc = [k(5),k(10),k(15)].^2;
for m = 1:size(hkl,1)
   k(5*m) = sqrt(1./(sum(hkl(m,:)./abc)));
   k(5*m) = asin(1.2398/2/k(5*m));
   k(5*m) = (k(5*m)*360/pi-anglerange(1))/anglerange(2);
end


%calculate fit
for l = 1:length(k)/5
 ffit = ffit + k(l*5-4)*apsvgt(k(l*5-3:l*5),[1:size(signal,2)]);
end

res = signal(time,:) - ffit;

%weight by intensity
%for l = 1:size(xrange,1)
%    x = xrange(l,1):xrange(l,2);
res = res.*sqrt(weight(time,:));
%end

%penalty for going beyond bounds
for l = 1:length(k)/5
 res = res+ones(1,size(signal,2))*(10E6*min(k(l*5-
3),0).^2+10E6*max(k(l*5-3)-1,0).^2+10E6*min(k(l*5)-
xrange(l,1),0).^2+10E6*max(k(l*5)-xrange(l,2),0).^2);
end

end
```

F.2.3 Fitting routine

```
for time = 1:110
    k0 = lfp2(time,:,:);
    [temp,resnorm,resid(time,:),exitflag,output,lambda,jac]          =
lsqnonlin(@apvfit,k0(:),[],[],opt1);
    simullfp(time,:)                    =                signal(time,:)-
resid(time,:)./sqrt(weight(time,:));
    CI = nlparci(temp,resid(time,:),'jacobian',jac);
    disp(['timestep ', int2str(time), ' exit ', int2str(exitflag)])
    lfp4(time,1:5,:) = reshape(temp,5,3);
    lfp4(time,6,:) = CI([5,10,15]);
```

```
    lfp4(time,7,:) = CI([20,25,30]);
end
```

F.2.4 Function to obtain peak mean from peak shape

```
%function to get mean of distribution (in degrees), numerical
approach
function res = apsvgtmean(k)
 normapsvgt     =     k(1)*apsvgt(k(2:5),[-5621:12378])./apsvgtint(k);
%this line needs to be adjusted for the detector range (-5621:12378)
 xp                =                [0.002:0.005:89.997].*normapsvgt;
%this   line   needs   to   be   adjusted   for   the   detector   range
(0.002:0.005:89.997)
 res = sum(xp)*0.005;
end

function res = apsvgtint(k)
 sigma1 = 0.5*abs(k(3))*sqrt(pi/log(2));
 sigma2 = 0.5*abs(k(4))*sqrt(pi/log(2));
 res        =        k(1)/2*(k(2)*(pi*abs(k(3))/2+pi*abs(k(4))/2)+(1-
k(2))*(sigma1+sigma2)).*0.005;
end
```

F.3 Just Basic: Creating defects, running gulp and analyzing output

This program was written in "Just Basic" to write GULP input files for supercell defect calculations, place defects randomly, and extract thermodynamic defect data from the output files.

```
print  "----------------------------------------------------------------
----------------------------------------------------------------
----------------------------------------------------------------
-------------------------"
print "This program produces LiFePO4 Super Cells and random site-
exchange defects therein, creates the appropriate shell and batch
jobs, runs them and calculates defect internal energies, defect free
energies and defect entropies."
print  "----------------------------------------------------------------
----------------------------------------------------------------
----------------------------------------------------------------
-------------------------"
print ""
[ModeSelection]
print "What do you want to do?"
print "1 = Write input files, run and evaluate output"
```

```
print "2 = Write input files and batch file"
print "3 = Write only input files"
print "4 = Calculate thermodynamics from output files"
print "5 = quit"
input Modesel

select case Modesel
 Case 1,2,3, 4
  Goto [SCinput]
 Case 5
  end
 Case else
  print "No valid selection! (Put in 1, 2, 3, 4 or 5)"
  Goto [ModeSelection]
End select

'Input size of unit cell"
[SCinput]
print "Do you want to calculate defects for LFP, FP or both."
input "Type 'LFP', 'FP' or 'both' :"; LFPFP$

let LFPFP$ = TRIM$(LFPFP$)

While instr("LFPFPboth", LFPFP$) = 0
   input "Type 'LFP', 'FP' or 'both' :"; LFPFP$
Wend

While sizea < 1
 print "How many unit cells in a direction?"
 input sizea
Wend
While sizeb < 1
 print "How many unit cells in b direction?"
 input sizeb
Wend
While sizec < 1
 print "How many unit cells in c direction?"
 input sizec
Wend

if Modesel <> 4 then
 'Input number of defects"
 print "How many site-exchange defects?"
 input defectNumber

 While defectNumber > sizea*sizeb*sizec*4
  print "Too many defects for the size of the Super Cell. Maximum
number of defects:" + STR$(sizea*sizeb*sizec*4)
  print "How many site-exchange defects?"
  input defectNumber
 Wend
```

```
 While defectNumber < 1
  print "Cell has to have at least one defect."
  print "How many site-exchange defects?"
  input defectNumber
 Wend

 While defectNumber <> int(defectNumber)
  print "Number of defects has to be an integer."
  print "How many site-exchange defects?"
  input defectNumber
 Wend

end if

print "How many random defect configurations?"
input defectCalculations

While defectCalculations <> int(defectCalculations)
 print "Number of calculations has to be an integer."
 print "How many site-exchange defects?"
 input defectNumber
Wend

if Modesel = 4 then [Evaluation]

[UnitCellDefine]
'define LiFePO4 and FePO4 unit cell
dim LiUnitCell(4,3)
dim FeUnitCell(4,3)
dim PUnitCell(4,3)
dim OUnitCell(16,3)

let LFPCellParametera = 10.362201
let LFPCellParameterb = 5.983247
let LFPCellParameterc = 4.680449

let FPCellParametera = 10.3378
let FPCellParameterb = 6.0112
let FPCellParameterc = 4.6950

let FeUnitCell(    1     ,     1    )=    0.78223
let FeUnitCell(    2     ,     1    )=    0.211238
let FeUnitCell(    3     ,     1    )=    0.282229
let FeUnitCell(    4     ,     1    )=    0.711237
let LiUnitCell(    1     ,     1    )=    0.996733
let LiUnitCell(    2     ,     1    )=    0.996733
let LiUnitCell(    3     ,     1    )=    0.496731
let LiUnitCell(    4     ,     1    )=    0.496731
let OUnitCell(    1     ,     1    )=    0.88927
let OUnitCell(    2     ,     1    )=    0.6042
let OUnitCell(    3     ,     1    )=    0.389273
let OUnitCell(    4     ,     1    )=    0.104196
```

```
let OUnitCell(    5     ,     1    )=    0.957278
let OUnitCell(    6     ,     1    )=    0.036191
let OUnitCell(    7     ,     1    )=    0.457277
let OUnitCell(    8     ,     1    )=    0.536189
let OUnitCell(    9     ,     1    )=    0.830554
let OUnitCell(    10     ,     1    )=    0.662914
let OUnitCell(    11     ,     1    )=    0.330552
let OUnitCell(    12     ,     1    )=    0.162915
let OUnitCell(    13     ,     1    )=    0.162915
let OUnitCell(    14     ,     1    )=    0.330552
let OUnitCell(    15     ,     1    )=    0.662914
let OUnitCell(    16     ,     1    )=    0.830554
let PUnitCell(    1     ,     1    )=    0.398618
let PUnitCell(    2     ,     1    )=    0.59485
let PUnitCell(    3     ,     1    )=    0.898618
let PUnitCell(    4     ,     1    )=    0.09485
let FeUnitCell(    1     ,     2    )=    0.25
let FeUnitCell(    2     ,     2    )=    0.75
let FeUnitCell(    3     ,     2    )=    0.25
let FeUnitCell(    4     ,     2    )=    0.75
let LiUnitCell(    1     ,     2    )=    0.999999
let LiUnitCell(    2     ,     2    )=    0.500001
let LiUnitCell(    3     ,     2    )=    0.500001
let LiUnitCell(    4     ,     2    )=    0.999999
let OUnitCell(    1     ,     2    )=    0.75
let OUnitCell(    2     ,     2    )=    0.25
let OUnitCell(    3     ,     2    )=    0.75
let OUnitCell(    4     ,     2    )=    0.25
let OUnitCell(    5     ,     2    )=    0.25
let OUnitCell(    6     ,     2    )=    0.75
let OUnitCell(    7     ,     2    )=    0.25
let OUnitCell(    8     ,     2    )=    0.75
let OUnitCell(    9     ,     2    )=    0.949938
let OUnitCell(    10     ,     2    )=    0.050061
let OUnitCell(    11     ,     2    )=    0.550062
let OUnitCell(    12     ,     2    )=    0.050061
let OUnitCell(    13     ,     2    )=    0.449939
let OUnitCell(    14     ,     2    )=    0.949938
let OUnitCell(    15     ,     2    )=    0.449939
let OUnitCell(    16     ,     2    )=    0.550062
let PUnitCell(    1     ,     2    )=    0.75
let PUnitCell(    2     ,     2    )=    0.25
let PUnitCell(    3     ,     2    )=    0.75
let PUnitCell(    4     ,     2    )=    0.25
let FeUnitCell(    1     ,     3    )=    0.5261
let FeUnitCell(    2     ,     3    )=    0.479718
let FeUnitCell(    3     ,     3    )=    0.979718
let FeUnitCell(    4     ,     3    )=    0.026088
let LiUnitCell(    1     ,     3    )=    0.002909
let LiUnitCell(    2     ,     3    )=    0.002909
let LiUnitCell(    3     ,     3    )=    0.5029
let LiUnitCell(    4     ,     3    )=    0.5029
```

```
let OUnitCell(    1     ,     3    )=    0.26071
let OUnitCell(    2     ,     3    )=    0.760706
let OUnitCell(    3     ,     3    )=    0.245103
let OUnitCell(    4     ,     3    )=    0.745102
let OUnitCell(    5     ,     3    )=    0.304324
let OUnitCell(    6     ,     3    )=    0.701482
let OUnitCell(    7     ,     3    )=    0.201472
let OUnitCell(    8     ,     3    )=    0.804327
let OUnitCell(    9     ,     3    )=    0.728045
let OUnitCell(    10     ,     3    )=    0.228043
let OUnitCell(    11     ,     3    )=    0.777767
let OUnitCell(    12     ,     3    )=    0.277768
let OUnitCell(    13     ,     3    )=    0.277768
let OUnitCell(    14     ,     3    )=    0.777767
let OUnitCell(    15     ,     3    )=    0.228043
let OUnitCell(    16     ,     3    )=    0.728045
let PUnitCell(    1     ,     3    )=    0.923635
let PUnitCell(    2     ,     3    )=    0.082174
let PUnitCell(    3     ,     3    )=    0.582176
let PUnitCell(    4     ,     3    )=    0.423636

[SuperCellDefine]
'dimension Super Cell arrays
dim LiSuperCell(4*sizea*sizeb*sizec,3)
dim FeSuperCell(4*sizea*sizeb*sizec,3)
dim PSuperCell(4*sizea*sizeb*sizec,3)
dim OSuperCell(16*sizea*sizeb*sizec,3)

'Create Bulk LFP Super Cell
For a=0 to sizea-1
 For b=0 to sizeb-1
  For c=0 to sizec-1
   For i=1 to 4

LiSuperCell(i+4*sizeb*sizec*a+4*sizec*b+4*c,1)=(LiUnitCell(i,1)+a)/s
izea

LiSuperCell(i+4*sizeb*sizec*a+4*sizec*b+4*c,2)=(LiUnitCell(i,2)+b)/s
izeb

LiSuperCell(i+4*sizeb*sizec*a+4*sizec*b+4*c,3)=(LiUnitCell(i,3)+c)/s
izec
    next i
   For i=1 to 4

FeSuperCell(i+4*sizeb*sizec*a+4*sizec*b+4*c,1)=(FeUnitCell(i,1)+a)/s
izea

FeSuperCell(i+4*sizeb*sizec*a+4*sizec*b+4*c,2)=(FeUnitCell(i,2)+b)/s
izeb
```

```
FeSuperCell(i+4*sizeb*sizec*a+4*sizec*b+4*c,3)=(FeUnitCell(i,3)+c)/s
izec
    next i
   For i=1 to 4

PSuperCell(i+4*sizeb*sizec*a+4*sizec*b+4*c,1)=(PUnitCell(i,1)+a)/siz
ea

PSuperCell(i+4*sizeb*sizec*a+4*sizec*b+4*c,2)=(PUnitCell(i,2)+b)/siz
eb

PSuperCell(i+4*sizeb*sizec*a+4*sizec*b+4*c,3)=(PUnitCell(i,3)+c)/siz
ec
    next i
   For i=1 to 16

OSuperCell(i+16*sizeb*sizec*a+16*sizec*b+16*c,1)=(OUnitCell(i,1)+a)/
sizea

OSuperCell(i+16*sizeb*sizec*a+16*sizec*b+16*c,2)=(OUnitCell(i,2)+b)/
sizeb

OSuperCell(i+16*sizeb*sizec*a+16*sizec*b+16*c,3)=(OUnitCell(i,3)+c)/
sizec
    next i
   next c
  next b
 next a

if LFPFP$ = "FP" then [FPBulkWrite]
'---------------------------------------LFP-----------------------
------------
[LFPBulkWrite]
'write Bulk input
open "C:\Program Files (x86)\gulp\Exe\SC\LFPSC" + STR$(sizea) +
STR$(sizeb) + STR$(sizec) + "-" +
STR$(int(100*defectNumber/sizea/sizeb/sizec/4)) + "pc_bulk.gin" for
output as #Gin

print #Gin, "opti conp phonon"
print #Gin, "temperature 298"

print #Gin, ""
print #Gin, "name LFP-bulk"
print #Gin, "cell"
print #Gin, STR$(LFPCellParametera*sizea); " ";
STR$(LFPCellParameterb*sizeb); " "; STR$(LFPCellParameterc*sizec); "
90 90 90"
print #Gin, ""

print #Gin, "fractional"
```

```
For a=0 to sizea-1
 For b=0 to sizeb-1
  For c=0 to sizec-1
   For i=1 to 4
    print            #Gin,            "Li1            core            ";
STR$(LiSuperCell(i+4*sizeb*sizec*a+4*sizec*b+4*c,1));       "       ";
STR$(LiSuperCell(i+4*sizeb*sizec*a+4*sizec*b+4*c,2));       "       ";
STR$(LiSuperCell(i+4*sizeb*sizec*a+4*sizec*b+4*c,3))
    next i
   For i=1 to 4
    print            #Gin,            "Fe1            core            ";
STR$(FeSuperCell(i+4*sizeb*sizec*a+4*sizec*b+4*c,1));       "       ";
STR$(FeSuperCell(i+4*sizeb*sizec*a+4*sizec*b+4*c,2));       "       ";
STR$(FeSuperCell(i+4*sizeb*sizec*a+4*sizec*b+4*c,3))
    next i
   For i=1 to 4
    print            #Gin,            "P1             core            ";
STR$(PSuperCell(i+4*sizeb*sizec*a+4*sizec*b+4*c,1));       "       ";
STR$(PSuperCell(i+4*sizeb*sizec*a+4*sizec*b+4*c,2));       "       ";
STR$(PSuperCell(i+4*sizeb*sizec*a+4*sizec*b+4*c,3))
    next i
   For i=1 to 16
    print            #Gin,            "O1             core            ";
STR$(OSuperCell(i+16*sizeb*sizec*a+16*sizec*b+16*c,1));      "      ";
STR$(OSuperCell(i+16*sizeb*sizec*a+16*sizec*b+16*c,2));      "      ";
STR$(OSuperCell(i+16*sizeb*sizec*a+16*sizec*b+16*c,3))
    print            #Gin,            "O1             shel            ";
STR$(OSuperCell(i+16*sizeb*sizec*a+16*sizec*b+16*c,1));      "      ";
STR$(OSuperCell(i+16*sizeb*sizec*a+16*sizec*b+16*c,2));      "      ";
STR$(OSuperCell(i+16*sizeb*sizec*a+16*sizec*b+16*c,3))
    next i
   next c
  next b
 next a

print #Gin, "space"
print #Gin, "P 1"
print #Gin, ""
print #Gin, "shrink   2"
print #Gin, "species   6"
print #Gin, "Li1    core    1.000000"
print #Gin, "Fe1    core    2.000000"
print #Gin, "Fe2    core    3.000000"
print #Gin, "P1     core    4.970800"
print #Gin, "O1     shel   -2.894200"
print #Gin, "O1     core    0.901500"
print #Gin, "buck"
print  #Gin,  "Li      core  O       shel   381.524400        0.304910
0.000000      0.00  10.00"
print #Gin, "buck"
```

```
print #Gin, "Fe1     core O        shel   13207.0079        0.222450
0.000000      0.00  10.00"
print #Gin, "buck"
print #Gin, "Fe2     core O        shel   2111.96710        0.289410
0.000000      0.00  10.00"
print #Gin, "buck"
print #Gin, "P       core O        shel   1028.97410        0.335300
0.000000      0.00  10.00"
print #Gin, "buck"
print #Gin, "O       shel O        shel   39.7594000        0.477130
53.20373      0.00  10.00"
print #Gin, "spring"
print #Gin, "O      67.356400"

close #Gin

print "Done writing LFP bulk file."

'Create defect Files
[LFPDefectWrite]

For NumberDefectCalc=1 to defectCalculations

 dim M1(defectNumber)
 dim M2(defectNumber)
 dim ReadM1(defectNumber,3)
 dim ReadM2(defectNumber,3)
 let repetition = 0

 For DefectCount=1 to defectNumber
  [LFPSetM1M2]
  let repetition = 0
  M1(DefectCount) = int(RND(1)*4*sizea*sizeb*sizec+1)
  M2(DefectCount) = int(RND(1)*4*sizea*sizeb*sizec+1)
  If DefectCount > 1 then
   For k=1 to DefectCount-1
    if M1(DefectCount) = M1(k) then let repetition = 1
    if M2(DefectCount) = M2(k) then let repetition = 1
    next k
  End if
  if repetition = 1 then [LFPSetM1M2]

  'Read M1 and M2
  ReadM1(DefectCount,1) = LiSuperCell(M1(DefectCount),1)
  ReadM1(DefectCount,2) = LiSuperCell(M1(DefectCount),2)
  ReadM1(DefectCount,3) = LiSuperCell(M1(DefectCount),3)
  ReadM2(DefectCount,1) = FeSuperCell(M2(DefectCount),1)
  ReadM2(DefectCount,2) = FeSuperCell(M2(DefectCount),2)
  ReadM2(DefectCount,3) = FeSuperCell(M2(DefectCount),3)

  'Exchange M1 and M2
  let LiSuperCell(M1(DefectCount),1) = ReadM2(DefectCount,1)
```

```
  let LiSuperCell(M1(DefectCount),2) = ReadM2(DefectCount,2)
  let LiSuperCell(M1(DefectCount),3) = ReadM2(DefectCount,3)
  let FeSuperCell(M2(DefectCount),1) = ReadM1(DefectCount,1)
  let FeSuperCell(M2(DefectCount),2) = ReadM1(DefectCount,2)
  let FeSuperCell(M2(DefectCount),3) = ReadM1(DefectCount,3)

  next DefectCount

 open "C:\Program Files (x86)\gulp\Exe\SC\LFPSC" + STR$(sizea) +
STR$(sizeb) + STR$(sizec) + "-" +
STR$(int(100*defectNumber/sizea/sizeb/sizec/4)) + "pc_defect" +
STR$(NumberDefectCalc) + ".gin" for output as #Gin

 print #Gin, "opti conp phonon"
 print #Gin, "temperature 298"

 print #Gin, ""
 print #Gin, "name LFP-defect" + STR$(NumberDefectCalc)
 print #Gin, "cell"
 print #Gin, STR$(LFPCellParametera*sizea); " ";
STR$(LFPCellParameterb*sizeb); " "; STR$(LFPCellParameterc*sizec); "
90 90 90"
 print #Gin, ""

 print #Gin, "fractional"

 For a=0 to sizea-1
  For b=0 to sizeb-1
   For c=0 to sizec-1
    For i=1 to 4
     print #Gin, "Li1 core ";
STR$(LiSuperCell(i+4*sizeb*sizec*a+4*sizec*b+4*c,1)); " ";
STR$(LiSuperCell(i+4*sizeb*sizec*a+4*sizec*b+4*c,2)); " ";
STR$(LiSuperCell(i+4*sizeb*sizec*a+4*sizec*b+4*c,3))
     next i
    For i=1 to 4
     print #Gin, "Fe1 core ";
STR$(FeSuperCell(i+4*sizeb*sizec*a+4*sizec*b+4*c,1)); " ";
STR$(FeSuperCell(i+4*sizeb*sizec*a+4*sizec*b+4*c,2)); " ";
STR$(FeSuperCell(i+4*sizeb*sizec*a+4*sizec*b+4*c,3))
     next i
    For i=1 to 4
     print #Gin, "P1 core ";
STR$(PSuperCell(i+4*sizeb*sizec*a+4*sizec*b+4*c,1)); " ";
STR$(PSuperCell(i+4*sizeb*sizec*a+4*sizec*b+4*c,2)); " ";
STR$(PSuperCell(i+4*sizeb*sizec*a+4*sizec*b+4*c,3))
     next i
    For i=1 to 16
     print #Gin, "O1 core ";
STR$(OSuperCell(i+16*sizeb*sizec*a+16*sizec*b+16*c,1)); " ";
STR$(OSuperCell(i+16*sizeb*sizec*a+16*sizec*b+16*c,2)); " ";
STR$(OSuperCell(i+16*sizeb*sizec*a+16*sizec*b+16*c,3))
```

```
    print            #Gin,           "O1            shel            ";
STR$(OSuperCell(i+16*sizeb*sizec*a+16*sizec*b+16*c,1));      "      ";
STR$(OSuperCell(i+16*sizeb*sizec*a+16*sizec*b+16*c,2));      "      ";
STR$(OSuperCell(i+16*sizeb*sizec*a+16*sizec*b+16*c,3))
     next i
    next c
   next b
  next a

 print #Gin, "space"
 print #Gin, "P 1"
 print #Gin, ""
 print #Gin, "shrink   2"
 print #Gin, "species   6"
 print #Gin, "Li1    core    1.000000"
 print #Gin, "Fe1    core    2.000000"
 print #Gin, "Fe2    core    3.000000"
 print #Gin, "P1     core    4.970800"
 print #Gin, "O1     shel   -2.894200"
 print #Gin, "O1     core    0.901500"
 print #Gin, "buck"
 print #Gin, "Li      core O       shel   381.524400        0.304910
0.000000      0.00  10.00"
 print #Gin, "buck"
 print #Gin, "Fe1     core O       shel   13207.0079        0.222450
0.000000      0.00  10.00"
 print #Gin, "buck"
 print #Gin, "Fe2     core O       shel   2111.96710        0.289410
0.000000      0.00  10.00"
 print #Gin, "buck"
 print #Gin, "P       core O       shel   1028.97410        0.335300
0.000000      0.00  10.00"
 print #Gin, "buck"
 print #Gin, "O       shel O       shel   39.7594000        0.477130
53.20373      0.00  10.00"
 print #Gin, "spring"
 print #Gin, "O      67.356400"

 close #Gin

 For DefectCount=1 to defectNumber

  let LiSuperCell(M1(DefectCount),1) = ReadM1(DefectCount,1)
  let LiSuperCell(M1(DefectCount),2) = ReadM1(DefectCount,2)
  let LiSuperCell(M1(DefectCount),3) = ReadM1(DefectCount,3)
  let FeSuperCell(M2(DefectCount),1) = ReadM2(DefectCount,1)
  let FeSuperCell(M2(DefectCount),2) = ReadM2(DefectCount,2)
  let FeSuperCell(M2(DefectCount),3) = ReadM2(DefectCount,3)

  next DefectCount
```

```
 print "Done writing LFP defect file #" + STR$(NumberDefectCalc) +
". (first defect M1=(" + left$(STR$(ReadM1(1,1)),6) + "," +
left$(STR$(ReadM1(1,2)),6) + "," + left$(STR$(ReadM1(1,3)),6) + ")
and M2=(" + left$(STR$(ReadM2(1,1)),6) + "," +
left$(STR$(ReadM2(1,2)),6) + "," + left$(STR$(ReadM2(1,3)),6) + ")."

 next NumberDefectCalc

if LFPFP$ = "LFP" then
 if Modesel = 3 then [ModeSelection]
end if

'Create Batch File
open "C:\Program Files (x86)\gulp\Exe\SC\LFPSC" + STR$(sizea) +
STR$(sizeb) + STR$(sizec) + "-" +
STR$(int(100*defectNumber/sizea/sizeb/sizec/4)) + "pc.bat" for
output as #Bat

print #Bat, "Pause"
print #Bat, ":: Batch file for running a " + STR$(sizea) +
STR$(sizeb) + STR$(sizec) + " Super Cell with " + STR$(defectNumber)
+ " inter-site exchange defects in " + STR$(defectCalculations) + "
calculations."
print #Bat, "cd C:/Program Files (x86)/gulp/Exe/"
print #Bat, chr$(34) + "gulp.exe" + chr$(34) + " < SC/LFPSC" +
STR$(sizea) + STR$(sizeb) + STR$(sizec) + "-" +
STR$(int(100*defectNumber/sizea/sizeb/sizec/4)) + "pc_bulk.gin >
SC/LFPSC" + STR$(sizea) + STR$(sizeb) + STR$(sizec) + "-" +
STR$(int(100*defectNumber/sizea/sizeb/sizec/4)) + "pc_bulk.gout"

For NumberDefectCalc=1 to defectCalculations

 print #Bat, chr$(34) + "gulp.exe" + chr$(34) + " < SC/LFPSC" +
STR$(sizea) + STR$(sizeb) + STR$(sizec) + "-" +
STR$(int(100*defectNumber/sizea/sizeb/sizec/4)) + "pc_defect" +
STR$(NumberDefectCalc) + ".gin > SC/LFPSC" + STR$(sizea) +
STR$(sizeb) + STR$(sizec) + "-" +
STR$(int(100*defectNumber/sizea/sizeb/sizec/4)) + "pc_defect" +
STR$(NumberDefectCalc) + ".gout"
 next NumberDefectCalc

print #Bat, "Pause"

close #Bat

print "Done writing batch file."

'Create Shell File
open "C:\Program Files (x86)\gulp\Exe\SC\LFPSC" + STR$(sizea) +
STR$(sizeb) + STR$(sizec) + "-" +
STR$(int(100*defectNumber/sizea/sizeb/sizec/4)) + "pc.sh" for output
as #Shell
```

```
print #Shell, "#!/bin/bash"
print #Shell, "# Shell file for running a " + STR$(sizea) +
STR$(sizeb) + STR$(sizec) + " Super Cell with " + STR$(defectNumber)
+ " inter-site exchange defects in " + STR$(defectCalculations) + "
calculations."
print #Shell, ""
print #Shell, "mpirun gulp < SC/LFPSC" + STR$(sizea) + STR$(sizeb) +
STR$(sizec) + "-" + STR$(int(100*defectNumber/sizea/sizeb/sizec/4))
+ "pc_bulk.gin > SC/LFPSC" + STR$(sizea) + STR$(sizeb) + STR$(sizec)
+    "-"    +    STR$(int(100*defectNumber/sizea/sizeb/sizec/4))    +
"pc_bulk.gout"

For NumberDefectCalc=1 to defectCalculations

 print #Shell, "mpirun gulp < SC/LFPSC" + STR$(sizea) + STR$(sizeb)
+            STR$(sizec)            +            "-"            +
STR$(int(100*defectNumber/sizea/sizeb/sizec/4))   +   "pc_defect"   +
STR$(NumberDefectCalc)   +   ".gin   >   SC/LFPSC"   +   STR$(sizea)   +
STR$(sizeb)        +        STR$(sizec)        +        "-"        +
STR$(int(100*defectNumber/sizea/sizeb/sizec/4))   +   "pc_defect"   +
STR$(NumberDefectCalc) + ".gout"
 next NumberDefectCalc

close #Shell

print "Done writing shell file."

if LFPFP$ = "LFP" then
 if Modesel = 2 then [ModeSelection]
 goto [BatchRun]
end if

'-------------------------------------------------FP---------------
-----------------------------------
[FPBulkWrite]

let FeUnitCell(    1    ,    1    ) =    0.78223
let FeUnitCell(    2    ,    1    ) =    0.217922
let FeUnitCell(    3    ,    1    ) =    0.282231
let FeUnitCell(    4    ,    1    ) =    0.717921
let OUnitCell(    1    ,    1    ) =    0.873966
let OUnitCell(    2    ,    1    ) =    0.626185
let OUnitCell(    3    ,    1    ) =    0.373967
let OUnitCell(    4    ,    1    ) =    0.126187
let OUnitCell(    5    ,    1    ) =    0.947321
let OUnitCell(    6    ,    1    ) =    0.052831
let OUnitCell(    7    ,    1    ) =    0.447321
let OUnitCell(    8    ,    1    ) =    0.552831
let OUnitCell(    9    ,    1    ) =    0.825585
let OUnitCell(    10    ,    1    ) =    0.674567
let OUnitCell(    11    ,    1    ) =    0.325586
```

```
let OUnitCell(    12    ,    1    ) =    0.174567
let OUnitCell(    13    ,    1    ) =    0.174567
let OUnitCell(    14    ,    1    ) =    0.325586
let OUnitCell(    15    ,    1    ) =    0.674567
let OUnitCell(    16    ,    1    ) =    0.825585
let PUnitCell(    1     ,    1    ) =    0.402317
let PUnitCell(    2     ,    1    ) =    0.597835
let PUnitCell(    3     ,    1    ) =    0.902316
let PUnitCell(    4     ,    1    ) =    0.097836
let FeUnitCell(    1    ,    2    ) =    0.25
let FeUnitCell(    2    ,    2    ) =    0.75
let FeUnitCell(    3    ,    2    ) =    0.25
let FeUnitCell(    4    ,    2    ) =    0.75
let OUnitCell(    1     ,    2    ) =    0.75
let OUnitCell(    2     ,    2    ) =    0.25
let OUnitCell(    3     ,    2    ) =    0.75
let OUnitCell(    4     ,    2    ) =    0.25
let OUnitCell(    5     ,    2    ) =    0.25
let OUnitCell(    6     ,    2    ) =    0.75
let OUnitCell(    7     ,    2    ) =    0.25
let OUnitCell(    8     ,    2    ) =    0.75
let OUnitCell(    9     ,    2    ) =    0.949654
let OUnitCell(    10    ,    2    ) =    0.050347
let OUnitCell(    11    ,    2    ) =    0.550347
let OUnitCell(    12    ,    2    ) =    0.050346
let OUnitCell(    13    ,    2    ) =    0.449654
let OUnitCell(    14    ,    2    ) =    0.949653
let OUnitCell(    15    ,    2    ) =    0.449653
let OUnitCell(    16    ,    2    ) =    0.550346
let PUnitCell(    1     ,    2    ) =    0.75
let PUnitCell(    2     ,    2    ) =    0.25
let PUnitCell(    3     ,    2    ) =    0.75
let PUnitCell(    4     ,    2    ) =    0.25
let FeUnitCell(    1    ,    3    ) =    0.5261
let FeUnitCell(    2    ,    3    ) =    0.406228
let FeUnitCell(    3    ,    3    ) =    0.906227
let FeUnitCell(    4    ,    3    ) =    0.0261
let OUnitCell(    1     ,    3    ) =    0.252914
let OUnitCell(    2     ,    3    ) =    0.752912
let OUnitCell(    3     ,    3    ) =    0.179414
let OUnitCell(    4     ,    3    ) =    0.679412
let OUnitCell(    5     ,    3    ) =    0.316793
let OUnitCell(    6     ,    3    ) =    0.615536
let OUnitCell(    7     ,    3    ) =    0.11554
let OUnitCell(    8     ,    3    ) =    0.816789
let OUnitCell(    9     ,    3    ) =    0.718099
let OUnitCell(    10    ,    3    ) =    0.218098
let OUnitCell(    11    ,    3    ) =    0.714229
let OUnitCell(    12    ,    3    ) =    0.214228
let OUnitCell(    13    ,    3    ) =    0.214228
let OUnitCell(    14    ,    3    ) =    0.714229
let OUnitCell(    15    ,    3    ) =    0.218098
```

```
let OUnitCell(    16    ,    3    ) =    0.718099
let PUnitCell(    1     ,    3    ) =    0.871469
let PUnitCell(    2     ,    3    ) =    0.060859
let PUnitCell(    3     ,    3    ) =    0.560859
let PUnitCell(    4     ,    3    ) =    0.371468

'write Bulk input
open  "C:\Program  Files  (x86)\gulp\Exe\SC\FPSC"  +  STR$(sizea)  +
STR$(sizeb)        +        STR$(sizec)        +        "-"        +
STR$(int(100*defectNumber/sizea/sizeb/sizec/4))  +  "pc_bulk.gin"  for
output as #Gin

print #Gin, "opti conp phonon"
print #Gin, "temperature 298"

print #Gin, ""
print #Gin, "name FP-bulk"
print #Gin, "cell"
print       #Gin,       STR$(FPCellParametera*sizea);       "       ";
STR$(FPCellParameterb*sizeb);  "  ";  STR$(FPCellParameterc*sizec);  "
90 90 90"
print #Gin, ""

print #Gin, "fractional"

For a=0 to sizea-1
 For b=0 to sizeb-1
  For c=0 to sizec-1
   For i=1 to 4
    print            #Gin,            "Fe2            core            ";
STR$(FeSuperCell(i+4*sizeb*sizec*a+4*sizec*b+4*c,1));       "       ";
STR$(FeSuperCell(i+4*sizeb*sizec*a+4*sizec*b+4*c,2));       "       ";
STR$(FeSuperCell(i+4*sizeb*sizec*a+4*sizec*b+4*c,3))
    next i
   For i=1 to 4
    print            #Gin,            "P1             core            ";
STR$(PSuperCell(i+4*sizeb*sizec*a+4*sizec*b+4*c,1));        "       ";
STR$(PSuperCell(i+4*sizeb*sizec*a+4*sizec*b+4*c,2));        "       ";
STR$(PSuperCell(i+4*sizeb*sizec*a+4*sizec*b+4*c,3))
    next i
   For i=1 to 16
    print            #Gin,            "O1             core            ";
STR$(OSuperCell(i+16*sizeb*sizec*a+16*sizec*b+16*c,1));      "      ";
STR$(OSuperCell(i+16*sizeb*sizec*a+16*sizec*b+16*c,2));      "      ";
STR$(OSuperCell(i+16*sizeb*sizec*a+16*sizec*b+16*c,3))
    print            #Gin,            "O1             shel            ";
STR$(OSuperCell(i+16*sizeb*sizec*a+16*sizec*b+16*c,1));      "      ";
STR$(OSuperCell(i+16*sizeb*sizec*a+16*sizec*b+16*c,2));      "      ";
STR$(OSuperCell(i+16*sizeb*sizec*a+16*sizec*b+16*c,3))
    next i
   next c
  next b
```

```
 next a

print #Gin, "space"
print #Gin, "P 1"
print #Gin, ""
print #Gin, "shrink   2"
print #Gin, "species   6"
print #Gin, "Li1    core    1.000000"
print #Gin, "Fe1    core    2.000000"
print #Gin, "Fe2    core    3.000000"
print #Gin, "P1     core    4.970800"
print #Gin, "O1     shel   -2.894200"
print #Gin, "O1     core    0.901500"
print #Gin, "buck"
print  #Gin,  "Li      core  O       shel   381.524400        0.304910
0.000000      0.00  10.00"
print #Gin, "buck"
print  #Gin,  "Fe1     core  O       shel   13207.0079        0.222450
0.000000      0.00  10.00"
print #Gin, "buck"
print  #Gin,  "Fe2     core  O       shel   2111.96710        0.289410
0.000000      0.00  10.00"
print #Gin, "buck"
print  #Gin,  "P       core  O       shel   1028.97410        0.335300
0.000000      0.00  10.00"
print #Gin, "buck"
print  #Gin,  "O       shel  O       shel   39.7594000        0.477130
53.20373      0.00  10.00"
print #Gin, "spring"
print #Gin, "O      67.356400"

close #Gin

print "Done writing FP bulk file."

'Create defect Files
[FPDefectWrite]

For NumberDefectCalc=1 to defectCalculations

 dim M1(defectNumber)
 dim M2(defectNumber)
 dim ReadM1(defectNumber,3)
 dim ReadM2(defectNumber,3)
 let repetition = 0

 For DefectCount=1 to defectNumber
  [FPSetM1M2]
  let repetition = 0
  M1(DefectCount) = int(RND(1)*4*sizea*sizeb*sizec+1)
  M2(DefectCount) = int(RND(1)*4*sizea*sizeb*sizec+1)
  If DefectCount > 1 then
```

```
   For k=1 to DefectCount-1
    if M1(DefectCount) = M1(k) then let repetition = 1
    if M2(DefectCount) = M2(k) then let repetition = 1
    next k
  End if
  if repetition = 1 then [FPSetM1M2]

  'Read M1 and M2
  ReadM1(DefectCount,1) = LiSuperCell(M1(DefectCount),1)
  ReadM1(DefectCount,2) = LiSuperCell(M1(DefectCount),2)
  ReadM1(DefectCount,3) = LiSuperCell(M1(DefectCount),3)
  ReadM2(DefectCount,1) = FeSuperCell(M2(DefectCount),1)
  ReadM2(DefectCount,2) = FeSuperCell(M2(DefectCount),2)
  ReadM2(DefectCount,3) = FeSuperCell(M2(DefectCount),3)

  'Exchange M1 and M2
  let LiSuperCell(M1(DefectCount),1) = ReadM2(DefectCount,1)
  let LiSuperCell(M1(DefectCount),2) = ReadM2(DefectCount,2)
  let LiSuperCell(M1(DefectCount),3) = ReadM2(DefectCount,3)
  let FeSuperCell(M2(DefectCount),1) = ReadM1(DefectCount,1)
  let FeSuperCell(M2(DefectCount),2) = ReadM1(DefectCount,2)
  let FeSuperCell(M2(DefectCount),3) = ReadM1(DefectCount,3)

  next DefectCount

 open "C:\Program Files (x86)\gulp\Exe\SC\FPSC" + STR$(sizea) +
STR$(sizeb) + STR$(sizec) + "-" +
STR$(int(100*defectNumber/sizea/sizeb/sizec/4)) + "pc_defect" +
STR$(NumberDefectCalc) + ".gin" for output as #Gin

 print #Gin, "opti conp phonon"
 print #Gin, "temperature 298"

 print #Gin, ""
 print #Gin, "name FP-defect" + STR$(NumberDefectCalc)
 print #Gin, "cell"
 print #Gin, STR$(FPCellParametera*sizea); " ";
STR$(FPCellParameterb*sizeb); " "; STR$(FPCellParameterc*sizec); "
90 90 90"
 print #Gin, ""

 print #Gin, "fractional"

 For a=0 to sizea-1
  For b=0 to sizeb-1
   For c=0 to sizec-1
    For i=1 to 4
     print #Gin, "Fe2 core ";
STR$(FeSuperCell(i+4*sizeb*sizec*a+4*sizec*b+4*c,1)); " ";
STR$(FeSuperCell(i+4*sizeb*sizec*a+4*sizec*b+4*c,2)); " ";
STR$(FeSuperCell(i+4*sizeb*sizec*a+4*sizec*b+4*c,3))
     next i
```

```
    For i=1 to 4
     print            #Gin,            "P1            core            ";
STR$(PSuperCell(i+4*sizeb*sizec*a+4*sizec*b+4*c,1));       "       ";
STR$(PSuperCell(i+4*sizeb*sizec*a+4*sizec*b+4*c,2));       "       ";
STR$(PSuperCell(i+4*sizeb*sizec*a+4*sizec*b+4*c,3))
     next i
    For i=1 to 16
     print            #Gin,            "O1            core            ";
STR$(OSuperCell(i+16*sizeb*sizec*a+16*sizec*b+16*c,1));     "       ";
STR$(OSuperCell(i+16*sizeb*sizec*a+16*sizec*b+16*c,2));     "       ";
STR$(OSuperCell(i+16*sizeb*sizec*a+16*sizec*b+16*c,3))
     print            #Gin,            "O1            shel            ";
STR$(OSuperCell(i+16*sizeb*sizec*a+16*sizec*b+16*c,1));     "       ";
STR$(OSuperCell(i+16*sizeb*sizec*a+16*sizec*b+16*c,2));     "       ";
STR$(OSuperCell(i+16*sizeb*sizec*a+16*sizec*b+16*c,3))
     next i
    next c
   next b
  next a

 print #Gin, "space"
 print #Gin, "P 1"
 print #Gin, ""
 print #Gin, "shrink   2"
 print #Gin, "species   6"
 print #Gin, "Li1    core    1.000000"
 print #Gin, "Fe1    core    2.000000"
 print #Gin, "Fe2    core    3.000000"
 print #Gin, "P1     core    4.970800"
 print #Gin, "O1     shel   -2.894200"
 print #Gin, "O1     core    0.901500"
 print #Gin, "buck"
 print #Gin, "Li      core O       shel   381.524400        0.304910
0.000000      0.00  10.00"
 print #Gin, "buck"
 print #Gin, "Fe1     core O       shel   13207.0079        0.222450
0.000000      0.00  10.00"
 print #Gin, "buck"
 print #Gin, "Fe2     core O       shel   2111.96710        0.289410
0.000000      0.00  10.00"
 print #Gin, "buck"
 print #Gin, "P       core O       shel   1028.97410        0.335300
0.000000      0.00  10.00"
 print #Gin, "buck"
 print #Gin, "O       shel O       shel   39.7594000        0.477130
53.20373      0.00  10.00"
 print #Gin, "spring"
 print #Gin, "O      67.356400"

 close #Gin

 For DefectCount=1 to defectNumber
```

```
  let LiSuperCell(M1(DefectCount),1) = ReadM1(DefectCount,1)
  let LiSuperCell(M1(DefectCount),2) = ReadM1(DefectCount,2)
  let LiSuperCell(M1(DefectCount),3) = ReadM1(DefectCount,3)
  let FeSuperCell(M2(DefectCount),1) = ReadM2(DefectCount,1)
  let FeSuperCell(M2(DefectCount),2) = ReadM2(DefectCount,2)
  let FeSuperCell(M2(DefectCount),3) = ReadM2(DefectCount,3)

  next DefectCount

 print "Done writing FP defect file #" + STR$(NumberDefectCalc) + ".
(first defect M1=(" + left$(STR$(ReadM1(1,1)),6) + "," +
left$(STR$(ReadM1(1,2)),6) + "," + left$(STR$(ReadM1(1,3)),6) + ")
and M2=(" + left$(STR$(ReadM2(1,1)),6) + "," +
left$(STR$(ReadM2(1,2)),6) + "," + left$(STR$(ReadM2(1,3)),6) + ")."

 next NumberDefectCalc

if Modesel = 3 then [ModeSelection]

'Create Batch File
open "C:\Program Files (x86)\gulp\Exe\SC\FPSC" + STR$(sizea) +
STR$(sizeb) + STR$(sizec) + "-" +
STR$(int(100*defectNumber/sizea/sizeb/sizec/4)) + "pc.bat" for
output as #Bat

print #Bat, "Pause"
print #Bat, ":: Batch file for running a " + STR$(sizea) +
STR$(sizeb) + STR$(sizec) + " Super Cell with " + STR$(defectNumber)
+ " inter-site exchange defects in " + STR$(defectCalculations) + "
calculations."
print #Bat, "cd C:/Program Files (x86)/gulp/Exe/"
print #Bat, chr$(34) + "gulp.exe" + chr$(34) + " < SC/FPSC" +
STR$(sizea) + STR$(sizeb) + STR$(sizec) + "-" +
STR$(int(100*defectNumber/sizea/sizeb/sizec/4)) + "pc_bulk.gin >
SC/FPSC" + STR$(sizea) + STR$(sizeb) + STR$(sizec) + "-" +
STR$(int(100*defectNumber/sizea/sizeb/sizec/4)) + "pc_bulk.gout"

For NumberDefectCalc=1 to defectCalculations

 print #Bat, chr$(34) + "gulp.exe" + chr$(34) + " < SC/FPSC" +
STR$(sizea) + STR$(sizeb) + STR$(sizec) + "-" +
STR$(int(100*defectNumber/sizea/sizeb/sizec/4)) + "pc_defect" +
STR$(NumberDefectCalc) + ".gin > SC/FPSC" + STR$(sizea) +
STR$(sizeb) + STR$(sizec) + "-" +
STR$(int(100*defectNumber/sizea/sizeb/sizec/4)) + "pc_defect" +
STR$(NumberDefectCalc) + ".gout"
 next NumberDefectCalc

print #Bat, "Pause"

close #Bat
```

```
print "Done writing batch file."

'Create Shell File
open "C:\Program Files (x86)\gulp\Exe\SC\FPSC" + STR$(sizea) +
STR$(sizeb) + STR$(sizec) + "-" +
STR$(int(100*defectNumber/sizea/sizeb/sizec/4)) + "pc.sh" for output
as #Shell

print #Shell, "#!/bin/bash"
print #Shell, "# Shell file for running a " + STR$(sizea) +
STR$(sizeb) + STR$(sizec) + " Super Cell with " + STR$(defectNumber)
+ " inter-site exchange defects in " + STR$(defectCalculations) + "
calculations."
print #Shell, ""
print #Shell, "mpirun gulp < SC/FPSC" + STR$(sizea) + STR$(sizeb) +
STR$(sizec) + "-" + STR$(int(100*defectNumber/sizea/sizeb/sizec/4))
+ "pc_bulk.gin > SC/FPSC" + STR$(sizea) + STR$(sizeb) + STR$(sizec)
+ "-" + STR$(int(100*defectNumber/sizea/sizeb/sizec/4)) +
"pc_bulk.gout"

For NumberDefectCalc=1 to defectCalculations

 print #Shell, "mpirun gulp < SC/FPSC" + STR$(sizea) + STR$(sizeb) +
STR$(sizec) + "-" + STR$(int(100*defectNumber/sizea/sizeb/sizec/4))
+ "pc_defect" + STR$(NumberDefectCalc) + ".gin > SC/FPSC" +
STR$(sizea) + STR$(sizeb) + STR$(sizec) + "-" +
STR$(int(100*defectNumber/sizea/sizeb/sizec/4)) + "pc_defect" +
STR$(NumberDefectCalc) + ".gout"
 next NumberDefectCalc

close #Shell

print "Done writing shell file."

if Modesel = 2 then [ModeSelection]

'-----------------------------------------------RUN---------------
----------------------------------------
'Run Batch File
[BatchRun]
If LFPFP$ <> "FP" then run "C:\Program Files
(x86)\gulp\Exe\SC\LFPSC" + STR$(sizea) + STR$(sizeb) + STR$(sizec) +
".bat"

 print "Running LFP calculations."
 input "Hit Enter, when the batch file has terminated calculations
:"; Nonesense

If LFPFP$ <> "LFP" then run "C:\Program Files
(x86)\gulp\Exe\SC\FPSC" + STR$(sizea) + STR$(sizeb) + STR$(sizec) +
".bat"
```

```
 print "Running FP calculations."
 input "Hit Enter, when the batch file has terminated calculations
:"; Nonesense

'-----------------------------------------------EVALUATE----------
----------------------------------------
'Evaluation
[Evaluation]

dim Thermodynamics(defectCalculations+1,3)

If LFPFP$ <> "FP" then
 open "C:/Program Files (x86)/gulp/Exe/SC/LFPSC" + STR$(sizea) +
STR$(sizeb) + STR$(sizec) + "-" +
STR$(int(100*defectNumber/sizea/sizeb/sizec/4)) + "pc_bulk.gout" for
input as #Gout

 While instr(goutLine$,"Final energy") = 0
  if eof(#Gout) = -1 then [Error1]
  line input #Gout, goutLine$
 Wend

 let Thermodynamics(1,1) = val(trim$(mid$(goutLine$,17,18)))

 While instr(goutLine$,"Entropy") = 0
  if eof(#Gout) = -1 then [Error1]
  line input #Gout, goutLine$
 Wend

 let Thermodynamics(1,2) = val(trim$(mid$(goutLine$,33,17)))

 While instr(goutLine$,"Helmholtz") = 0
  if eof(#Gout) = -1 then [Error1]
  line input #Gout, goutLine$
 Wend

 let Thermodynamics(1,3) = val(trim$(mid$(goutLine$,33,17)))

 close #Gout


 For NumberDefectCalc=1 to defectCalculations

  open "C:/Program Files (x86)/gulp/Exe/SC/LFPSC" + STR$(sizea) +
STR$(sizeb) + STR$(sizec) + "-" +
STR$(int(100*defectNumber/sizea/sizeb/sizec/4)) + "pc_defect" +
STR$(NumberDefectCalc) + ".gout" for input as #Gout

  While instr(goutLine$,"Final energy") = 0
   if eof(#Gout) = -1 then [Error1]
   line input #Gout, goutLine$
```

```
  Wend

  let              Thermodynamics(NumberDefectCalc+1,1)              =
val(trim$(mid$(goutLine$,17,18)))

  While instr(goutLine$,"Entropy") = 0
   if eof(#Gout) = -1 then [Error1]
   line input #Gout, goutLine$
  Wend

  let              Thermodynamics(NumberDefectCalc+1,2)              =
val(trim$(mid$(goutLine$,33,17)))

  While instr(goutLine$,"Helmholtz") = 0
   if eof(#Gout) = -1 then [Error1]
   line input #Gout, goutLine$
  Wend

  let              Thermodynamics(NumberDefectCalc+1,3)              =
val(trim$(mid$(goutLine$,33,17)))

  close #Gout

  next NumberDefectCalc

 print "------- LFP Defect Thermodynamics ----------"
 print "  Ed / eV      Sd / eV/K      Gd / eV"

 dim defectEnergy(defectCalculations)
 dim defectFreeEnergy(defectCalculations)
 dim defectEntropy(defectCalculations)

 'For NumberDefectCalc=1 to defectCalculations
 '           let           defectEnergy(NumberDefectCalc)           =
Thermodynamics(NumberDefectCalc+1,1)-Thermodynamics(1,1)
 '          let          defectFreeEnergy(NumberDefectCalc)          =
Thermodynamics(NumberDefectCalc+1,2)-Thermodynamics(1,2)
 '           let           defectEntropy(NumberDefectCalc)           =
Thermodynamics(NumberDefectCalc+1,3)-Thermodynamics(1,3)
 ' print "   "; left$(STR$(defectEnergy(NumberDefectCalc)),8);"     ";
left$(STR$(defectFreeEnergy(NumberDefectCalc)),8);"                 ";
STR$(defectEntropy(NumberDefectCalc))
 ' next NumberDefectCalc

 For NumberDefectCalc=1 to defectCalculations
  let                defectEnergy(NumberDefectCalc)                =
Thermodynamics(NumberDefectCalc+1,1)+1020.80248624*sizea*sizeb*sizec
  let               defectEntropy(NumberDefectCalc)                =
Thermodynamics(NumberDefectCalc+1,2)-0.004747*sizea*sizeb*sizec
  let             defectFreeEnergy(NumberDefectCalc)               =
Thermodynamics(NumberDefectCalc+1,3)+1018.995796*sizea*sizeb*sizec
```

```
  print "   "; left$(STR$(defectEnergy(NumberDefectCalc)),8);"      ";
left$(STR$(defectEntropy(NumberDefectCalc)),8);"                    ";
STR$(defectFreeEnergy(NumberDefectCalc))
  next NumberDefectCalc
End if

If LFPFP$ <> "LFP" then
 open "C:/Program Files (x86)/gulp/Exe/SC/FPSC" + STR$(sizea) +
STR$(sizeb) + STR$(sizec) + "-" +
STR$(int(100*defectNumber/sizea/sizeb/sizec/4)) + "pc_bulk.gout" for
input as #Gout

 While instr(goutLine$,"Final energy") = 0
  if eof(#Gout) = -1 then [Error1]
  line input #Gout, goutLine$
 Wend

 let Thermodynamics(1,1) = val(trim$(mid$(goutLine$,17,18)))

 While instr(goutLine$,"Entropy") = 0
  if eof(#Gout) = -1 then [Error1]
  line input #Gout, goutLine$
 Wend

 let Thermodynamics(1,2) = val(trim$(mid$(goutLine$,33,17)))

 While instr(goutLine$,"Helmholtz") = 0
  if eof(#Gout) = -1 then [Error1]
  line input #Gout, goutLine$
 Wend

 let Thermodynamics(1,3) = val(trim$(mid$(goutLine$,33,17)))

 close #Gout


 For NumberDefectCalc=1 to defectCalculations

  open "C:/Program Files (x86)/gulp/Exe/SC/FPSC" + STR$(sizea) +
STR$(sizeb) + STR$(sizec) + "-" +
STR$(int(100*defectNumber/sizea/sizeb/sizec/4)) + "pc_defect" +
STR$(NumberDefectCalc) + ".gout" for input as #Gout

  While instr(goutLine$,"Final energy") = 0
   if eof(#Gout) = -1 then [Error1]
   line input #Gout, goutLine$
  Wend

  let Thermodynamics(NumberDefectCalc+1,1) =
val(trim$(mid$(goutLine$,17,18)))

  While instr(goutLine$,"Entropy") = 0
```

```
   if eof(#Gout) = -1 then [Error1]
   line input #Gout, goutLine$
  Wend

  let              Thermodynamics(NumberDefectCalc+1,2)              =
val(trim$(mid$(goutLine$,33,17)))

  While instr(goutLine$,"Helmholtz") = 0
   if eof(#Gout) = -1 then [Error1]
   line input #Gout, goutLine$
  Wend

  let              Thermodynamics(NumberDefectCalc+1,3)              =
val(trim$(mid$(goutLine$,33,17)))

  close #Gout

  next NumberDefectCalc

 print "------- FP Defect Thermodynamics ----------"
 print "  Ed / eV     Sd / eV/K     Gd / eV"

 dim defectEnergy(defectCalculations)
 dim defectFreeEnergy(defectCalculations)
 dim defectEntropy(defectCalculations)

 For NumberDefectCalc=1 to defectCalculations
  let                 defectEnergy(NumberDefectCalc)                =
Thermodynamics(NumberDefectCalc+1,1)-Thermodynamics(1,1)
  let               defectFreeEnergy(NumberDefectCalc)              =
Thermodynamics(NumberDefectCalc+1,2)-Thermodynamics(1,2)
  let                defectEntropy(NumberDefectCalc)                =
Thermodynamics(NumberDefectCalc+1,3)-Thermodynamics(1,3)
  print "   "; left$(STR$(defectEnergy(NumberDefectCalc)),8);"     ";
left$(STR$(defectFreeEnergy(NumberDefectCalc)),8);"               ";
STR$(defectEntropy(NumberDefectCalc))
  next NumberDefectCalc

 'For NumberDefectCalc=1 to defectCalculations
 '           let           defectEnergy(NumberDefectCalc)           =
Thermodynamics(NumberDefectCalc+1,1)+1020.80248624*sizea*sizeb*sizec
 '           let           defectEntropy(NumberDefectCalc)          =
Thermodynamics(NumberDefectCalc+1,2)-0.004747*sizea*sizeb*sizec
 '          let          defectFreeEnergy(NumberDefectCalc)          =
Thermodynamics(NumberDefectCalc+1,3)+1018.995796*sizea*sizeb*sizec
 ' print "   "; left$(STR$(defectEnergy(NumberDefectCalc)),8);"     ";
left$(STR$(defectEntropy(NumberDefectCalc)),8);"                  ";
STR$(defectFreeEnergy(NumberDefectCalc))
 ' next NumberDefectCalc
End if

input "Press enter to restart :"; Nonesense
```

```
goto [ModeSelection]

[Error1]
print ""
print "----- Error during evaluation. ------ Error in gulp output
file.------"
close #Gout
goto [ModeSelection]
```

BIBLIOGRAPHY

Adams, S., & Rao, R. P. (2011). Simulated defect and interface engineering for high power Li electrode materials. *Solid State Ionics, 184*(1), 57-61. doi: 10.1016/j.ssi.2010.09.011

Aduru, S., Contarini, S., & Rabalais, J. W. (1986). Electron-, x-ray-, and ion-stimulated decomposition of nitrate salts. *Journal of Physical Chemistry, 90*(8), 1683-1688. doi: 10.1021/j100399a045

Ait-Salah, A., Dodd, J., Mauger, A., Yazami, R., Gendron, F., & Julien, C. M. (2006). Structural and Magnetic Properties of $LiFePO_4$ and Lithium Extraction Effects. *Zeitschrift für anorganische und allgemeine Chemie, 632*(8-9), 1598-1605. doi: 10.1002/zaac.200600090

Allen, J. L., Jow, T. R., & Wolfenstine, J. (2007). Kinetic Study of the Electrochemical $FePO_4$ to $LiFePO_4$ Phase Transition. *Chemistry of Materials, 19*(8), 2108-2111. doi: 10.1021/cm062963o

Allen, J. L., Jow, T. R., & Wolfenstine, J. (2012). Correction to Kinetic Study of the Electrochemical $FePO_4$ to $LiFePO_4$ Phase Transition. *Chemistry of Materials, 24*(7), 1400-1400. doi: 10.1021/cm300743n

Amin, R., Balaya, P., & Maier, J. (2007). Anisotropy of Electronic and Ionic Transport in $LiFePO_4$ Single Crystals. *Electrochemical and Solid-State Letters, 10*(1), A13-A16. doi: 10.1149/1.2388240

APS/ANL. (2013). Overview of the APS Page consultée le Nov. 27th, 2013, à http://www.aps.anl.gov/About/APS_Overview/index.html

Arnold, G., Garche, J., Hemmer, R., Ströbele, S., Vogler, C., & Wohlfahrt-Mehrens, M. (2003). Fine-particle lithium iron phosphate $LiFePO_4$ synthesized by a new low-cost aqueous precipitation technique. *Journal of Power Sources, 119-121*, 247-251. doi: 10.1016/s0378-7753(03)00241-6

Avrami, M. (1939). Kinetics of phase change. I: General theory. *The Journal of Chemical Physics, 7*(12), 1103-1112. doi: 10.1063/1.1750380

Avrami, M. (1940). Kinetics of phase change. II Transformation-time relations for random distribution of nuclei. *The Journal of Chemical Physics, 8*(2), 212-224. doi: 10.1063/1.1750631

Avrami, M. (1941). Granulation, phase change, and microstructure kinetics of phase change. III. *The Journal of Chemical Physics, 9*(2), 177-184. doi: 10.1063/1.1750872

Badi, S.-P., Wagemaker, M., Ellis, B. L., Singh, D. P., Borghols, W. J. H., Kan, W. H., . . . Nazar, L. F. (2011). Direct synthesis of nanocrystalline $Li_{0.90}FePO_4$: observation of phase segregation of anti-site defects on delithiation. *Journal of Materials Chemistry, 21*(27), 10085-10093. doi: 10.1039/C0JM04378H

Bae, C. J., Erdonmez, C. K., Halloran, J. W., & Chiang, Y. M. (2013). Design of battery electrodes with dual-scale porosity to minimize tortuosity and maximize performance. *Advanced Materials, 25*(9), 1254-1258. doi: 10.1002/adma.201204055

Bai, P., Cogswell, D. A., & Bazant, M. Z. (2011). Suppression of phase separation in $LiFePO_4$ nanoparticles during battery discharge. *Nano Letters, 11*(11), 4890-4896. doi: 10.1021/nl202764f

Bai, P., & Tian, G. (2013). Statistical kinetics of phase-transforming nanoparticles in $LiFePO_4$ porous electrodes. *Electrochimica Acta, 89*(0), 644-651. doi: 10.1016/j.electacta.2012.11.070

Bard, A. J., & Faulkner, L. R. (2001). *Electrochemical Methods* (2ième éd.). Hoboken, NJ: John Wiley & Sons.

Boovaragavan, V., & Srinivasan, V. (2011). On the High Rate Capability of $LiFePO_4$. *ECS Transactions, 33*(29), 17-29. doi: 10.1149/1.3564866

Borg, R. J., & Dienes, G. J. (1992). *The Physical Chemistry of Solids*. San Diego: Academic Press.

Boulfelfel, S. E., Seifert, G., & Leoni, S. (2011). Atomistic investigation of Li+ diffusion pathways in the olivine $LiFePO_4$ cathode material. *Journal of Materials Chemistry, 21*(41), 16365-16372. doi: 10.1039/C1JM10725A

Bruce, P. G. (1997). Solid-state chemistry of lithium power sources. *Chemical Communications*(19), 1817-1824. doi: 10.1039/A608551B

Brunetti, G., Robert, D., Bayle-Guillèmaud, P., Rouvière, J. L., Rauch, E. F., Martin, J. F., . . . Cayron, C. (2011). Confirmation of the Domino-Cascade Model by $LiFePO_4/FePO_4$ Precession Electron Diffraction. *Chemistry of Materials, 23*(20), 4515-4524. doi: 10.1021/cm201783z

Buckingham, R. A. (1938). The Classical Equation of State of Gaseous Helium, Neon and Argon. *Proceedings of the Royal Society of London, Series A: Mathematical and Physical Sciences, 168*(933), 264-283.

Burba, C. M., & Frech, R. (2004). Raman and FTIR Spectroscopic Study of Li_xFePO_4 ($0 \leq x \leq 1$). *Journal of The Electrochemical Society, 151*(7), A1032-A1038.

Castro, L., Dedryvère, R., El Khalifi, M., Lippens, P. E., Bréger, J., Tessier, C., & Gonbeau, D. (2010). The spin-polarized electronic structure of $LiFePO_4$ and FePO 4 evidenced by in-lab XPS. *Journal of Physical Chemistry C, 114*(41), 17995-18000. doi: 10.1021/jp106631v

Chen, G., Song, X., & Richardson, T. J. (2007). Metastable Solid-Solution Phases in the $LiFePO_4/FePO_4$ System. *Journal of the Electrochemical Society, 154*(7), A627-A632. doi: 10.1149/1.2732189

Chen, J., & Graetz, J. (2011). Study of Antisite Defects in Hydrothermally Prepared $LiFePO_4$ by in Situ X-ray Diffraction. *ACS Applied Materials & Interfaces, 3*(5), 1380-1384. doi: 10.1021/am200141a

Cho, T.-H., & Chung, H.-T. (2004). Synthesis of olivine-type $LiFePO_4$ by emulsion-drying method. *Journal of Power Sources, 133*(2), 272-276. doi: 10.1016/j.jpowsour.2004.02.015

Chung, S.-Y., Choi, S.-Y., Yamamoto, T., & Ikuhara, Y. (2008). Atomic-Scale Visualization of Antisite Defects in $LiFePO_4$. *Physical Review Letters, 100*(12), 125502. doi: 10.1103/PhysRevLett.100.125502

Cogswell, D. A., & Bazant, M. Z. (2012). Coherency Strain and the Kinetics of Phase Separation in $LiFePO_4$ Nanoparticles. *ACS Nano, 6*(3), 2215-2225. doi: 10.1021/nn204177u

Cornut, R., Lepage, D., & Schougaard, S. B. (2012). Ohmic Drop in $LiFePO_4$ Based Lithium Battery Cathodes Containing Agglomerates. *Journal of the Electrochemical Society, 159*(6), A822-A827. doi: 10.1149/2.081206jes

Cuisinier, M., Martin, J. F., Dupré, N., Yamada, A., Kanno, R., & Guyomard, D. (2010). Moisture driven aging mechanism of LiFePO 4 subjected to air exposure. *Electrochemistry Communications, 12*(2), 238-241. doi: 10.1016/j.elecom.2009.12.003

Dargaville, S., & Farrell, T. W. (2013). The persistence of phase-separation in $LiFePO_4$ with two-dimensional Li^+ transport: The Cahn–Hilliard-reaction equation and the role of defects. *Electrochimica Acta, 94*(0), 143-158. doi: 10.1016/j.electacta.2013.01.082

Dathar, G. K. P., Sheppard, D., Stevenson, K. J., & Henkelman, G. (2011). Calculations of Li-Ion Diffusion in Olivine Phosphates. *Chemistry of Materials, 23*(17), 4032-4037. doi: 10.1021/cm201604g

Dean, J. A. (1999). *Lange's Handbook of Chemistry* (15 éd.). New York: McGraw Hill.

Delacourt, C., Poizot, P., Tarascon, J.-M., & Masquelier, C. (2005). The existence of a temperature-driven solid solution in Li_xFePO_4 for $0 \leq x \leq 1$. *Nature Materials, 4*(3), 254-260. doi: 10.1038/nmat1335

Delmas, C., Maccario, M., Croguennec, L., Le Cras, F., & Weill, F. (2008). Lithium deintercalation in $LiFePO_4$ nanoparticles via a domino-cascade model. *Nature Materials, 7*(8), 665-671. doi: 10.1038/nmat2230

Dick, B. G., & Overhauser, A. W. (1958). Theory of the Dielectric Constants of Alkali Halide Crystals. *Physical Review, 112*(1), 90-103. doi: 10.1103/PhysRev.112.90

Duda, R., Rejl, L., & Slivka, D. (1998). *Mineralien.* Augsburg: Bechtermünz Vlg.

Dufresne, E. M., Adams, B., Arms, D. A., Chollet, M., Landahl, E. C., Li, Y., . . . Wang, J. (2010). Time-Resolved Research at the Advanced Photon Source Beamline 7-ID. *AIP Conference Proceedings, 1234*(1), 181-184. doi: 10.1063/1.3463168

Fergus, J. W. (2010). Ceramic and polymeric solid electrolytes for lithium-ion batteries. *Journal of Power Sources, 195*(15), 4554-4569. doi: 10.1016/j.jpowsour.2010.01.076

Fick, A. (1855). Ueber Diffusion. *Annalen der Physik, 170*(1), 59-86. doi: 10.1002/andp.18551700105

Fisher, C. A. J., Hart Prieto, V. M., & Islam, M. S. (2008). Lithium Battery Materials $LiMPO_4$ (M = Mn, Fe, Co, and Ni): Insights into Defect Association, Transport Mechanisms, and Doping Behavior. *Chemistry of Materials, 20*(18), 5907-5915. doi: 10.1021/cm801262x

Franger, S., Le Cras, F., Bourbon, C., & Rouault, H. (2003). Comparison between different $LiFePO_4$ synthesis routes and their influence on its physico-chemical properties. *Journal of Power Sources, 119-121*, 252-257. doi: 10.1016/s0378-7753(03)00242-8

Furutsuki, S., Chung, S.-C., Nishimura, S.-i., Kudo, Y., Yamashita, K., & Yamada, A. (2012). Electrochromism of Li_xFePO_4 Induced by Intervalence Charge Transfer Transition. *The Journal of Physical Chemistry C, 116*(29), 15259-15264. doi: 10.1021/jp304221z

Gale, J. D., & Rohl, A. L. (2003). The General Utility Lattice Program (GULP). *Molecular Simulation, 29*(5), 291-341. doi: 10.1080/0892702031000104887

Gardiner, G. R., & Islam, M. S. (2010). Anti-site defects and ion migration in the $LiFe_{0.5}Mn_{0.5}PO_4$ mixed-metal cathode material. *Chemistry of Materials, 22*(3), 1242-1248. doi: 10.1021/cm902720z

Girard, S., Gale, J. D., Mellot-Draznieks, C., & Férey, G. (2001). Derivation of Interatomic Potentials for Gallophosphates from the $GaPO_4$–Quartz Structure: Transferability Study to Gallosilicates and Zeotype Gallophosphates. *Chemistry of Materials, 13*(5), 1732-1738. doi: 10.1021/cm001233s

Goldstein, J. I., Newbury, D. E., Joy, D. C., Lyman, C. E., Echlin, P., Lifshin, E., . . . Michael, J. R. (2003). *Scanning Electron Microscopy and X-ray Microanalysis* (3ième éd.): Springer.

Gorzkowska, I., Jozwiak, P., Garbarczyk, J. E., Wasiucionek, M., & Julien, C. M. (2008). Studies on glass transition of lithium-iron phosphate glasses. *Journal of Thermal Analysis and Calorimetry, 93*(3), 759-762. doi: 10.1007/s10973-008-9141-9

Graham-Rowe, E., Gardner, B., Abraham, C., Skippon, S., Dittmar, H., Hutchins, R., & Stannard, J. (2012). Mainstream consumers driving plug-in battery-electric and plug-in hybrid electric cars: A qualitative analysis of responses and evaluations. *Transportation Research Part A: Policy and Practice, 46*(1), 140-153. doi: 10.1016/j.tra.2011.09.008

Hamelet, S., Gibot, P., Casas-Cabanas, M., Bonnin, D., Grey, C. P., Cabana, J., . . . Masquelier, C. (2009). The effects of moderate thermal treatments under air

on LiFePO4-based nano powders. *Journal of Materials Chemistry, 19*(23), 3979-3991. doi: 10.1039/B901491H

Hebert, R. J. (2011). Nanocrystals in Metallic Glasses. Dans Y. Masuda (Éd.), *Nanocrystal*. Rijeka: InTech

Hönnerscheid, A., Nuss, J., Mühle, C., & Jansen, M. (2003). Die Kristallstrukturen der Monohydrate von Lithiumchlorid und Lithiumbromid. *Zeitschrift für anorganische und allgemeine Chemie, 629*(2), 312-316. doi: 10.1002/zaac.200390049

Hou, X., Hu, S., Li, W., Zhao, L., Ru, Q., Yu, H., & Huang, Z. (2008). Ab initio study of the effects of Ag/Mn doping on the electronic structure of $LiFePO_4$. *Chinese Science Bulletin, 53*(11), 1763-1767. doi: 10.1007/s11434-008-0091-1

Hsu, K.-F., Tsay, S.-Y., & Hwang, B.-J. (2004). Synthesis and characterization of nano-sized $LiFePO_4$ cathode materials prepared by a citric acid-based sol-gel route. *Journal of Materials Chemistry, 14*(17), 2690-2695. doi: 10.1039/B406774F

Huang, Y.-H., Wang, F.-M., Huang, T.-T., Chen, J.-M., Hwang, B.-J., & Rick, J. (2012). Micro-Electrode Linked Cyclic Voltammetry Study Reveals Ultra-Fast Discharge and High Ionic Transfer Behavior of $LiFePO_4$. *International Journal of Electrochemical Science, 7*, 1205-1213.

Ichitsubo, T., Tokuda, K., Yagi, S., Kawamori, M., Kawaguchi, T., Doi, T., . . . Matsubara, E. (2013). Elastically constrained phase-separation dynamics competing with the charge process in the $LiFePO_4/FePO_4$ system. *Journal of Materials Chemistry A, 1*(7), 2567-2577. doi: 10.1039/c2ta01102f

Islam, M. S., Driscoll, D. J., Fisher, C. A. J., & Slater, P. R. (2005). Atomic-scale investigation of defects, dopants, and lithium transport in the $LiFePO_4$ olivine-type battery material. *Chemistry of Materials, 17*(20), 5085-5092. doi: 10.1021/cm050999v

Jones, F. W. (1938). The Measurement of Particle Size by the X-Ray Method. *Proceedings of the Royal Society of London. Series A. Mathematical and Physical Sciences, 166*(924), 16-43. doi: 10.1098/rspa.1938.0079

Kang, B., & Ceder, G. (2009). Battery materials for ultrafast charging and discharging. *Nature, 458*(7235), 190-193. doi: 10.1038/nature07853

Kao, Y. H., Tang, M., Meethong, N., Bai, J., Carter, W. C., & Chiang, Y. M. (2010). Overpotential-dependent phase transformation pathways in lithium iron phosphate battery electrodes. *Chemistry of Materials, 22*(21), 5845-5855. doi: 10.1021/cm101698b

Kaushik, V. K. (1991). XPS core level spectra and Auger parameters for some silver compounds. *Journal of Electron Spectroscopy and Related Phenomena, 56*(3), 273-277. doi: 10.1016/0368-2048(91)85008-H

Kehrwald, D., Shearing, P. R., Brandon, N. P., Sinha, P. K., & Harris, S. J. (2011). Local tortuosity inhomogeneities in a lithium battery composite electrode. *Journal of The Electrochemical Society, 158*(12), A1393-A1399. doi: 10.1149/2.079112jes

Khawam, A., & Flanagan, D. R. (2006). Solid-state kinetic models: Basics and mathematical fundamentals. *Journal of Physical Chemistry B, 110*(35), 17315-17328.

Kim, K.-J. (2009). Characteristics of Synchrotron Radiation. Dans A. C. Thompson (Éd.), *X-ray data booklet* (3ième éd.). Berkeley, CA: Lawrence Berkeley National Laboratory.

Kuss, C., Lepage, D., Liang, G., & Schougaard, S. B. (2013). Ultrafast charging of $LiFePO_4$ with gaseous oxidants under ambient conditions. *Chemical Science, 4*(11), 4223-4227. doi: 10.1039/c3sc51195b

Kuss, C., Liang, G., & Schougaard, S. B. (2012). Atomistic modeling of site exchange defects in lithium iron phosphate and iron phosphate. *Journal of Materials Chemistry, 22*(47), 24889-24893. doi: 10.1039/c2jm35538h

Lepage, D., Sobh, F., Kuss, C., Liang, G., & Schougaard, S. B. (2014). Delithiation Kinetics Study of Carbon Coated and Carbon Free $LiFePO_4$. *Journal of Power Sources, 256*, 61-65. doi: 10.1016/j.jpowsour.2013.12.054

Levi, M. D., Sigalov, S., Salitra, G., Nayak, P., Aurbach, D., Daikhin, L., . . . Presser, V. (2013). Collective Phase Transition Dynamics in Microarray Composite Li_xFePO_4 Electrodes Tracked by in Situ Electrochemical Quartz Crystal Admittance. *The Journal of Physical Chemistry C, 117*(30), 15505-15514. doi: 10.1021/jp403653d

Li, J., Yao, W., Martin, S., & Vaknin, D. (2008). Lithium ion conductivity in single crystal $LiFePO_4$. *Solid State Ionics, 179*(35–36), 2016-2019. doi: 10.1016/j.ssi.2008.06.028

Liu, F., Siddique, N. A., & Mukherjee, P. P. (2011). Nonequilibrium phase transformation and particle shape effect in $LiFePO_4$ materials for Li-ion batteries. *Electrochemical and Solid-State Letters, 14*(10), A143-A147. doi: 10.1149/1.3610424

Liu, H., Strobridge, F. C., Borkiewicz, O. J., Wiaderek, K. M., Chapman, K. W., Chupas, P. J., & Grey, C. P. (2014). Capturing metastable structures during high-rate cycling of $LiFePO_4$ nanoparticle electrodes. *Science, 344*(6191), 1252817. doi: 10.1126/science.1252817

Lorca-Susino, M. (2008). A Brief Energy Outlook for the XXI Century *Jean Monnet/Robert Schuman Paper Series* (Vol. 15, pp. 1-18).

Malik, R., Abdellahi, A., & Ceder, G. (2013). A Critical Review of the Li Insertion Mechanisms in $LiFePO_4$ Electrodes. *Journal of The Electrochemical Society, 160*(5), A3179-A3197. doi: 10.1149/2.029305jes

Malik, R., Burch, D., Bazant, M., & Ceder, G. (2010). Particle Size Dependence of the Ionic Diffusivity. *Nano Letters, 10*(10), 4123-4127. doi: 10.1021/nl1023595

Malik, R., Zhou, F., & Ceder, G. (2011). Kinetics of non-equilibrium lithium incorporation in $LiFePO_4$. *Nature Materials, 10*(8), 587-590. doi: 10.1038/nmat3065

Marks, T., Trussler, S., Smith, A. J., Xiong, D., & Dahn, J. R. (2011). A Guide to Li-Ion Coin-Cell Electrode Making for Academic Researchers. *Journal of The Electrochemical Society, 158*(1), A51-A57. doi: 10.1149/1.3515072

Masquelier, C., Wurm, C., Rodríguez-Carvajal, J., Gaubicher, J., & Nazar, L. (2000). A Powder Neutron Diffraction Investigation of the Two Rhombohedral NASICON Analogues: γ-$Na_3Fe_2(PO_4)_3$ and $Li_3Fe_2(PO_4)_3$. *Chemistry of Materials, 12*(2), 525-532. doi: 10.1021/cm991138n

Meethong, N., Huang, H. Y. S., Speakman, S. A., Carter, W. C., & Chiang, Y. M. (2007). Strain accommodation during phase transformations in olivine-based cathodes as a materials selection criterion for high-power rechargeable batteries. *Advanced Functional Materials, 17*(7), 1115-1123. doi: 10.1002/adfm.200600938

Morales, J., Trócoli, R., Franger, S., & Santos-Peña, J. (2010). Cycling-induced stress in lithium ion negative electrodes: $LiAl/LiFePO_4$ and $Li_4Ti_5O_{12}/LiFePO_4$ cells. *Electrochimica Acta, 55*(9), 3075-3082. doi: 10.1016/j.electacta.2009.12.104

Morgan, D., Van der Ven, A., & Ceder, G. (2004). Li Conductivity in Li_xMPO_4 (M = Mn, Fe, Co, Ni) Olivine Materials. *Electrochemical and Solid-State Letters, 7*(2), A30-A32. doi: 10.1149/1.1633511

Mott, N. F., & Littleton, M. J. (1938). Conduction in polar crystals. I. Electrolytic conduction in solid salts. *Transactions of the Faraday Society, 34*, 485-499. doi: 10.1039/TF9383400485

Munakata, H., Takemura, B., Saito, T., & Kanamura, K. (2012). Evaluation of real performance of $LiFePO_4$ by using single particle technique. *Journal of Power Sources, 217*(0), 444-448. doi: 10.1016/j.jpowsour.2012.06.037

Nishimura, S.-i., Kobayashi, G., Ohoyama, K., Kanno, R., Yashima, M., & Yamada, A. (2008). Experimental visualization of lithium diffusion in Li_xFePO_4. *Nature Materials, 7*(9), 707-711. doi: 10.1038/nmat2251

Niu, J., Kushima, A., Qian, X., Qi, L., Xiang, K., Chiang, Y.-M., & Li, J. (2014). In Situ Observation of Random Solid Solution Zone in $LiFePO_4$ Electrode. *Nano Letters, 14*(7), 4005-4010. doi: 10.1021/nl501415b

Okubo, M., Hosono, E., Kim, J., Enomoto, M., Kojima, N., Kudo, T., . . . Honma, I. (2007). Nanosize effect on high-rate Li-ion intercalation in $LiCoO_2$ electrode. *Journal of the American Chemical Society, 129*(23), 7444-7452. doi: 10.1021/ja0681927

Ong, S. P., Chevrier, V. L., & Ceder, G. (2011). Comparison of small polaron migration and phase separation in olivine $LiMnPO_4$ and $LiFePO_4$ using hybrid density functional theory. *Physical Review B - Condensed Matter and Materials Physics, 83*(7). doi: 10.1103/PhysRevB.83.075112

Ong, S. P., Jain, A., Hautier, G., Kang, B., & Ceder, G. (2010). Thermal stabilities of delithiated olivine MPO_4 (M = Fe, Mn) cathodes investigated using first principles calculations. *Electrochemistry Communications, 12*(3), 427-430. doi: 10.1016/j.elecom.2010.01.010

Ong, S. P., Wang, L., Kang, B., & Ceder, G. (2008). Li - Fe - P - O2 phase diagram from first principles calculations. *Chemistry of Materials, 20*(5), 1798-1807. doi: 10.1021/cm702327g

Orikasa, Y., Maeda, T., Koyama, Y., Minato, T., Murayama, H., Fukuda, K., . . . Ogumi, Z. (2013). Phase Transition Analysis between $LiFePO_4$ and $FePO_4$ by In-Situ Time-Resolved X-ray Absorption and X-ray Diffraction. *Journal of The Electrochemical Society, 160*(5), A3061-A3065. doi: 10.1149/2.012305jes

Orikasa, Y., Maeda, T., Koyama, Y., Murayama, H., Fukuda, K., Tanida, H., . . . Ogumi, Z. (2013a). Direct Observation of a Metastable Crystal Phase of

Li_xFePO_4 under Electrochemical Phase Transition. *Journal of the American Chemical Society, 135*(15), 5497-5500. doi: 10.1021/ja312527x

Orikasa, Y., Maeda, T., Koyama, Y., Murayama, H., Fukuda, K., Tanida, H., . . . Ogumi, Z. (2013b). Transient Phase Change in Two Phase Reaction between $LiFePO_4$ and $FePO_4$ under Battery Operation. *Chemistry of Materials, 25*(7), 1032-1039. doi: 10.1021/cm303411t

Ouyang, C., Shi, S., Wang, Z., Huang, X., & Chen, L. (2004). First-principles study of Li ion diffusion in $LiFePO_4$. *Physical Review B, 69*(10), 104303. doi: 10.1103/PhysRevB.69.104303

Oyama, G., Yamada, Y., Natsui, R.-i., Nishimura, S.-i., & Yamada, A. (2012). Kinetics of Nucleation and Growth in Two-Phase Electrochemical Reaction of Li_xFePO_4. *The Journal of Physical Chemistry C, 116*(13), 7306-7311. doi: 10.1021/jp300085n

Padhi, A. K., Nanjundaswamy, K. S., & Goodenough, J. B. (1997). Phospho-olivines as Positive-Electrode Materials for Rechargeable Lithium Batteries. *Journal of The Electrochemical Society, 144*(4), 1188-1194. doi: 10.1149/1.1837571

Palomares, V., Goñi, A., Muro, I. G. d., de Meatza, I., Bengoechea, M., Miguel, O., & Rojo, T. (2007). New freeze-drying method for $LiFePO_4$ synthesis. *Journal of Power Sources, 171*(2), 879-885. doi: 10.1016/j.jpowsour.2007.06.161

Park, M., Zhang, X., Chung, M., Less, G. B., & Sastry, A. M. (2010). A review of conduction phenomena in Li-ion batteries. *Journal of Power Sources, 195*(24), 7904-7929. doi: 10.1016/j.jpowsour.2010.06.060

Prosini, P. P. (2005). Modeling the Voltage Profile for $LiFePO_4$. *Journal of the Electrochemical Society, 152*(10), A1925-A1929. doi: 10.1149/1.2006607

Prosini, P. P., Carewska, M., Scaccia, S., Wisniewski, P., Passerini, S., & Pasquali, M. (2002). A New Synthetic Route for Preparing $LiFePO_4$ with Enhanced Electrochemical Performance. *Journal of the Electrochemical Society, 149*(7), A886-A890. doi: 10.1149/1.1481716

Ratner, B. D., & Castner, D. G. (2009). Electron Spectroscopy for Chemical Analysis *Surface Analysis – The Principal Techniques* (pp. 47-112): John Wiley & Sons, Ltd.

Ravet, N., Goodenough, J. B., Besner, S., Simoneau, M., Hovington, P., & Armand, M. (1999. *Improved Iron Based Cathode Material.* Communication présentée 196th Meeting of the Electrochemical Society, Honolulu, HI.

Ren, Y., Armstrong, A. R., Jiao, F., & Bruce, P. G. (2010). Influence of size on the rate of mesoporous electrodes for lithium batteries. *Journal of the American Chemical Society, 132*(3), 996-1004. doi: 10.1021/ja905488x

Rodriguez-Carvajal, J. (2001). An Introduction to the Program FullProf 2000 (July2001 éd.). Gif-sur-Yvette, France.

Rousse, G., Rodriguez-Carvajal, J., Patoux, S., & Masquelier, C. (2003). Magnetic Structures of the Triphylite $LiFePO_4$ and of Its Delithiated Form $FePO_4$. *Chemistry of Materials, 15*(21), 4082-4090. doi: 10.1021/cm0300462

Sakdinawat, A., & Attwood, D. (2010). Nanoscale X-ray imaging. *Nature Photonics, 4*(12), 840-848. doi: 10.1038/nphoton.2010.267

Schmidt, J. P., Chrobak, T., Ender, M., Illig, J., Klotz, D., & Ivers-Tiffée, E. (2011). Studies on $LiFePO_4$ as cathode material using impedance spectroscopy. *Journal of Power Sources, 196*(12), 5342-5348. doi: 10.1016/j.jpowsour.2010.09.121

Schneider, C. A., Rasband, W. S., & Eliceiri, K. W. (2012). NIH Image to ImageJ: 25 years of image analysis. *Nat Meth, 9*(7), 671-675. doi: 10.1038/nmeth.2089

Sharma, N., Guo, X., Du, G., Guo, Z., Wang, J., Wang, Z., & Peterson, V. K. (2012). Direct Evidence of Concurrent Solid-Solution and Two-Phase Reactions and the Nonequilibrium Structural Evolution of $LiFePO_4$. *Journal of the American Chemical Society, 134*(18), 7867-7873. doi: 10.1021/ja301187u

Shi, S., Zhang, H., Ke, X., Ouyang, C., Lei, M., & Chen, L. (2009). First-principles study of lattice dynamics of $LiFePO_4$. *Physics Letters A, 373*(44), 4096-4100. doi: 10.1016/j.physleta.2009.09.014

Srinivasan, V., & Newman, J. (2004). Discharge Model for the Lithium Iron-Phosphate Electrode. *Journal of the Electrochemical Society, 151*(10), A1517-A1529. doi: 10.1149/1.1785012

Stokes, A. R., & Wilson, A. J. C. (1944). The diffraction of X rays by distorted crystal aggregates - I. *Proceedings of the Physical Society, 56*(3), 174. doi: 10.1088/0959-5309/56/3/303

Takahashi, M., Tobishima, S.-i., Takei, K., & Sakurai, Y. (2002). Reaction behavior of $LiFePO_4$ as a cathode material for rechargeable lithium batteries. *Solid State Ionics, 148*(3-4), 283-289. doi: 10.1016/s0167-2738(02)00064-4

Tang, M., Carter, W. C., Belak, J. F., & Chiang, Y. M. (2010). Modeling the competing phase transition pathways in nanoscale olivine electrodes. *Electrochimica Acta, 56*(2), 969-976. doi: 10.1016/j.electacta.2010.09.027

Tang, M., Carter, W. C., & Chiang, Y. M. (2010). Electrochemically driven phase transitions in insertion electrodes for lithium-ion batteries: Examples in lithium metal phosphate olivines. *Annual Review of Materials Research, 40*, 501-529.

Tang, M., Huang, H. Y., Meethong, N., Kao, Y. H., Carter, W. C., & Chiang, Y. M. (2009). Model for the Particle Size, Overpotential, and Strain Dependence of Phase Transition Pathways in Storage Electrodes: Application to Nanoscale Olivines. *Chemistry of Materials, 21*(8), 1557-1571. doi: 10.1021/cm803172s

Tarascon, J. M., & Armand, M. (2001). Issues and challenges facing rechargeable lithium batteries. *Nature, 414*(6861), 359-367. doi: 10.1038/35104644

Testa, B. M. (2009). Building the new electric grid. *Mechanical Engineering, 131*(12), 30-34.

Thorat, I. V., Joshi, T., Zaghib, K., Harb, J. N., & Wheeler, D. R. (2011). Understanding Rate-Limiting Mechanisms in $LiFePO_4$ Cathodes for Li-Ion Batteries. *Journal of The Electrochemical Society, 158*(11), A1185-A1193. doi: 10.1149/2.001111jes

Trinh, N. D., Liang, G., Gauthier, M., & Schougaard, S. B. (2012). A rapid solution method to determine the charge capacity of $LiFePO_4$. *Journal of Power Sources, 200*(0), 92-97. doi: 10.1016/j.jpowsour.2011.10.049

Vijayaraghavan, B., Ely, D. R., Chiang, Y. M., García-García, R., & García, R. E. (2012). An analytical method to determine tortuosity in rechargeable battery electrodes. *Journal of The Electrochemical Society, 159*(5), A548-A552. doi: 10.1149/2.jes113224

Voelcker, J. (2006). Electric Cars For Enlightened Stars. *Spectrum, IEEE, 43*(11), 14-16. doi: 10.1109/spec.2006.247950

Wang, Z., Sun, S., Xia, D., Chu, W., Zhang, S., & Wu, Z. (2008). Investigation of electronic conductivity and occupancy sites of Mo doped into $LiFePO_4$ by ab initio calculation and X-ray absorption spectroscopy. *Journal of Physical Chemistry C, 112*(44), 17450-17455. doi: 10.1021/jp801497z

Waseda, Y., Matsubara, E., & Kozo, S. (2011). *X-ray Diffraction Crystallography: Introduction, Examples and Solved Problems*. Berlin / Heidelberg: Springer.

Wiberg, N. (1995). *Lehrbuch der Anorganischen Chemie* (101 éd.). New York: Walter de Gruyter.

Wiedemann, H. (1998). Synchrotron Radiation Primer. Ithaca: Stanford Synchrotron Radiation Laboratory.

Williams, D. B., & Carter, C. B. (2009). *Transmission Electron Microscopy: A Textbook for Materials Science* (2ième éd.): Springer.

Williamson, G. K., & Hall, W. H. (1953). X-ray line broadening from filed aluminium and wolfram. *Acta Metallurgica, 1*(1), 22-31. doi: 10.1016/0001-6160(53)90006-6

Winter, M., Besenhard, J. O., Spahr, M. E., & Novák, P. (1998). Insertion Electrode Materials for Rechargeable Lithium Batteries. *Advanced Materials, 10*(10), 725-763. doi: 10.1002/(sici)1521-4095(199807)10:10<725::aid-adma725>3.0.co;2-z

Wu, X., Fronczek, F. R., & Butler, L. G. (1994). Structure of LiNO3: Point Charge Model and Sign of the 7Li Quadrupole Coupling Constant. *Inorganic Chemistry, 33*(7), 1363-1365. doi: 10.1021/ic00085a025

Xu, K. (2004). Nonaqueous Liquid Electrolytes for Lithium-Based Rechargeable Batteries. *Chemical Reviews, 104*(10), 4303-4418. doi: 10.1021/cr030203g

Yamada, A., Koizumi, H., Sonoyama, N., & Kanno, R. (2005). Phase Change in Li x $FePO_4$. *Electrochemical and Solid-State Letters, 8*(8), A409-A413. doi: 10.1149/1.1945373

Yamada, A., Kudo, Y., & Liu, K.-Y. (2001). Phase Diagram of $Li_x(Mn_yFe_{1-y})PO_4$ $(0 \leqslant x, y \leqslant 1)$ *Journal of the Electrochemical Society, 148*(10), A1153-A1158. doi: 10.1149/1.1401083

Yang, S., Zavalij, P. Y., & Whittingham, M. S. (2001). Hydrothermal synthesis of lithium iron phosphate cathodes. *Electrochemistry Communications, 3*(9), 505-508. doi: 10.1016/s1388-2481(01)00200-4

Yip, S. (Éd.). (2005). *Handbook of Materials Modeling* (Vol. A). Dordrecht: Springer.

Yoshino, A. (2012). The birth of the lithium-ion battery. *Angewandte Chemie - International Edition, 51*(24), 5798-5800. doi: 10.1002/anie.201105006

Yu, D. Y. W., Donoue, K., Inoue, T., Fujimoto, M., & Fujitani, S. (2006). Effect of Electrode Parameters on $LiFePO_4$ Cathodes. *Journal of the Electrochemical Society, 153*(5), A835-A839. doi: 10.1149/1.2179199

Yu, P., Popov, B. N., Ritter, J. A., & White, R. E. (1999). Determination of the Lithium Ion Diffusion Coefficient in Graphite. *Journal of the Electrochemical Society, 146*(1), 8-14. doi: 10.1149/1.1391556

Yu, X., Wang, Q., Zhou, Y., Li, H., Yang, X.-Q., Nam, K.-W., . . . Meng, Y. S. (2012). High rate delithiation behaviour of $LiFePO_4$ studied by quick X-ray absorption spectroscopy. *Chemical Communications, 48*(94), 11537-11539. doi: 10.1039/c2cc36382h

Yuan, L.-X., Wang, Z.-H., Zhang, W.-X., Hu, X.-L., Chen, J.-T., Huang, Y.-H., & Goodenough, J. B. (2011). Development and challenges of $LiFePO_4$ cathode material for lithium-ion batteries. *Energy & Environmental Science, 4*(2), 269-284. doi: 10.1039/C0EE00029A

Zaghib, K., Dontigny, M., Perret, P., Guerfi, A., Ramanathan, M., Prakash, J., . . . : Julien, C. M. (2014). Electrochemical and thermal characterization of lithium titanate spinel anode in C–$LiFePO_4$//C–$Li_4Ti_5O_{12}$ cells at sub-zero temperatures. *Journal of Power Sources, 248*(0), 1050-1057. doi: 10.1016/j.jpowsour.2013.09.083

Zaghib, K., Goodenough, J. B., Mauger, A., & Julien, C. (2009). Unsupported claims of ultrafast charging of $LiFePO_4$ Li-ion batteries. *Journal of Power Sources, 194*(2), 1021-1023. doi: 10.1016/j.jpowsour.2009.05.043

Zaghib, K., Mauger, A., Goodenough, J. B., Gendron, F., & Julien, C. M. (2007). Electronic, Optical, and Magnetic Properties of $LiFePO_4$: Small Magnetic Polaron Effects. *Chemistry of Materials, 19*(15), 3740-3747. doi: 10.1021/cm0710296

Zaghib, K., Mauger, A., Groult, H., Goodenough, J., & Julien, C. (2013). Advanced Electrodes for High Power Li-ion Batteries. *Materials, 6*(3), 1028-1049.

Zemann, J. (1960). Die Kristallstruktur von Lithiumphosphat, Li_3PO_4. *Acta Crystallographica, 13*(11), 863-867. doi: 10.1107/S0365110X60002132

Zhang, P., Wu, Y., Zhang, D., Xu, Q., Liu, J., Ren, X., . . . Hong, W. (2008). Molecular Dynamics Study on Ion Diffusion in $LiFePO_4$ Olivine Materials. *Journal of Physical Chemistry A, 112*(24), 5406-5410. doi: 10.1021/jp710204z

Zhang, S. S. (2006). A review on electrolyte additives for lithium-ion batteries. *Journal of Power Sources, 162*(2 SPEC. ISS.), 1379-1394. doi: 10.1016/j.jpowsour.2006.07.074

Zhang, S. S. (2007). A review on the separators of liquid electrolyte Li-ion batteries. *Journal of Power Sources, 164*(1), 351-364. doi: 10.1016/j.jpowsour.2006.10.065

Zhang, Y., Huo, Q.-y., Du, P.-p., Wang, L.-z., Zhang, A.-q., Song, Y.-h., . . . Li, G.-y. (2012). Advances in new cathode material $LiFePO_4$ for lithium-ion batteries. *Synthetic Metals, 162*(13–14), 1315-1326. doi: 10.1016/j.synthmet.2012.04.025

Zhao, Z., Si, X., Liu, X., He, L., & Liang, X. (2013). Li extraction from high Mg/Li ratio brine with $LiFePO_4/FePO_4$ as electrode materials. *Hydrometallurgy, 133*(0), 75-83. doi: 10.1016/j.hydromet.2012.11.013

Zhou, F., Maxisch, T., & Ceder, G. (2006). Configurational electronic entropy and the phase diagram of mixed-valence oxides: The case of Li_xFePO_4. *Physical Review Letters, 97*(15), 155704. doi: 10.1103/PhysRevLett.97.155704

Zhu, C., Gu, L., Suo, L., Popovic, J., Li, H., Ikuhara, Y., & Maier, J. (2014). Size-Dependent Staging and Phase Transition in $LiFePO_4/FePO_4$. *Advanced Functional Materials, 24*(3), 312-318. doi: 10.1002/adfm.201301792

Zhu, Y., & Wang, C. (2010). Galvanostatic Intermittent Titration Technique for Phase-Transformation Electrodes. *The Journal of Physical Chemistry C, 114*(6), 2830-2841. doi: 10.1021/jp9113333

Zhu, Y., Wang, J. W., Liu, Y., Liu, X., Kushima, A., Liu, Y., . . . Huang, J. Y. (2013). In Situ Atomic-Scale Imaging of Phase Boundary Migration in $FePO_4$ Microparticles during Electrochemical Lithiation. *Advanced Materials, 25*(38), 5461-5466. doi: 10.1002/adma.201301374